# OPTIMAL HIGH-SPEED RAIL ROUTE SELECTION USING GIS, REMOTE SENSING, AND MULTI-CRITERIA DECISION ANALYSIS TECHNIQUES

**Suhrabuddin NASERY**

**Master's Thesis**

**Department of Remote Sensing and Geographical Information Systems**

**Supervisor: Assoc. Prof. Dr. Uğur AVDAN**

**Eskişehir**

**Eskişehir Technical University**

**Institute of Graduate Programs**

**January 2022**

# ABSTRACT

## OPTIMAL HIGH-SPEED RAIL ROUTE SELECTION USING GIS, REMOTE SENSING, AND MULTI-CRITERIA DECISION ANALYSIS TECHNIQUES



Suhrabuddin NASERY

Department of Remote Sensing and Geographical Information Systems

Eskişehir Technical University, Institute of Graduate Programs, January 2022

Supervisor: Assoc. Prof. Dr. Uğur AVDAN



High-speed rails (HSR) are the most efficient mode of transportation from the perspective of travel time reduction, low travel costs, time-saving, and environment. The HSR route selection is an essential and complex process that involves several factors that must be considered. The integration of geographical information system (GIS) and remote sensing (RS) with multi-criteria decision analysis (MCDA) techniques has been used in different routing problems such as roads, railways, and HSR. In this study, a GIS-based MCDA method was adopted to generate the optimal HSR route between Kabul and Kandahar cities in Afghanistan. The influential factors on the HSR route location and their relative importance were determined by questionaries performed by transportation sector experts and the fuzzy analytical hierarchy process (fuzzy-AHP) and analytical hierarchy process (AHP) MCDA methods were employed to calculate their weights. Slope, land use/landcover (LULC), soil types, distance from rivers, proximity to roads, proximity to towns/cities, landslide risk, snow avalanche risk, flood risk, distance from faultlines were considered as the influential factors on the HSR route location selection. Separate analyses were performed for deriving the landslide, snow avalanche, and flood susceptibility layers/maps. The fuzzy-AHP method was utilized to calculate the weights and relative importance of the factors considered in a landslide, snow avalanche, and flood susceptibility assessments.

The results showed that the methodology adopted in this study successfully generated the optimal HSR route that is geometrically the shortest, economically feasible, safest in terms of natural disaster risk, and functionally with a wide-range service area. The route has a 502 km length, connecting 3 adjacent cities with Kabul and Kandahar cities. About 470.05 km of the route has a slope of less than 4%, while 30.35 km and 1.93 km have 4-10% and more than 10%, respectively. The results of the study will enable transportation planners to conduct a detailed investigation in the field using the HSR suitability map and conduct a topographical survey around the generated route for determining the centerline of the route. Furthermore, the results can be a good source of information for landuse planners for land readjustment and future landuse development.

**Keywords:** High-speed rail, Geographical Information Systems, Fuzzy-AHP, Multi-criteria decision analysis, Optimal rail route.

# ÖZET

## CBS, UZAKTAN ALGILAMA VE ÇOK KRİTERLİ KARAR VERME ANALİZİ TEKNİKLERİNİ KULLANARAK OPTİMUM YÜKSEK HIZLI TREN GÜZERGAHI SEÇİMİ

Suhrabuddin NASERY

Uzaktan Algılama ve Coğrafi Bilgi Sistemleri Anabilim Dalı

Eskişehir Teknik Üniversitesi, Lisansüstü Eğitim Enstitüsü, Ocak 2022

Danışman: Doç. Dr. Uğur AVDAN

Yüksek hızlı trenler (YHT), seyahat süresinin azaltılması, düşük seyahat maliyetleri, zaman tasarrufu ve çevre açısından en verimli ulaşım türüdür. En uygun YHT güzergâh seçimi, dikkate alınması gereken çeşitli faktörleri içeren çok önemli ve karmaşık bir süreçtir. Coğrafi bilgi sistemi (CBS) ve uzaktan algılamanın (UA) çok kriterli karar verme analizi (ÇKKVA) teknikleri ile entegrasyonu, yollar, demiryolları, YHT vb. farklı yönlendirme problemlerinde kullanılmıştır.

Bu çalışmada, Afganistan'daki Kabil ve Kandahar şehirleri arasında en uygun YHT rotasını oluşturmak için CBS tabanlı bir ÇKKVA yöntemi benimsenmiştir. YHT rota konumu üzerindeki etkili faktörler ve bunların göreceli önemi, ulaştırma sektörü uzmanları tarafından gerçekleştirilen anketlerle belirlenmiştir. YHT güzergahında etkili faktörlerin ağırlıklarını hesaplamak için bulanık analitik hiyerarşi prosesi (bulanık-AHP) ve analitik hiyerarşi prosesi (AHP) ÇKKVA yöntemleri kullanılmıştır. YHT güzergâh yer seçiminde eğim, arazi kullanımı/arazi örtüsü (AKAÖ), toprak tipleri, nehirlerden uzaklık, yollara yakınlık, yerleşim alanları/şehirlere yakınlık, heyelan riski, kar çığ riski, taşkın riski ve faylardan uzaklık etkili faktörler olarak değerlendirilmiştir. Heyelan, kar çığ ve sel duyarlılık katmanları/haritalarının türetilmesi için ayrı analizler yapılmıştır. Heyelan, çığ ve sel duyarlılık değerlendirmelerinde dikkate alınan faktörlerin ağırlıkları ve göreli önemlerini hesaplamak için bulanık-AHP yöntemi de kullanılmıştır; heyelan, çığ ve sel, YHT yönlendirmesi için faktör olarak kabul edilir.

Sonuçlar, bu çalışmada benimsenen metodolojinin, geometrik olarak en kısa, ekonomik olarak en düşük maliyetli, doğal afet riski açısından en güvenli ve işlevsel olarak geniş bir hizmet yelpazesi ile en uygun YHT rotasını başarıyla oluşturduğunu göstermektedir. Güzergâh 502 km uzunluğunda ve üç komşu şehirleri Kabil ve Kandahar şehirleriyle birleştiriyor. Güzergahın yaklaşık 470.05 km'si %4'ten az eğime sahipken, 30.35 km'si %4-10 ve 1.93 km'si %10'dan fazla eğime sahiptir. Çalışmanın sonuçları, ulaşım planlamacılarının YHT uygunluk haritasını kullanarak sahada ayrıntılı bir araştırma yapmalarını ve güzergahın merkez çizgisini belirlemek için bu çalışmadaki oluşturulan güzergâh etrafında topoğrafik araştırma yapmalarını sağlayacaktır. Ayrıca, elde edilen sonuçlar arazi yeniden düzenlemesi ve gelecekteki arazi kullanım gelişimi için arazi kullanım planlamacıları için iyi bir bilgi kaynağı olabilecektir.

**Anahtar Sözcükler:** Yüksek hızlı tren, Coğrafi Bilgi Sistemleri, Bulanık-AHP, Çok kriterli kara verme analizi, Optimum tren güzergahı.

## ACKNOWLEDGEMENTS

First and foremost, I thank Allah (Allah Subhanahu Wa Ta'ala) for giving me the opportunity, knowledge, capability, and perseverance to complete this thesis successfully.

Secondly, I would like to express my sincere appreciation to my supervisor, Assoc. Prof. Dr. Uğur AVDAN, for his invaluable contribution throughout this thesis. Your insightful suggestions pushed me to sharpen my thinking and brought my work to a higher level. Without his support, this study could not have reached its goal.

I would like to extend my sincere thanks to each of the members of my thesis committee, Prof. Dr. Saye Nihan ÇABUK, and Assoc. Prof. Dr. Hakan Ahmet NEFESLİOĞLU who have provided me extensive professional guidance and for taking the time to evaluate my thesis, taught me a great deal about both scientific research and life in general. I am extremely grateful to Assoc. Prof. Hakan Ahmet NEFESLİOĞLU who was generous with his time in completing the questionaries. I would also like to acknowledge the Turkey scholarship program for providing me with the master’s degree scholarship.

Last but not least, I must express my very profound gratitude to my parents and my beloved family, for providing me with unfailing support and continuous encouragement throughout my years of study and through the process of researching and writing this thesis; also I wish to thank my friends whose assistance was a milestone in the completion of this thesis.

Suhrabuddin NASERY

28/01/2022

## STATEMENT OF COMPLIANCE WITH ETHICAL PRINCIPLES AND RULES

I hereby truthfully declare that this thesis is an original work prepared by me; that I have behaved in accordance with the scientific ethical principles and rules throughout the stages of preparation, data collection, analysis and presentation of my work; that I have cited the sources of all the data and information that could be obtained within the scope of this study, and included these sources in the references section; and that this study has been scanned for plagiarism with “scientific plagiarism detection program” used by Eskişehir Technical University, and that “it does not have any plagiarism” whatsoever. I also declare that, if a case contrary to my declaration is detected in my work at any time, I hereby express my consent to all the ethical and legal consequences that are involved.

Suhrabuddin NASERY

CONTENTS

## LIST OF TABLES

# LIST OF FIGURES

## GLOSSARY OF SYMBOLS AND ABBREVIATIONS

| | | |
|---|---|---|
| % | : | Percent |
| ‰ | : | Millimeter Rise per Meter |
| °C | : | Degree Celsius |
| °E | : | Degrees East |
| °N | : | Degrees North |
| 3D | : | Three Dimensional |
| AASHTO | : | American Association of State Highway and Transportation Officials |
| ABC | : | Artificial Bee Colony |
| AHP | : | Analytical Hierarchy Process |
| Fuzzy-AHP | : | Fuzzy Analytical Hierarchy Process |
| API | : | Application Programming Interface |
| ASF | : | Alaska Satellite Facility |
| ASTER | : | Advanced Spaceborne Thermal Emission and Reflection Radiometer |
| cm/h | : | Centimeters per Hour |
| $CO_2$ | : | Carbon Dioxide |
| DEM | : | Digital Elevation Model |
| ELECTRE | : | ELimination Et Choix Traduisant la REalité |
| FAO | : | Food and Agriculture Organization of the United Nations |
| GA | : | Genetic Algorithm |
| GDP | : | Gross Domestic Product |
| GEE | : | Google Earth Engine |
| GIS | : | Geographical Information System |
| GNSS | : | Global Navigations Satellite System |
| GPS | : | Global Positioning System |
| HFLTS | : | Hesitate Fuzzy Linguistic Term Set |
| HSR | : | High Speed Rail |
| km | : | Kilometers |
| $km^2$ | : | Square Kilometer |
| km/h | : | Kilometers per Hour |
| kW/t | : | Kilowatt per Ton |

| | | |
|---|---|---|
| $ktCO_2$/year | : | Kilotons of CO2 per year |
| ILWIS | : | Integrated Land and Water Information System |
| LCC | : | Least Cost Corridor |
| LCP | : | Least Cost Path |
| LCPA | : | Least Cost Path Analysis |
| LiDAR | : | Light Detection and Ranging |
| LR | : | Logistic Regression |
| LS | : | Length of Slope |
| LST | : | Land Surface Temperature |
| LULC | : | Landuse/Landcover |
| MCDA | : | Multi-Criteria Decision Analysis |
| m/s | : | Meter per Second |
| mm/h | : | Millimeter per Hour |
| m | : | Meter |
| mm | : | Millimeter |
| MSI | : | MultiSpectral Instrument |
| N/kN | : | Newton per Kilonewton |
| NDVI | : | Normalized Difference Vegetation Index |
| NEPA | : | National Environmental Protection Agency |
| PROMETHEE | : | Preference Ranking Organization METHod for Enrichment Evaluation |
| QGIS | : | Quantum GIS |
| RS | : | Remote Sensing |
| SAGA-GIS | : | System for Automated Geoscientific Analyses GIS |
| SMCE | : | Spatial Multicriteria Evaluation |
| $T/m^3$ | : | Ton Per Cubic Meter |
| TFN | : | Triangular Fuzzy Numbers |
| TRI | : | Topographic Ruggedness Index |
| TWI | : | Topographic Wetness Index |
| UAV | : | Unmanned Aerial Vehicle |
| USGS | : | United State Geological Survey |
| WEI | : | Wind Exposition Index |
| WoE | : | Weight of Evidence |

# 1. INTRODUCTION

Transportation networks and infrastructures are the key ignitors for the development of a country. These infrastructures have enormous benefits, both direct such as decreasing costs, travel time, and accessibility, and indirect such as economic improvement, increasing employment, and sustainable development (Komikado et al., 2021). Transportation infrastructures are the key catalysts for several developing nations for achieving their economic aspirations, these nations have experienced quick economic growth and are planning to broadly invest in these infrastructures, such as the HSR transportation infrastructures (Komikado et al., 2021; Long, Zheng, & Song, 2018). HSRs infrastructures have made the greatest contribution to improving accessibility in Japan and China and have the major effect on travel time reduction that shrinks a continents (Komikado et al., 2021).

HSRs have an exclusive place in public transportation due to their speediness, convenience, punctuality, and being environmentally friendly (Chen et al., 2021; Li et al., 2020; Wang et al., 2019; Zhao, Zhang, & Zhao, 2021). Several countries have developed HSR technology that transports billions of passengers every year. Japan was the first country that launched an HSR system in 1964 called Shinkansen (Komikado et al., 2021; Wetwitoo & Kato, 2017). In addition, Japan has developed the most advanced and fastest rails known as Bullet and Magnetic Levitation Trains which can reach a record speed of 600 km/h. Moreover, with 29000 km of commercial HSR lines, China has the broadest HSR network in the world and plans to reach 38000 km by 2025 (Chang et al., 2019; Li et al., 2020; Wang, Acheampong, & He, 2020; Yang et al., 2019). HSR has many advantages over other transportation modes such as improving economic productivity, shaping regional economic structure, minimizing energy consumption, and decreasing greenhouse gases emissions.

HSR has both direct and indirect impacts on economic productivity by providing accessibility to fast, convenient, and cheap transportation. In the short run, it directly affects commercial delivery, business travel, and travel time reduction; in the long run, it could indirectly result in market expansion, increase potential competitiveness, change land-use patterns, and increase employment level (Jiao et al., 2020; Kim, Sultana, & Weber, 2018; Long, Zheng, & Song, 2018; Wetwitoo & Kato, 2017). For example, in Japan, the presence of HSR stations is the most prominent factor for population growth;

also, urban redevelopment is more induced in areas located near HSR stations (Wetwitoo & Kato, 2017). In addition, the prefectural productivity of Japan before 1981 shows the western shoreline as the most productive corridor; however, the productivity in the eastern part of Japan progressively improves after the expansion of the HSR network to the east region in 1982, while the prefectures outside the HSR service range remain unproductive (Wetwitoo & Kato, 2017).

Furthermore, the HSR system substantially impacts the regional economic structure in three aspects: the same-city impact, the corridor impact, and the siphoning impact (Li et al., 2020). The economic connection between adjacent cities by HSR network refers to the same-city impact that encourages regional urban integration; as a result, it ensures a much better passage of people, material, capital, and information at higher efficiency and with lower transportation and transaction costs (Asian Development Bank Institute, 2021; Li et al., 2020; Long, Zheng, & Song, 2018) which creates a space-time compression effect and promotes urban economic exchange and cooperation (Li et al., 2020; Li, Chen, & Wang, 2020). The corridor impact refers to the high accessibility of cities along the HSR line that maintains high external and inter-pair links, thus forming an economic corridor that facilitates the transportation of goods and elements, increasing the railway's carrying capacity, and ensuring a smooth and frequent economic exchange (Li et al., 2020; Long, Zheng, & Song, 2018). The siphoning impact refers to establishing HSR systems that sustain the agglomeration of funds, talents, and information to the cites located along the rail line and improve its geographic importance (Li et al., 2020; Wang et al., 2019).

Most importantly, HSR has considered the most effective and environmentally friendly mode of transportation compared to other types of transportation such as cars and aircraft (Chang et al., 2019; Yang et al., 2019). HSR has the lowest energy consumption on a per-passenger kilometer scale and emits much lower carbon dioxide ($CO_2$). The energy consumption ratio for an HSR, car, and aircraft is 1:2.4:2.8; in addition, for 600 km trip, an airplane emits 93.0 kg of $CO_2$, a car 67.4 kg of $CO_2$, and an HSR just 8.1 kg of $CO_2$ (Asian Development Bank Institute, 2021; Yang et al., 2019). The HSR carbon footprint is 8.32 times less intensive than car travel and up to 11.48 times less than aviation travel (Asian Development Bank Institute, 2021). Dalkic et al. (2017) have studied the $CO_2$ emission reduction along the Ankara-Eskisehir and Ankara-Konya HSR lines in Turkey and concluded that the $CO_2$ emission is reduced by 24.3 kilo tons of CO2 per year ($ktCO_2$/year). Yang et al. (2019) researched the impact of HSR on environmental pollution from 2003 to 2013 and found that HSR has significantly reduced environmental pollution by 7.35 percent (%). Many studies have found that HSR reduces greenhouse gases (Chang et al., 2019; Chen et al., 2021; Zhao, Zhang, & Zhao, 2021) and environmental pollution (Yang et al., 2019; Zhao, Zhang, & Zhao, 2021).

These insights on the benefits of the HSR in reducing transportation problems, improving the regional economy, and reducing $CO_2$ emissions have encouraged the development of existing HSR lines and the building of new lines in several countries across the globe over the last few decades.

## 1.1. Research Background

The HSR network substantially impacts travel patterns, landuse development, economic, social, and environmental aspects of the potential service area. It requires a massive investment in structures that are difficult to relocate once constructed. Consequently, comprehensive planning and review processes are essential for acquiring the best HSR route. The design of a rail route is a highly complex process that involves the determination of station locations, networks of lines connecting stations, track geometry, bridges, tunnels, and other system components.

The most essential element in the design phase of the HSR is route alignment selection, which has a significant impact on project costs and assures the route's efficiency in creating an economic corridor by serving the largest number of people and connecting multiple cities and regions along the route (Saat & Aguilar Serrano, 2015). In addition, by drawing relatively high numbers of ridership and generating economic activities, HSR station locations can operate as transportation hubs and grow as localized urban centers (Kim, Sultana, & Weber, 2018). HSR stations located in urban centers act as transportation nodes, lead to decentralizing regional development, and are more effective compared to stations located in suburban areas (Kim, Sultana, & Weber, 2018).

In general, the determination of route alignment and station locations is a complex and intensively iterative process that involves several factors at multiple levels. The degree of complexity increases even more when the alignment is planned in a region with complex topographical and geological features. The ideal HSR route alignment would be a direct straight and level route that would require the least amount of maintenance and produce maximum economical operation. In practice, the route should have the longest straight track, minimum gradient, and largest horizontal and vertical curves possible (Beale, 2006; Yi, 2018a). The spatial location of an HSR route alignment is tremendously influenced by topographic conditions, particularly the average natural ground slopes; Furthermore, climate, hydrology, engineering geology, soil, plants, and several other factors also affect the process (Yi, 2018b).

## 1.2. Literature Review

This chapter reviews the relevant literature on the route selection problem using GIS and MCDA techniques. The primary focus of this chapter is on the most recent literature related to the HSR route selection and a comprehensive review of the current procedures for solving the optimal route problem. This chapter is organized into three sections. The first section presents a general overview of the route selection approaches for different linear engineering structures using GIS technology and MCDA methods. The second section comprehensively accents the most recent literature related to HSR and conventional rail route optimization. The last section summarizes the overall findings from the literature review. Consequently, the most significant factors in the HSR route selection are defined and their significance and importance are evaluated.

### 1.2.1. General overview

GIS and MCDA are being used very frequently to locate an optimal route in different disciplines such as roads, highways, railways, electric transmission lines, pipelines, etc. Several studies focused on generating suitability maps as the final results (Gitau & Mundia, 2017; Kırlangıçoğlu, 2014; Kumar et al., 2017; Mohammed Sameer, Abed, & Naba Sayl, 2021; Panchal, 2017), while others have concentrated on developing a specific route or alignment (Acharya, Yang, & Lee, 2017; De Luca, Dell'Acqua, & Lamberti, 2012; Farooq et al., 2019; Godwin Muriki, Lewi Kari, 2019; Hamid-Mosaku et al., 2020; Hasanabadi, Almodaresi, & Boloor, 2018; Januadi Putra & Novia Utami, 2020; Kiema, Dang'ana, & Karanja, 2007; Kursah, 2017; Ngunyi, Mundia, & Gachari, 2017; Rao et al., 2018; Sarı & Sen, 2017; Schito, 2017; Singh, Singh, & Singh, 2019; Tarife et al., 2020; Yildirim & Bediroglu, 2019a, 2019c). Most of the studies used the least-cost path analysis (LCPA) technique and the AHP-MCDA method for generating the most optimal route. Following are some of the most recent researches associated with the optimal route selection using GIS, RS, and MCDA. The studies related to roads, highways, electric transmission lines, and pipelines are presented firstly followed by studies about conventional railways and HSR afterward.

#### *1.2.1.1. The optimal road route*

Gitau and Mundia (2017) proposed a GIS-based AHP method for modeling optimal road route selection. Slope, existing roads, rivers, air quality, towns, vegetation, LULC, settlements, and schools were considered influential factors in this study. The factors were weighted using the AHP method and overlaid in ArcGIS to generate a suitability map or cost surface; the routes were then generated manually considering this map.

Following the same approach, Rao et al. (2018) integrated slope and LULC factors to generate the shortest path using the LCP tool. The LULC layer has been generated from satellite imageries. Furthermore, the resulting optimal route's 3D (three-dimensional) model was shown for better visualization.

In a recent study, Godwin Muriki and Lewi Kari (2019) used GIS and AHP-MCDA for deriving the LCP for a road, considering population, landuse, geology, and slope factors. The factors were assigned with different weights, and a total of five potential routes were generated using the LCP tool.

In a more recent study, Singh, Singh, & Singh (2019) formulated a GIS and fuzzy-AHP model used to design and evaluate road route alignment. Environmental, social, economic, and technical spatial criteria (drainage network, road, rail, agriculture land, industrial area, urban area, rural habitation, population density, water body, trees, river, and sandbank) were considered in this study. The LCP tool (method) was applied to find four optimal routes. These routes were then evaluated and ranked using the fuzzy-AHP method to identify the best optimal route. In the end, a validation process was implemented using field survey global positioning system (GPS) points.

#### *1.2.1.2. The optimal highway route*

Sarı and Sen (2017) developed a GIS-based Hybrid AHP method for determining the most optimal highway location. They used slope, height, geology, landuse, population, distance to settlements, and distance to existing highways as practical factors in route processing. Three routes were generated using the LCP algorithm as a result of the study; economic route, environmental route, and hybrid AHP route, which considers both economic and environmental aspects.

In a subsequent study, Gärds and Oscarsson (2019) proposed the methodology for generating the least-cost corridor with 400-pixel width, instead of the LCP. They considered slope, water bodies, land cover, and proximity to buildings as criteria for the study and used AHP for weighting the criteria.

In a recent study along the same lines of research, Januadi Putra and Novia Utami (2020) presented a LCPA and MCDA method for deriving the optimal highway route. Landuse, geology, slope, and multi-hazard index variables were weighted considering three different simulations. Three different routes were generated and evaluated for optimality purposes.

In a more recent study, Mohammed Sameer, Abed, and Naba Sayl (2021) formulated a GIS and AHP MCDA method to generate an optimal highway path in a rural area. They considered slope, soil types, LULC, and hydrology as influential factors in controlling the route location. A suitability map was generated; two routes were drawn considering the map, which were then compared and evaluated with the existing highway to show the appropriateness of the method.

#### *1.2.1.3. The optimal electric transmission lines route*

Schito (2017) implemented MCDA and LCP algorithms to locate electric transmission lines. The study first computed cost surface, then least-cost corridor (LCC), after that the LCP, and finally the position of the transmission towers by simple additive weightings. In the study, six different MCDA models have been used to compute six LCPs, from which the LCC was being derived by the Kernel Density Estimation probabilistic function.

In a subsequent study, Eroğlu and Aydin (2018) proposed a Genetic Algorithm (GA) and Artificial Bee Colony (ABC) methods to generate a power transmission line route with fewer curves and smaller angles of the curves. The authors compared the result of GA, ABC, cost path, and cost distance methods and it was concluded that the ABC algorithms have better performance than the others.

In a more recent study, Tarife et al. (2020) developed a route selection model considering the built environment, natural environment, engineering environment, and simply combined perspectives to derive the LCP. They used GIS and AHP MCDA methods for weighting the criteria and generating the LCPs. For the built environment perspective only landuse criteria with 100% influence, for the natural environment perspective wetlands and land cover criteria, and for the engineering environment perspective slope and infrastructure criteria were considered; while the simply combined perspective considered all criteria at the same time and was considered as the optimal route.

#### *1.2.1.4. The optimal pipelines route*

Kursah (2017) developed a geospatial model by combining MCDA and GIS techniques to determine an LCP for a water pipeline. In this study, slope, land cover, watercourses, distance to roads, and soil types were considered factors that affect the pipeline's construction costs. Experts' opinions and literature have been used to weight the criteria and the LCP tool has been used to generate the optimal route.

In a subsequent study, Durmaz, Ünal, and Aydın (2019) proposed an automatic pipeline route finder algorithm to determine a suitable place for gas pipeline using GIS and AHP MCDA. In this study, topography, restricted areas, ridges, slopes, rivers, streams, terrain, roads, and industrial areas were considered as factors while generating the optimal pipeline route. The generated route was then compared with an already built pipeline to assess the method's effectiveness; they concluded that the algorithm had decreased the cost by 20%.

A more recent study performed by Hamid-Mosaku et al. (2020) indicates that GIS, RS, and Analytical Network Process (ANP) can be used for pipeline route selection. The authors used environmental, geological, and economic factors for determining the optimal route for gas and oil pipelines using the LCP tool. Furthermore, Landsat8 imageries were utilized to produce LULC map.

### 1.2.2. State-of-the-art railway route optimization

#### *1.2.2.1. The optimal conventional rail route*

Kiema, Dang'ana, and Karanja (2007) implemented GIS and MCDA methods for generating optimal rail routes in Kenya, Sudan. Slope, soil types, proximity to rivers, LULC, important towns and cities, and forbidden areas were the factors considered in this study. These factors were rasterized and reclassified using ArcGIS software and were weighted using the AHP method. These layers were overlaid using ArcGIS software to produce a cost surface raster. The cities across the source and destination points were considered intermediate stations. Therefore, different cost distance and cost direction rasters were generated for each route, and the LCPA was performed to generate optimal routes. The results included four alternative optimal routes; these routes were evaluated based on cut/fill volume, route length, environmental issues, intersection with rivers, and intersection with roads; the best optimal route was then selected.

In a subsequent study Kosijer, Marković, and Belošević (2012) proposed an MCDA method for the most favorable railway route planning and design based on predetermined criteria and real-life restrictions. The MCDA method was illustrated in detail, and the idea of weighting was described. Four alternative routes were evaluated considering four different scenarios: equal weighting all criteria, economic-based route, traffic and transportation-based route, and space-related and environmental based route. The VIKOR (VIseKriterijumska Optimizacija I Kompromisno Resenje, that means: Multicriteria Optimization and Compromise Solution) MCDA method was used for deriving weights for criteria. The criteria were railway construction investment, railway operation, and maintenance, railway line capacity, effects the railway will have on physical development and influence of railway on the living environment.

A thesis study performed by Kırlangıçoğlu (2014) indicates that GIS, RS, and MCDA methods are reliable and robust for finding the most suitable location for a HSR route. The study considered 12 factors affecting the routing process. The relative importance of these factors was determined by the questionnaires filled out by railway engineers, road transportation engineers, and economic experts, which makes it a very detailed study. The factors considered were as follow: travel demand, land ownership, integration into other transportation systems, population density, distance to sites, compliance with the lithological structure, topography, distance to water bodies, proximity to industrial and commercial areas, proximity to public and educational institutions, distance to faultlines, and proximity to public housing areas. The study explained the effect of each factor on the route selection process in great detail. Some of the factors were generated from the combination of other subfactors. All the 12 factors were overlaid considering their weights, derived from AHP analysis, using GIS software to generate cost surface raster. Alternative routes were drawn by hand over the cost raster considering the most optimal areas visually. The cost surface raster was then compared with existing rail routes and under construction routes to check the accuracy of the method, the results showed that the existing routes and under construction routes have a very good harmony with the cost surface raster.

Following the same approach, Ngunyi, Mundia, & Gachari (2017) proposed a GIS-based rail route selections method and considered environmental and engineering factors and a combination of these two as factors for the routing process. Experts fill out questionnaire forms to evaluate the relative importance of the factors and the weight for each factor was determined using the AHP method. The study used slope, land cover, proximity to towns, geology, soil map, proximity to existing roads, proximity to rivers, and proximity to protected areas as factors affecting the route's location. The layers of the factors were rasterized, reclassified, and were overlaid in the ArcGIS environment. The cost distance and cost direction raster were generated and used to derive three alternative routes using the LCP tool.

Similarly, Panchal (2017) formulated a method using GIS and MCDA to generate a cost map used for manually planning a rail route over it. The factors considered in this study were slope, proximity to city and village, proximity to streams, gradient, lithology, soil type, proximity to roads, and land cover. The factors were weighted using the AHP method, and ArcGIS is used to perform the overlay process of the data layers. The result was a feasibility map or cost surface raster used for route planning manually.

Using the same technique, Acharya, Yang, and Lee (2017) used topography and land cover maps separately to produce optimal routes using GIS. Slope, distance to rivers (derived from digital elevation model), distance to ridges (derived from digital elevation model), and LULC were used as factors affecting the final route. Four different scenarios were considered for the route, and the slope has the highest weight in all the scenarios. The factors' wights were specified using the AHP method and the data layers are overlaid in ArcGIS to generate cost surface raster. The LCPA was performed on the cost surface layer, and four routes were generated, and a comparison was made between them.

Another case study performed by Kumar et al. (2017) indicates that GIS and MCDA have the potential to accurately map an optimal route for a railway in hilly regions based on the planner's perceptions. The factors that have been used in the study were land cover, slope distance to roads, distance to drainage distance to power lines, and geology. All criteria were categorized into subcategories considering hilly region conditions. The weights were calculated using the AHP method, and the final cost surface was generated by overlaying all criteria layers. The resulted feasibility map was categorized into extremely, highly, moderately, and least feasible areas.

Along the same lines of research, Hasanabadi, Almodaresi, and Boloor (2018) implemented GIS, Integrated Land and Water Information System (ILWIS), and MCDA methods to determine the best optimal rail route. They considered slope, proximity to residential areas, faults limitations, ecological limitations, railway station points, LULC, and proximity to existing roads criteria in this study. The data layers of the criteria were rasterized and reclassified for standardization purposes. The weights for the criteria were calculated using the AHP method and the overlay operation has been done in ILWIS software, and the results were converted to ArcGIS supportable format. The LCPA has been performed in the ArcGIS environment for extracting the best optimal rail route.

#### *1.2.2.2. The optimal high-speed rail route*

De Luca, Dell'Acqua, and Lamberti (2012) proposed a method for optimizing the HSR line using GIS and MCDA techniques. Three alternative route scenarios (conservative, compromise, and innovative) were evaluated for economic feasibility and social and environmental impacts. In this study, the following factors have been considered: geological, hydrology, natural resources, landuse, future landuse, and geometry of the route. The AHP method was used for weighing the factors; based on the evaluations, the best optimal route was considered the conservative route.

Following the same approach, Saat and Serrano (2015) implemented GIS and MCDA methods for optimization of HSR routes based on economic feasibility. The study was completed in two steps. The first step was origin to destination analysis which is used to identify high-potential city pairs to be connected by HSR in Malaysia. Three criteria, metropolitan/population size, economic productivity, and distance were used to rank the pairs, and three main corridors were identified for further investigations. In the second step, the resulting corridors were evaluated using ELECTRE 1 (ELimination Et Choix Traduisant la REalité) method considering construction costs, potential users from the cities nearby, and gross domestic product (GDP) geometric mean for the cities criteria. It was concluded that the alternative route (southbound from Kuala Lumpur to Singapore) is better than the other routes; the routes were planned to be built alongside the existing roads or railways.

Another case study performed by Yildirim & Bediroglu (2019b) indicates that the GIS-based MCDA model is efficient for determining an economical and engineering feasible HSR route. The study used the AHP and LCPA methods to determine the optimal HSR route. Slope, geology, soil quality, rivers, protected areas, roads, land cover, and lakes were considered as influential factors in this study. The data layers were overlaid using ArcGIS to generate cost surface raster, and LCPA was then performed on the cost surface for generating the optimal route. In the end, a sensitivity analysis was performed to see the behavior of the LCPA when changing the weights of the factors. The generated optimal route was compared with an already planned route which showed resemblances.

In a subsequent study, Farooq et al. (2019) proposed a GIS-based MCDA method for generating alternative HSR routes using the AHP and Preference Ranking Organization METHod for Enrichment Evaluation (PROMETHEE II). The AHP method was applied to determine wights of criteria, while the PROMETHEE II technique was used to select the most optimal route among the generated routes. The study was conducted in two stages. The first stage deals with identifying the suitable locations for stations, elevation mode, slope percentage, and preparing a proposal for a new railway line between the cities by using ArcGIS and ERDAS IMAGINE software. Satellite datasets such as Landsat 8 and the Advanced Spaceborne Thermal Emission and

Reflection Radiometer (ASTER) digital elevation model (DEM) were mosaicked to represent the study area. ERDAS IMAGINE and ArcGIS software were used to create and process the data layers. Furthermore, different map layers such as settlement percentage, slope, elevation, and vegetation percentage were formed for a feasibility assessment of the routes. In the second stage, the route alternatives were defined, and the best optimal route was selected considering the travel time, number of train stops, transport satisfaction, number of seats/days, connectivity, operating costs, profit, and payback period criteria. The weights of the criteria were defined using the AHP method and were fed into PROMETHEE II to determine the best alternative route. As a result, six alternative routes were generated, and route number 5 was considered the most optimal route.

In a recent study, Yildirim & Bediroglu (2019c) integrated GIS and AHP for generating an optimum HSR route considering economic and environmental concerns (criteria). They considered slope, geology, soil quality, rivers, protected areas, roads, land cover, and lakes as factors. The weights for the factors were derived from the AHP method, and the LCP tool with a novel GIS extension was used for generating the optimal HSR route. They generated the optimal route, which could decrease construction costs by about 12% compared to the current under-construction route in the area. A sensitivity analysis was performed to check the efficiency of the extension.

### 1.2.3. Summary

The literature appraised in this thesis are published in international journals. The stat-of-the-art in the HSR route selection was covered in the literature review to show a comprehensive picture of the problem and discover the most frequently used methods, factors (criteria), tools, and software. The following findings have been concluded from the literature review section:

- Most of the studies have used the AHP method for calculating the weights of the criteria and the LCP tool for generating the optimal route.
- Many studies have applied a GIS-based MCDA method to compare several alternative routes with each other and select the most optimal one.

- Some studies focused on generating optimal routes based on specific concerns such as economic, environmental, engineering, etc.
- All the studies have confirmed the suitability and capability of the GIS-based MCDA method for solving the highways, roads, electric transmission lines, conventional railways, and HSRs routing problem.
- Several factors (criteria) have been considered in these studies. Some studies have used similar factors; however, most have utilized different factors with no similarity in the geographical context, and some have considered very few factors.
- Most of the studies have used literature review to determine the criteria relative importance, while some others did not mention any source for pairwise comparison of the criteria.
- Among the studies, only (Kırlangıçoğlu, 2014) has performed a survey for determining the relative importance of the criteria.
- Lake of comprehensive technical specifications to demonstrate all details and requirements for an HSR route location selection.

The most significant factors for selecting the HSR route location are selected through the above comprehensive literature review, transportation sector experts' opinions, HSR alignment technical specifications, reports, and manuals. The application of these factors in determining the optimal HSR route location and direction is critical because they are directly related to the geometrical specifications of the HSR alignment, topographical situation, and metrological condition of the study area. In this thesis, slope, LULC, geology (soil types), distance from rivers, proximity to roads, proximity to towns/cites, distance from historical sites and protected areas, and natural disaster risk (landslide, snow avalanche, flood, and earthquakes) are considered as the most prominent factors for selecting the optimal HSR route. HSRs and conventional railways are endangered by natural disasters such as earthquakes, landslides, snow avalanches, glacial debris, floods, gale, hurricanes, and forest fires (Ding et al., 2020; Janic, 2015; Qizhou, Xin, & Lishuang, 2021; Voumard, Derron, & Jaboyedoff, 2018; Zhao, Liu, & Wang, 2020). The number and types of natural disaster risks to the HSR route can be different in distinct geographical areas with unique geological structures. The significance of the factors is explained in the section 4.1 in detail.

### 1.3. Problem Statement

Generally, locating the HSR route alignment has two principal phases, the first phase deals with the determination of the general route, while the second phase involves engineering design and improvement of the route (Asian Development Bank Institute, 2021; Indian Ministry of Railways, 2020; Medrano, 2016). There are two types of survey techniques for selecting the HSR route, which are currently being practiced broadly, namely conventional and modern survey methods (Indian Ministry of Railways, 2020; Padaya, Juremalani, & Prakash, 2017).

Selecting the HSR route using conventional survey methods is a tedious and time-consuming process that provides only topographical data, requires tremendous manual processing of a large amount of data, has data collection difficulties at inaccessible locations, and must address numerous environmental issues (Indian Ministry of Railways, 2020; Padaya, Juremalani, & Prakash, 2017; Wahdan et al., 2019). Furthermore, in the conventional method, initial planning is only carried out based on the topographical maps in different scales and contour intervals which does not account for all the above factors (Indian Ministry of Railways, 2020; Padaya, Juremalani, & Prakash, 2017). This oversimplification leads to selecting a few candidate routes for further analysis before choosing a final route which poses an obvious risk to achieving an optimal HSR route that accounts for all relevant factors.

Thus, employing modern survey methods that account for several factors at the same time and can generate several alternatives, are more reliable, time saving, and cost effective. Modern survey methods are rapidly developed with the advancement in the technologies like GNSS (Global Navigations Satellite System), LiDAR (Light Detection and Ranging), Aerial Photogrammetry from aircraft and UAV (Unmanned Aerial Vehicle), satellite imagery, etc. that have changed the manner of determining dimensions and contour of the Earth’s surface (Indian Ministry of Railways, 2020). Moreover, modern survey methods are based on RS and GIS technologies that need less human resources, cost, and time (Indian Ministry of Railways, 2020; Wahdan et al., 2019). Integration of GIS and MCDA offer a powerful capability to perform complex calculations based on human-oriented evaluations through weighing different criteria and generate the most optimal route. MCDA is a way to synthesize a variety of inputs (criteria) and helps focus on what is essential, logical and consistent, and easy to use among the alternatives or criteria (Greene et al., 2011; Keisler & Linkov, 2021; Padaya, Juremalani, & Prakash, 2017). Conclusively, GIS-based MCDA applications support complex decision making with multiple objectives and provide strong support for locational assessment of an optimal HSR route alignment (Farooq et al., 2019; Greene et al., 2011; Keisler & Linkov, 2021; Wahdan et al., 2019; Yildirim et al., 2016; Yildirim & Bediroglu, 2019b).

In this thesis, Afghanistan is selected as study area due to absence of modern survey methods applications for route selection, high costs of conventional methods, complex topography of the area, high demand for affordable and convenient transportation mode, its' strategic location, and to encourage other researchers adopt new technologies in their researches. The Kabul to Kandahar corridor is selected for implementing the method for selecting the optimal HSR route. More than 8.5 million population are travelling and trading through this corridor (National Statistics and Information Authority, 2020). Most of Afghanistan exports and a significant amount of imports are happening through this corridor with the neighboring countries (Ministry of Industry and Commerce, 2020).

### 1.4. Research Aim and Objectives

Given the background and limitations of the state-of-the-art in the HSR route planning process identified above, this research aims to develop a practical modern survey method to select the best optimal HSR route considering the influencing factors using GIS, RS, and MCDA techniques between Kabul and Kandahar cities in Afghanistan. Even though this study investigates only particular part of Afghanistan, the author believe that the methodology can be adopted in different geographical areas and the findings will of global interest. The following five objectives have been formulated to achieve this aim.

1. To introduce a more effective, accurate, cost-effective, and modern survey method for solving the route selection problem.
2. To find economically and geometrically the most optimal route.
3. To apply different MCDA methods for weighing the criteria and ranking the alternatives; accordingly, evaluating their effectiveness, accuracy, and assessing their results in the study area.

4. To generate the shortest possible route by implementing LCPA.
5. To optimize an HSR route with a wide-range service area to serve the greatest number of populations.
6. To identify the safest route in terms of natural disaster risks by carefully assessing the study area.

### 1.5. The Novelty of the Study

The methodology adopted in this study for selecting the optimal HSR route is a modern survey method based on the GIS, RS, and MCDA techniques and has many advantages compared to conventional survey methods. Conventional survey methods require extensive time, tremendous manual work, lack of data in a remote location, and planning based on only topographical maps (Indian Ministry of Railways, 2020; Padaya, Juremalani, & Prakash, 2017; Wahdan et al., 2019). Furthermore, this method avoids oversimplification in route selection by considering every possible route from origin to destination concerning multiple criteria, where most factors exhibit a high satisfaction degree.

Most importantly, this study contemplates the risk of the natural disaster that is crucial for every transportation infrastructure, especially the HSR route, to operate safely and efficiently. In addition, a natural disaster causes loss of lives and money. Natural disasters risk such as landslides, snow avalanches, floods, and earthquakes are highlighted in this study which have not been considered in most of the studies conducted on conventional and HSR route selection (Acharya, Yang, & Lee, 2017; Al-Hameedawi et al., 2018; Farooq et al., 2019; Kiema, Dang'ana, & Karanja, 2007; Y. Kumar et al., 2017; Ngunyi, Mundia, & Gachari, 2017; Panchal, 2017; Yildirim & Bediroglu, 2019b), the only study which has considered earthquake risk among natural disasters was conducted by (Hasanabadi, Almodaresi, & Boloor, 2018). On the other hand, the study has considered the most appropriate slope classification in respect to the HSR alignment technical specifications and reports. Most of the studies have adopted very exaggerative slope classification for HSR and conventional rail routes, which are not practically possible for an HSR or conventional rail to operate. Yildirim and Bediroglu (2019b) used slopes 0-5°(0-8.75%) and 5-10° (8.75-17.63%), and Farooq et al. (2019) considered slopes 0-5% and 5-8%, as the highly suitable slopes for HSR route, while the maximum gradient applicable for HSR route is less than 4% (Yi, 2018a). In addition, soil types that is one of the important factors in the construction phase and has a tremendous impact on the project costs, are considered in only three studies by Kiema, Dang'ana, and Karanja (2007), Ngunyi, Mundia, and Gachari (2017), and Yildirim and Bediroglu (2019b). To the best of the authors' knowledge, it's the first research conducted using GIS, RS, and MCDA techniques for the determination of an HSR route in the study area.

## 1.6. Structure of the Thesis

The thesis structure is outlined in 8 chapters.

**Chapter 1: Introduction**

This chapter explains the background of HSR route and station locations importance, defines the problem, states the aim and objectives of the research, and the novelty of the study.

**Chapter 2: Literature Review**

This chapter reviews the state-of-the-art in the HSR route selection. The review aims to find the scientific gaps and limitations in the previous studies for further improvement. Furthermore, the review represents various methods for evaluating criteria and alternatives considering different constraints to obtain the objective solution to the problem.

**Chapter 3: Study Area**

This chapter focuses on representing the transportation importance characteristics of the study area and a short introduction to the geographical location, economic situation, geological structures, and metrologically condition of the study area.

**Chapter 4: Materials**

This chapter focuses on the importance and significance of the required materials and data for the HSR route selection problem. Moreover, the sources of the data and methods of acquiring/generating the data layers are also discussed.

**Chapter 5: Research Methodology**

This chapter thoroughly discusses the methods used in this research for the HSR optimal route selection process. The AHP and fuzzy-AHP methods, used for weighing the criteria, are described. In the end, the GIS least-cost path (LCP) tool/method and its application process are clarified in detail.

**Chapter 6: Results**

This chapter includes all data processes and the results obtained from them. The results are presented for all factors considered in the study as well as the results for the optimal HSR route.

**Chapter 7: Discussion**

This thesis chapter discusses the resulted optimal route in terms of its location and characteristics, considering the criteria defined earlier. In addition, the results for the factors which are considered for HSR route selection are also discussed in detail.

**Chapter 8: Conclusion and Recommendations**

The final chapter of this thesis summarizes the findings and describes its contributions to different disciplines. Moreover, the study's limitations are highlighted, and specific recommendations have been given for future works.

## 2. STUDY AREA

The HSR route researched in this thesis connects Kabul city in Kabul province with Kandahar city in Kandahar province, the two largest cities in Afghanistan (Figure 2.1). These cities are Afghanistan's transportation and economic hubs, and most of the southern and western provinces of Afghanistan are traveling through Kandahar to Kabul and contrariwise. A highway connects these cities with approximately 482 km (300 miles) length, passing through Maidan Wardak, Ghazni, and Zabul provinces (Haqmal, Kaur, & Nasir, 2019; Schubert, 1991; Stinson et al., 2016). U.S. Army Corps of Engineers has constructed this highway from 1960 to 1967 (Schubert, 1991). The Highway alignment and grade had been determined photogrammetrically and had been staked out in the field, but no on-the-ground survey had been done (Schubert, 1991).

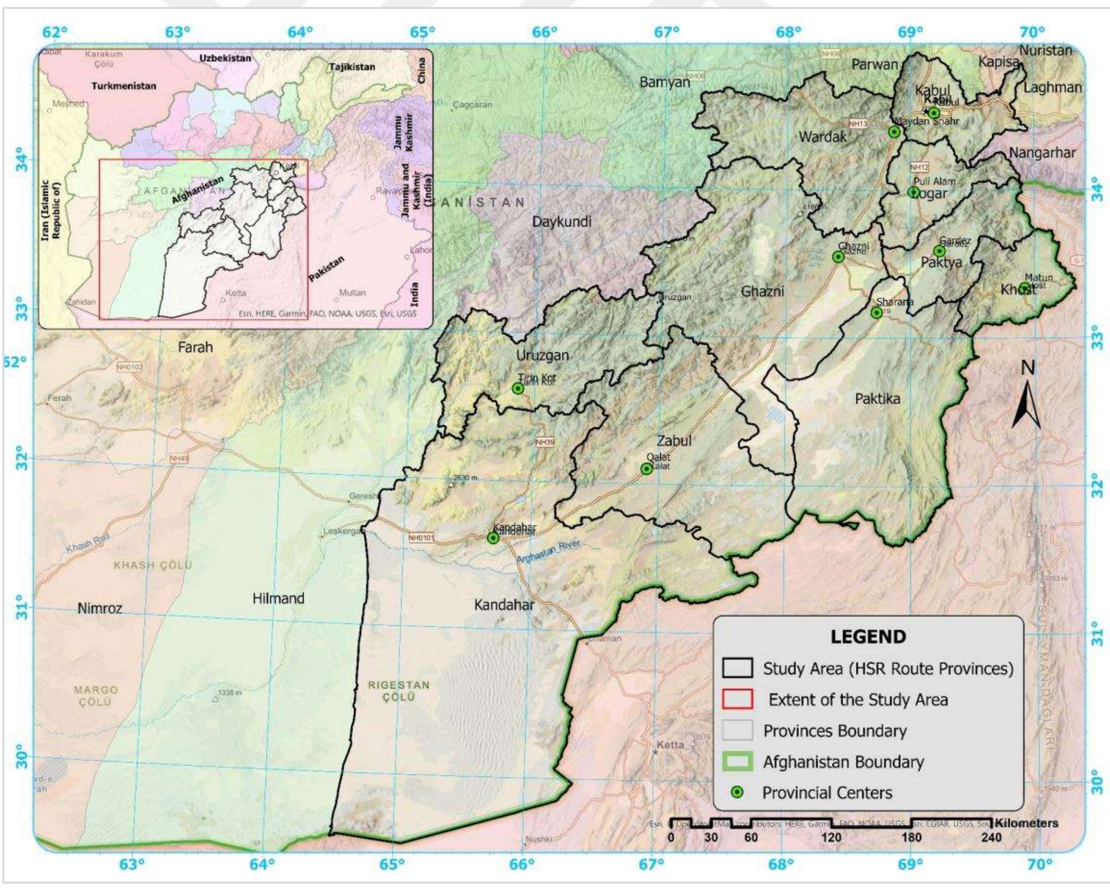


**Figure 2.1.** *The local and regional location of the study area*

Kabul province has 4524 km$^2$ area while Kandahar province has 54845 km$^2$ area with 5.21 million and 13.99 million populations, respectively (National Statistics and Information Authority, 2020). On the other hand, Maidan Wardak, Ghazni, and Zabul provinces have 10348 $km^2$, 22461 $km^2$, and 17472 $km^2$ areas and 0.66 million, 1.36 million, and 0.38 million populations, respectively (National Statistics and Information Authority, 2020).

### 2.1. Metrological Conditions and Natural Disaster Risks

Afghanistan has a continental climate with harsh winters and hot summers, where the average temperature in January is below -15°C and over 35°C in summer (National Environmental Protection Agency, 2019). According to the climate change analysis performed by the National Environmental Protection Agency (NEPA) of Afghanistan, based on two scenarios, the mean temperature is expected to rise 1.5°C, and 3°C until 2030 and 2050, respectively (National Environmental Protection Agency, 2019). This shows that there will be more floods and landslides all over the country. Therefore, the natural disaster risk should be strictly considered in future studies, projects, and planning.

In August 2020, heavy rainfall floods hit 14 provinces of Afghanistan, including Kabul, Maidan Wardak, and Ghazni (Afghan Red Crescent Society, 2021), which are on the HSR route. Based on the World Bank report in 2017, the flood risk is high along the rivers in Maidan Wardak, Ghazni, Zabul, and Kandahar, while the risk is very high in Kabul (The World Bank, 2017). The earthquake risk is high along the Kabul-Kandahar road, while the landslide risk is moderate to low, but some areas in Maidan Wardak, Ghazni, and Zabul are prone to high risk (The World Bank, 2017). In addition, snow avalanche risk is high in Kabul, Maidan Wardak, Ghazni, and Zabul provinces (The World Bank, 2017).

### 2.2. Economic Importance

The Kabul-Kandahar route is crucial for the economy of Afghanistan and plays a crucial role in Afghanistan's economic development, and acts as an economic corridor (Ministry of Industry and Commerce, 2020). According to statistics, about 80% of Afghanistan's exports are happening through this route to India, Pakistan, China, and Iran (Ministry of Industry and Commerce, 2020).

# 3. RESEARCH METHODOLOGY

This chapter comprehensively discusses the research methods adopted in this thesis and presents a practical approach to select the optimal HSR route. The methods adopted in this thesis are AHP and fuzzy-AHP. The relative importance of the most significant factors in HSR route location selection are defined by questionaries filled out by transportation sector experts. Afterward, the AHP and fuzzy-AHP methods are used for calculating the weights of the factors. Considering AHP and fuzzy-AHP weights of the factors, the weighted linear combination analysis is performed to generate the cost rasters or suitability maps, after that the cost rasters are subjected to LCPA for generating two alternative routes, the AHP alternative and the fuzzy-AHP alternative. A comparative analysis between these two routes is performed to derive the optimal HSR route.

In this study, landslide risk, snow avalanche risk, and flood risk are considered as influential factors on HSR route location; due to lack of data layers for these three factors, three separate analyses are conducted to generate the layers. The landslide susceptibility, snow avalanche susceptibility, and flood susceptibility analyses are performed using a GIS-based fuzzy-AHP method. The relative importance of the affective factors for each of them are specified using questionaries performed by hydrology and geology experts. The fuzzy-AHP method is used for calculating the weights of the factors for the factors related to landslide, snow avalanche, and flood susceptibility; considering their weights, the weighted linear combination analysis is performed to generate the susceptibility maps. For clarification purposes, the AHP and fuzzy-AHP methods are explained in separate sections in detail.

In addition, ArcGIS Pro software, version 2.8, was employed for processing the data and creating the necessary cost surfaces for deriving the optimal HSR route and landslide, snow avalanche, and flood susceptibility maps using the methods mentioned above. The tools employed in the processing stage are illustrated thoroughly to clarify the background processing mechanism of the tools.

Furthermore, Quantum GIS (QGIS) software was utilized for calculating the Length of the Slope, Topographic Ruggedness Index (TRI), Topographic Wetness Index (TWI), and Wind Exposition Index (WEI) factors. Normalized Difference Vegetation Index (NDVI), Precipitation, and Land Surface Temperature (LST) parameters were analyzed in Google Earth Engine (GEE) geospatial Application Programming Interface (API). The general workflow of the study and data processing steps can be seen in Figure 3.1.

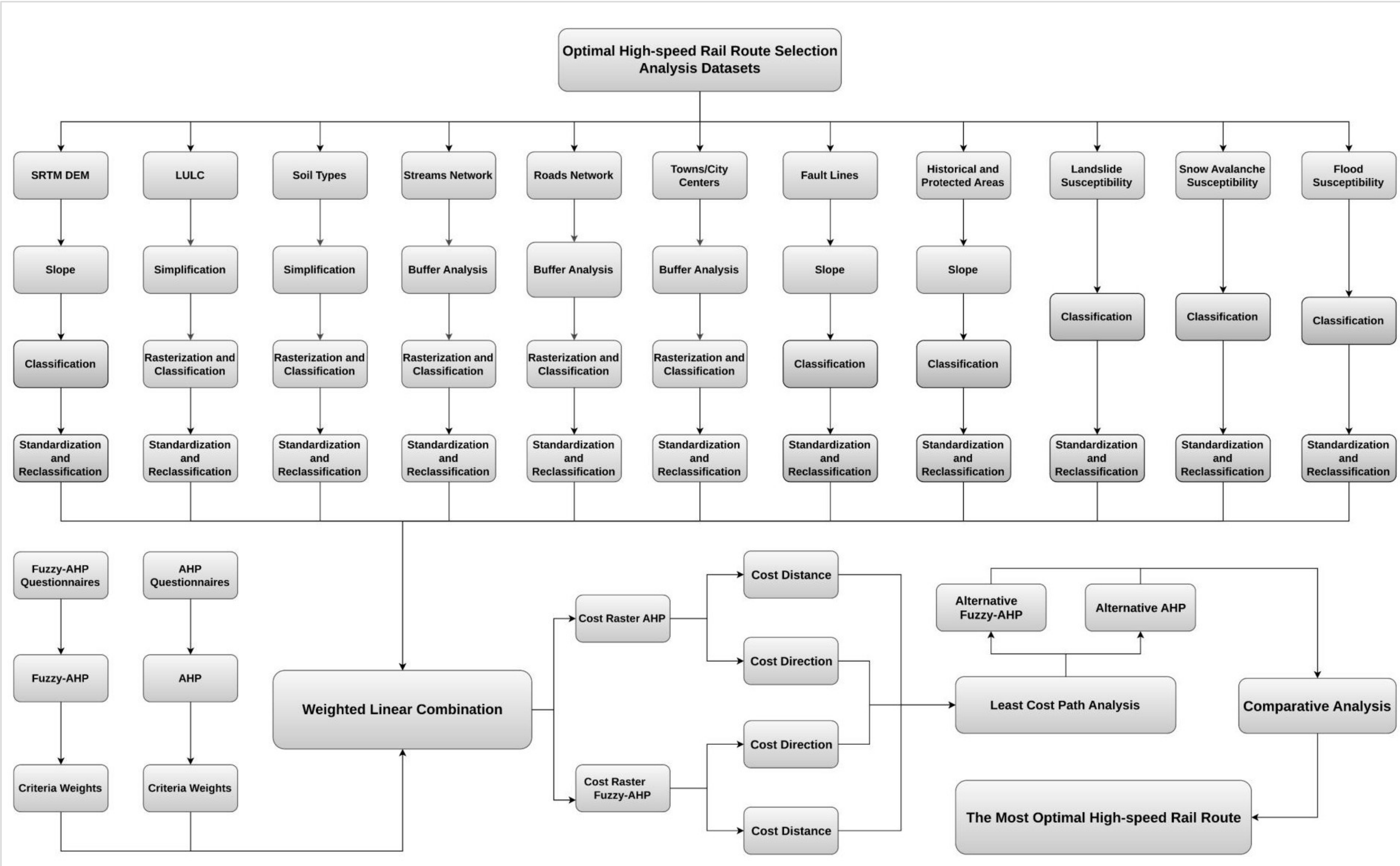


**Figure 3.1.** *The general workflow of the study for selecting the optimal HSR route*

### 3.1. Analytical Hierarchy Process

The AHP is extensively utilized in different disciplines and is one of the most popular multicriteria methods. AHP can analyze and organize complex decisions by deconstructing them into a hierarchical structure (Saaty, 1988). This method is based on pair to pair comparison of parameters/alternatives, organized in a matrix called the judgment matrix (Saaty & Vargas, 1980). This method can be employed to rank a group of parameters/alternatives or select the most optimal or the best alternative in a group (Saaty, 1988).

This method can be implemented in the following six steps (Saaty & Vargas, 1980):

1- Splitting the problem into component parameters.

2- Organizing these parameters in hierarchical order.

3- Generating $n \times n$ dimensional pairwise comparison matrix for parameters (Equation 1).

$$A = \begin{bmatrix} a_{1j} & \dots & a_{1j} & \dots & a_{1n} \\ \vdots & \dots & \vdots & \dots & \vdots \\ a_{ij} & \dots & a_{ij} & \dots & a_{in} \\ \vdots & \dots & \vdots & \dots & \vdots \\ a_{n1} & \dots & a_{nj} & \dots & a_{nn} \end{bmatrix} \quad (1.3)$$

Where $A$ is the pairwise comparison matrix, $a_{ij}$ is the importance of the $i^{\text{th}}$ criterion over the $j^{\text{th}}$ criterion, and $n$ is the numbers of criteria.

4- Assigning Saaty's importance scale values from 1 to 9 based on the relative importance of parameters (Table 3.1), performing a comparison for the upper diagonal value is sufficient as the lower diagonal values can be calculated using a reciprocal operation.

**Table 3.1.** *The relative importance scale of criteria proposed by* (Saaty, 1977)

| IMPORTANCE | DEFINITION/EXPLANATION |
|---|---|
| **1** | The two factors are equally important |
| **3** | One factor is slightly more important than the other |
| **5** | One factor is more strongly important than the other |
| **7** | One factor is very strongly important than the other |
| **9** | One factor is extremely more important than the other |
| **2,4,6,8** | The importance of the in-between value of adjacency determination is represented |

5- Weight calculation for each parameter can be performed by calculating the principal eigenvectors using Equation 2, constructing the normalized pairwise comparison matrix (Equation 3), and calculating the weight vector (weights of the parameters) by calculating the arithmetic mean of the principal eigenvectors (Equation 4).

$$b_{ij} = \frac{a_{ij}}{\sum_{i=1}^{n} a_{ij}} \quad ,j = 1, 2, \dots, n \tag{2.3}$$

Where $b_{ij}$ is the principle eigenvector of the $i^{\text{th}}$ criterion, $a_{ij}$ is the importance of $i^{\text{th}}$ over the $j^{\text{th}}$ criterion, and $n$ is the numbers of criteria.

$$C = \begin{bmatrix} c_{1j} & \cdots & c_{1j} & \cdots & c_{1n} \\ \vdots & \cdots & \vdots & \cdots & \vdots \\ c_{ij} & \cdots & c_{ij} & \cdots & c_{in} \\ \vdots & \cdots & \vdots & \cdots & \vdots \\ c_{n1} & \cdots & c_{nj} & \cdots & c_{nn} \end{bmatrix} \tag{3.3}$$

Where $C$ is normalized pairwise comparison matrix, $c_{ij}$ is the normalized importance value of the $i^{\text{th}}$ criterion over the $j^{\text{th}}$ criterion, and $n$ is the numbers of criteria.

$$w_i = \frac{\sum_{j=1}^{n} c_{ij}}{\mathrm{n}} \quad ,i = 1, 2, \dots, n \tag{4.3}$$

Where $w_i$ is the weight vector of the $i^{\text{th}}$ criterion, $c_{ij}$ is the normalized importance value of the $i^{\text{th}}$ criterion over the $j^{\text{th}}$ criterion, and $n$ is the numbers of criteria.

6- The consistency ratio of the pairwise comparison matrix can be calculated: by multiplying the weight vector by the pairwise comparison matrix, deriving vectors of the new matrix, calculating the eigenvalues for each parameter through dividing these vectors by weights of parameters, calculating the principal eigenvalue ($\lambda_{max}$) by calculating the arithmetical mean of the total eigenvectors, calculating the consistency index (Equation 5), and calculating the consistency ratio by implementing Equation 6.

$$CI = \frac{\lambda_{max} - n}{n-1} \tag{5.3}$$

where $CI$ is the consistency index, $\lambda_{max}$ is the principal eigenvalue and *n* is the number of parameters.

The consistency ratio should be less than 0.1 or 10%; Otherwise, the matrix has inconsistencies and must be revised (Saaty, 1988).

$$CR = \frac{CI}{RI} \tag{6.3}$$

Where *CR* represents the consistency ratio and *RI* the random index, random index is given by Saaty (1988) and can be chosen based on the number of parameters (Table 3.2).

**Table 3.2.** *The random index values proposed by* (Saaty & Vargas, 1980)

| n | 1 | 2 | 3 | 4 | 5 | 6 | 7 | 8 | 9 | 10 | 11 |
|---|---|---|---|---|---|---|---|---|---|---|---|
| **RI** | 0 | 0 | 0.58 | 0.90 | 1.12 | 1.24 | 1.32 | 1.41 | 1.45 | 1.49 | 1.51 |

### 3.2. Fuzzy Analytical Hierarchy Process

The fuzzy-AHP method is an extension of the classical AHP method that can decrease the vagueness and uncertainty of human judgment (Liu, Eckert, & Earl, 2020; Malczewski & Rinner, 2015; Nasery & Kalkan, 2021). This method is based on fuzzy logic derived from the fuzzy sets theory first introduced by Zadeh (1965). Most of the time, in a complex problem with several criteria/alternatives, the decision-maker's judgments have fuzziness, vagueness, and uncertainty as they cannot decide on the crisp value to be allocated for a criteria/alternative (Kahraman, 2008; Liu, Eckert, & Earl, 2020; Nasery & Kalkan, 2021; Patil, 2018; Zadeh, 1988). Fuzzy logic can realistically reflect human judgment style and reasoning (analysis, interpolation, logic), and can handle inherently imprecise, vague, and inexact concepts (Chang, 1996; Kahraman, 2008; Nasery & Kalkan, 2021; Patil, 2018; van Laarhoven & Pedrycz, 1983; Zadeh, 1965). There are numerous types of membership functions in fuzzy sets such as triangular, trapezoidal, Gaussian, etc. (Liu, Eckert, & Earl, 2020; Malczewski & Rinner, 2015). Triangular and trapezoidal are well researched. Triangular fuzzy numbers (TFN) are primarily used in literature and can be represented by order triplet (l, m, u) of real numbers, where l, m, u stands for low, medium, and upper values, respectively. The triangular fuzzy membership function is defined by Equation 7 and illustrated in Figure 3.2.

$$\mu\,(x) = \left\{ \begin{matrix} (x-l)/(m-l), & l \le x \le m \\ (u-x)/(u-m), & m \le x \le u \end{matrix} \right\} \tag{7.3}$$

Where $\mu\,(x)$ is the triangular fuzzy membership function, $x$ is the variable of the function, and $l$, $m, u$ are the low, medium, and upper possible values of the fuzzy-AHP scale.

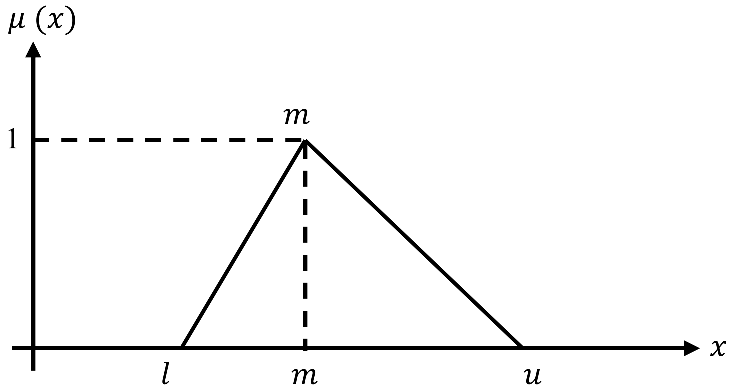

**Figure 3.2.** *The triangular fuzzy membership function*

The fuzzy-AHP method was initially introduced by van Laarhoven and Pedrycz (1983) and Chang (1996) to decrease the human judgment's uncertainty and vagueness and perform robust analysis by employing a range of value instead of a crisp value by distributing the problem into a hierarchical structure (Kahraman, 2008; Nasery & Kalkan, 2021). Implementation of fuzzy-AHP method consist of 6 steps (Ahmad & Shahzad Siddiqui, 2017; Liu, Eckert, & Earl, 2020; Nasery & Kalkan, 2021; Sobandi Dwi Putra et al., 2018):

1- Structuring the problem, this step decomposes the problem into a hierarchy which includes goal, criteria, and alternatives.

2- Constructing fuzzy-pairwise comparison matrix, in this step crisp values are replacing with fuzzy sets numbers (Equation 8) in the judgment matrix (Equation 9).

$$A_{ij} = (l, m, u) = (l, a_{ij}, u) \tag{8.3}$$

$$A = \begin{bmatrix} A_{1j} & \dots & A_{1j} & \dots & A_{1n} \\ \vdots & \dots & \vdots & \dots & \vdots \\ A_{ij} & \dots & A_{ij} & \dots & A_{in} \\ \vdots & \dots & \vdots & \dots & \vdots \\ A_{n1} & \dots & A_{nj} & \dots & A_{nn} \end{bmatrix} \tag{9.3}$$

Where $A_{ij}$ is the crisp value defined by expert, $l, m, u$ are the TFNs, and $a_{ij}$ is the importance of the $i^{\text{th}}$ criterion over the $j^{\text{th}}$ criterion.

3- Synthesizing the judgments, in this step the judgements of multiple experts are aggregating using the geometric mean aggregation technique (Equation 10).

$$B_{ij} = (l_{ij}, m_{ij}, u_{ij}) = \left( \left( \prod_{j=1}^{n} l_{ij}\ (t) \right)^{\frac{1}{n}}, \left( \prod_{j=1}^{n} m_{ij}\ (t) \right)^{\frac{1}{n}}, \left( \prod_{j=1}^{n} u_{ij}(t) \right)^{\frac{1}{n}} \right) \tag{10.3}$$

Where $B_{ij}$ is the aggregated judgments of multiple experts, $l, m, u$ are the TFNs, $t$ is the number of experts, and $n$ is the number of criteria.

4- Calculation of the Fuzzy weights of the criteria, in this step the fuzzy weights are calculated, several fuzzy sets are aggregated into a single fuzzy set by employing the geometric mean aggregation method (Equation 11) (Equation 12).

$$ri = \left(\prod_{j=1}^{n} B_{ij}\right)^{\frac{1}{n}} = \left(\left(\prod_{j=1}^{n} l_{ij}\right)^{\frac{1}{n}}, \left(\prod_{j=1}^{n} m_{ij}\right)^{\frac{1}{n}}, \left(\prod_{j=1}^{n} u_{ij}\right)^{\frac{1}{n}}\right) \tag{11.3}$$

$$wi = ri * (r1 + r2 + \cdots + rn)^{-1} = (lw_i, mw_i, uw_i) \tag{12.3}$$

Where $r_i$ is the geometric mean of the TFNs, $w_i$ is the weight of the $i^{\text{th}}$ criterion, and $lw_i, mw_i, uw_i$ are the weights of the TFNs.

5- Defuzzification of the fuzzy weights, this step involves the transformation operation of fuzzy weights (sets) to crisp or normal weights (values) (Equation 13), in this step normalization process is also performed to derive the final weights (Equation 14); and (6) Consistency Checking.

$$Mi = \frac{lwi + mwi + uwi}{3} \tag{13.3}$$

$$Ni = \frac{Mi}{\sum_{i=1}^{n} Mi} \tag{14.3}$$

Where $M_{ij}$ is the de-fuzzified weight of the $i^{\text{th}}$ criterion, and $N_i$ is the normalized de-fuzzified weight of the $i^{\text{th}}$ criterion.

## 4. MATERIALS

In this study, nine different data layers have been used that are obtained from various governmental, non-governmental, and international organizations, as well as open-source GIS and RS data providers. The data used in this thesis are listed in Table 4.1 with the necessary data descriptions and information about the sources/providers of the data accordingly.

**Table 4.1.** *Data sources and descriptions of the data used in this study*

| Data layer | Type | Resolution/Scale | Source/Provider |
|---|---|---|---|
| DEM | Raster | 30 m | United States Geological Survey (USGS) Earth Explorer portal |
| LULC | Vector | 1:50000 | Food and Agriculture Organization of the United Nations (FAO) |
| Soil types | Vector | 1:50000 | United States Geological Survey (USGS) |
| River | Vector | 1:50000 | Derived from DEM and LULC map |
| Roads | Vector | 1:25000 | Open street map data. |
| Urban area/Towns | Vector | 1:50000 | Derived from LULC map and Open Street map data |
| Sentinel 2 MSI | Raster | 30 m | United States Geological Survey (USGS) Earth Explorer portal |
| Precipitation | Raster | 5 km | GEE API, IDAHO TerraClimate dataset |
| LST | Raster | 1 km | GEE API, MOD11A2 V6 product |

The Shuttle Radar Topography Mission (SRTM) DEM was downloaded from the United States Geological Survey (USGS) Earth Explorer portal. The DEM was used for calculating slope angle, slope aspect, curvature, TRI, TWI, and WEI. These data layers are then used in generating the HSR cost surface layer and landslide, snow avalanche, and flood susceptibility maps/layers.

LULC data layer was obtained from the Food and Agriculture Organization of the United Nations (FAO). According to the metadata of this layer, the temporal resolution of the data is 2016. Although this layer was created five years ago, the accuracy and broad coverage of the data make it an excellent source to use. It is worth mentioning that the features and locations that are subjected to change during five years are detected and updated by integrating the open street map data with this layer. This layer is used in producing river and towns layers, as well as in HSR route selection analysis, landslide susceptibility, snow avalanche risk, and flood risk maps/layers.

The soil types data was acquired from the USGS website. This layer contains different types of soil classes which have been simplified according to the requirements of the current study.

The rivers data layer was delineated from the DEM layer using the hydrology toolbox in ArcGIS pro software and is combined with extracted streams from the LULC map. The LULC map provides stream and riverbeds with exquisite precision and density, making it very reliable data to determine an appropriate distance from the streams and riverbeds.

National highways and major local roads data were obtained from open street map data. Some errors and deficiencies of the data were resolved, and manual corrections were applied accordingly. This data layer was used in the HSR route selection process, landslide susceptibility, and avalanche susceptibility.

Urban areas and towns data layers were extracted from the LULC map and were integrated with the open street map data. Furthermore, the road buffers were also combined with this layer to better represent urban areas and structures. This layer was used in HSR route selection analysis.

The Sentinel 2 multi spectral images were derived and processed in the GEE API and the results were downloaded. Sentinel 2 data were used for calculating the NDVI. The NDVI layer is used in avalanche susceptibility assessment. The employed scrips for calculating the NDVI index are shown in Appendix B.

Precipitation data were processed in the GEE portal and the results were downloaded. The precipitation data was considered in two different intervals of five years; the first interval is from 2000 to 2005 from December to May of each year, the second interval starts from 2016 to 2021 from December to May of each year. These datasets were subjected to arithmetic mean operation for deriving the average precipitation of the study area. The utilized scrips for calculating the average rainfall are presented in Appendix B.

The LST data layer was derived from the Moderate Resolution Imaging Spectroradiometer (MODIS) satellite product in the GEE API environment. The average LST was calculated for six years interval, over three mounts (January to March) starting from 2016 to 2020. This data layer was used in snow avalanche susceptibility mapping. The employed scrips for calculating the average LST are displayed in Appendix B.

## 4.1. Generating Data Layers of the Most Significant Factors for the HSR Route Location Selection

This section explains the data layers production process of the most significant factors (criteria) for generating the optimal HSR route in the context of the current study and the significances of these factors are also comprehensively demonstrated. In addition, the data layers for the factors considered in landslide, snow avalanche, and flood susceptibility analyses are also generated and their significances are explained in their related sections. The most prominent factors affecting the HSR alignment location are selected based on the geographic location of the study area, considering the literature, and experts' opinions. In this study, slope, LULC, geology (soil types), distance from rivers, proximity to roads, proximity to towns/cites, distance from historical sites and protected areas, distance from faultlines, landslide risk, snow avalanche risk, and flood risk are considered as the most prominent factors for selecting the optimal HSR route. This study only covers those natural disasters that are highly expected to happen in the study area (floods, earthquakes, avalanches, and landslides). The data layers for the HSR route location selection and landslide, snow avalanche, and flood susceptibility are generated using ArcGIS Pro, QGIS, and System for Automated Geoscientific Analyses GIS (SAGA-GIS) software and GEE API. These layers are classified into different numbers of classes due to the nature of the data layer. For example, in landslide susceptibility same layers such as lithology and LULC have more classes than other layer and each class have different influence on the landslide susceptibility; hence, each class should be rated separately. Keeping this in mind, a scale of 1 to 100, assumed as percentage of influence, is considered in this study and used to rate the classified data layers of the HSR route location selection and landslide, snow avalanche, and flood susceptibility.

From the HSR route location selection perspective, the data layers are classified into different classes based on their suitability for the HSR route placement in the area.

The data classes for the HSR route are rated/reclassified using a scale of 1 to 100. The LCP tool considers the lowest/cheapest value in a cost raster to generate a route; thus, the most suitable classes for HSR route location are assigned the lowest values while the very low suitable classes are given the highest value.

In the case of the landslide, snow avalanche, and flood susceptibility analysis, the data layers are classified into different classes using a scale of 1 to 100 where the very highly susceptible areas are allocated the highest rating, while very low suitable areas are given the lowest rating.

#### 4.1.1. Slope (Gradient)

The slope factor has a fundamental role in HSR route location and direction. HSR route alignment has specific requirements for slope/gradient, which should be strictly followed during the routing process. The maximum gradient of the HSR line is a major technical standard that can significantly reduce the engineering and construction cost of the project by utilizing the largest possible maximum gradient (Yi, 2018a).

The vertical design of the HSR alignment considers the maximum gradient as the maximum design gradient which strongly affects the capacity, quality, and direction of the HSR line and is a major technical standard for railways (Yi, 2018a). Furthermore, the steepest possible maximum gradient reduces the engineering and construction costs of an HSR route. (Yi, 2018a). The maximum gradient for an electric traction HSR can be calculated using the following formula (Yi, 2018a):

$$i_{max} = \frac{3600P_k - w_0 . g . V_{max}}{g . V_{max}} (\text{‰}_0) \tag{1.4}$$

where $p_k$ is the power required per ton of train quality (*kW/t*); $V_{max}$ is the maximum speed of train operation (*km/h*); $w_0$ is the basic resistance of the train operation unit in calculating speed (*N/kN*), and *g* is the gravity of the earth.

Considering the above formula and taking into account the optimum power and speed limit condition, the maximum gradients for HSR at different standard designed speeds are calculated and the recommended gradients are shown in Table 4.2. The calculated gradients for the general lot are utilized first, followed by the gradients for special locations in areas with a greater gradient than the general lot.

**Table 4.2.** *Recommended maximum gradients for HSR line (Yi, 2018a)*

| Design Speed (km/h) | | 350 | 300 | 250 |
|---|---|---|---|---|
| $i_{max}$(%) | General lot | 1.2 | 1.5 | 1.8 |
| | Special location | 2.0 | 2.5 | 2.8 |

In plain areas, the maximum gradient has little effect on earth works, but in hilly areas, it strongly controls earth works and reduces the length of the tunnels and bridges (Yi, 2018a).

The maximum gradient of some of the HSR lines around the world are as follow: The French HSR line use 2.5-3.5%, Japan's Shinkansen lines less than 2.5%, Kyushu Shinkansen line in Japan is ready to use a grade of 3.8%, Tokaido Shinkansen line has 1.5%, the German HSR uses 2.0% but in full speed mode it is 4.0%, Beijing-Shanghai line generally has 1.2% and less than 2.0% in some areas, Beijing–Tianjin uses 2.0% grade, Shijiazhuang–Taiyuan has 1.35% upward gradient limit and 1.8% downward, Shenyang–Harbin has mostly 1.2% and to 2.0%, Beijing–Zhengzhou uses a grade of 1.2% to 2.0%, and Wuhan–Guangzhou has 1.2%, 1.5%, 2.0%, and 2.5% (Yi, 2018a). China have adopted a maximum gradient system of 0.9%, 1.2%, 1.5%, and 2.0% for its HSR network (Japan International Cooperation Agency & Ministry of Railways Republic of India, 2015; Yi, 2018a).

Generally, a maximum gradient of 1.2% is considered more reasonable but up to 4.0% is allowed related to topographical and geographical conditions on an area (Japan International Cooperation Agency & Ministry of Railways Republic of India, 2015; UIC-International union of railways, 2018; United Nations Economic Commission for Europe, 2017; Yi, 2018a).

Taking into consideration the geographical location of the study area and technical documents, a maximum gradient of 4.0% is proposed as the maximum design gradient for the HSR route. Furthermore, according to formula 2.1, the maximum recommended gradient for electric traction HSR train at a 250 km/h speed is calculated 1.8% for the general lot and 2.8% for special locations. Considering the above-stated indications, the slope later of the study area is classified into five classes (Table 4.3). The classified slope map is generated by considering these four classes and is shown in Figure 4.1.

**Table 4.3.** *The influential factors on the optimal HSR alignment location, their sub-categories, and assigned ratings*

| Factor/Criterion | Classes (sub-categories) | Ratings (%) |
|---|---|---|
| **Slope** | 0 - 1.2 % | 1 |
| | 1.2 - 2.8 % | 5 |
| | 2.8 - 4.0 % | 15 |
| | 4.0 - 10.0 % | 90 |
| | >10.0 % | 100 |
| **LULC** | Barren Lands | 1 |
| | Rangelands | 1 |
| | Irrigated Agricultural Lands | 60 |
| | Rainfed Agricultural Lands | 50 |
| | Fruit Trees | 70 |
| | Vineyards | 70 |
| | Forests and Shrubs | 70 |
| | Sand Cover | 95 |
| | Water Bodies and Marshlands | 100 |
| | Permanent Snow Cover | 100 |
| | Build Up Areas | 100 |
| **Soil Types** | Silty Clay | 60 |
| | Sandy Clay | 15 |
| | Clayey Gravel | 5 |
| | Sand | 95 |
| | Silty Gravel | 1 |
| | Rocks | 50 |
| | Water Bodies | 100 |
| **Distance from Rivers** | <200 m | 100 |
| | 200-500 m | 80 |
| | 500-1000 m | 30 |
| | 1000-1500 m | 15 |
| | 1500-2000 m | 10 |
| | >2000 m | 1 |
| **Proximity to Roads** | <200 m | 100 |
| | 200-1000 m | 1 |
| | 1000-2000 m | 10 |
| | 2000-3000 m | 20 |
| | 3000-4000 m | 30 |
| | >4000 m | 40 |

**Table 4.3.** *(continue) The influential factors on the optimal HSR alignment location, their sub-categories, and assigned ratings*

| | | |
|---|---|---|
| **Proximity to Towns/Cities** | <1000 m | 1 |
| | 1000-2000 m | 10 |
| | 2000-3000m | 50 |
| | 3000-4000m | 80 |
| | >4000 m | 90 |
| **Landslide Risk** | Very Low | 1 |
| | Low | 20 |
| | Moderate | 50 |
| | High | 80 |
| | Very High | 100 |
| **Snow Avalanche Risk** | Very Low | 1 |
| | Low | 20 |
| | Moderate | 50 |
| | High | 80 |
| | Very High | 100 |
| **Flood Risk** | Very Low | 1 |
| | Low | 20 |
| | Moderate | 50 |
| | High | 80 |
| | Very High | 100 |
| **Distance from faultlines** | 0-500 m | 95 |
| | 500-750 m | 80 |
| | 750-1000 m | 50 |
| | 1000-1250 m | 30 |
| | 1250-1500 m | 10 |
| | >1500 m | 1 |

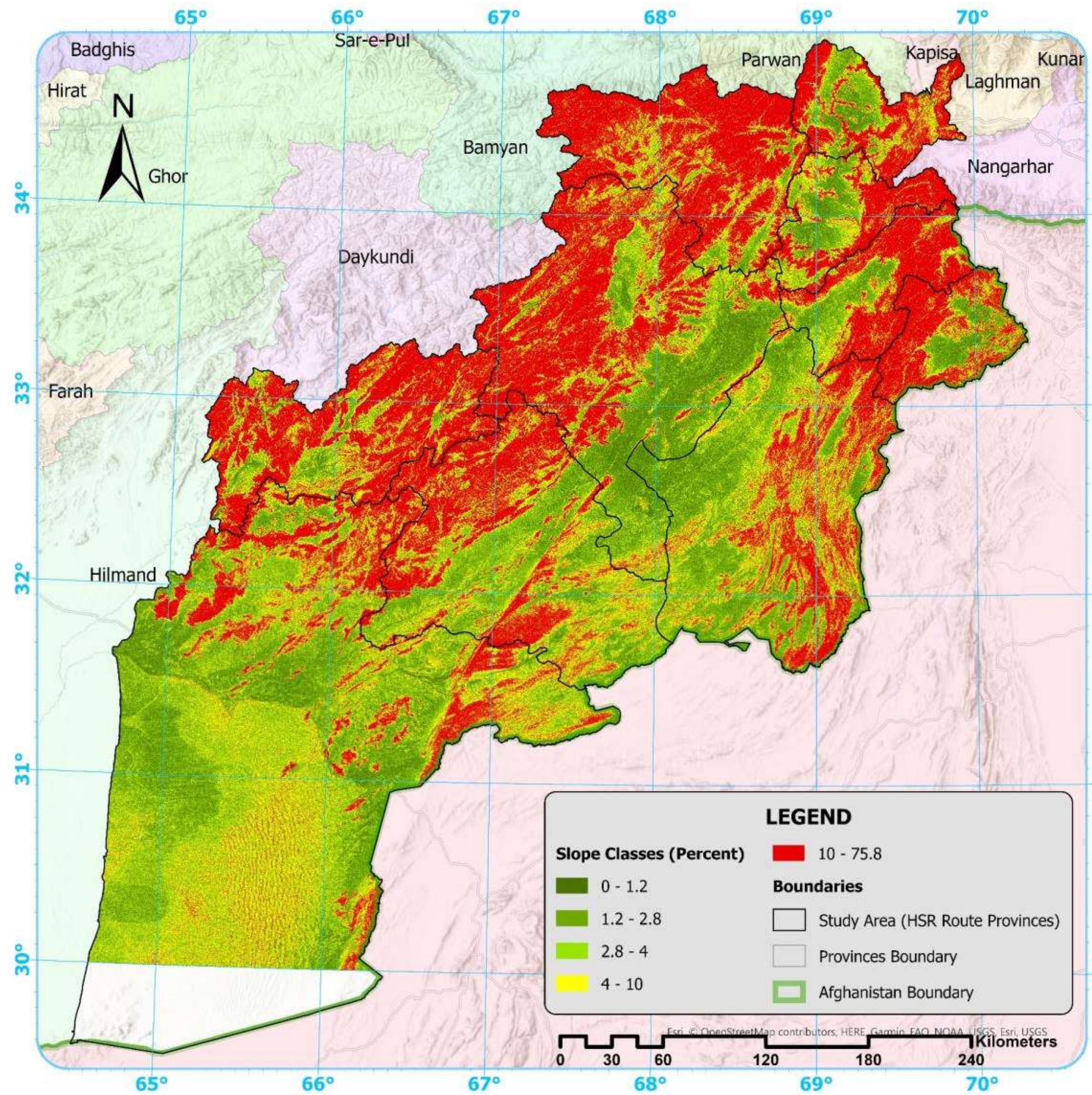


**Figure 4.1.** *The classified slope map, considered in the HSR route location assessment*

### 4.1.2. Landuse/landcover

LULC is one of the important factors which heavily affects the overall project and construction costs and is also vital from the environmental perspective. Therefore, the LULC map of a region should be prepared appropriately, and each class of the land should be evaluated in accordance with economic and environmental criteria. The route should avoid productive agricultural lands, urban areas, rural habitations, water bodies, forests, riverbeds, sandbanks, protected areas, and other constraints such as national parks, archeological, and areas designated to cemeteries and tombs (Singh, Singh, & Singh, 2019). The route will be more optimal if it passes through areas with poorly vegetated and barren lands that are more viable compared to agricultural lands. The land aquation costs are very high in urban areas and agricultural lands, while the industrial areas are less expensive (Singh, Singh, & Singh, 2019; Wahdana et al., 2019). The land acquisition costs show a major difference from country to country. Generally, it can change from 5% to 10% (Henn, Sloan, & Douglas, 2013); for example, the land acquisition cost of the United Kingdom HS2 line is estimated about 15% of the project costs, while it is 10% in the case of Egypt (Belal, Khalil, & El-Dash, 2020). The LULC data layer is obtained from the FAO that contains detailed LULC classes (Figure 4.2).

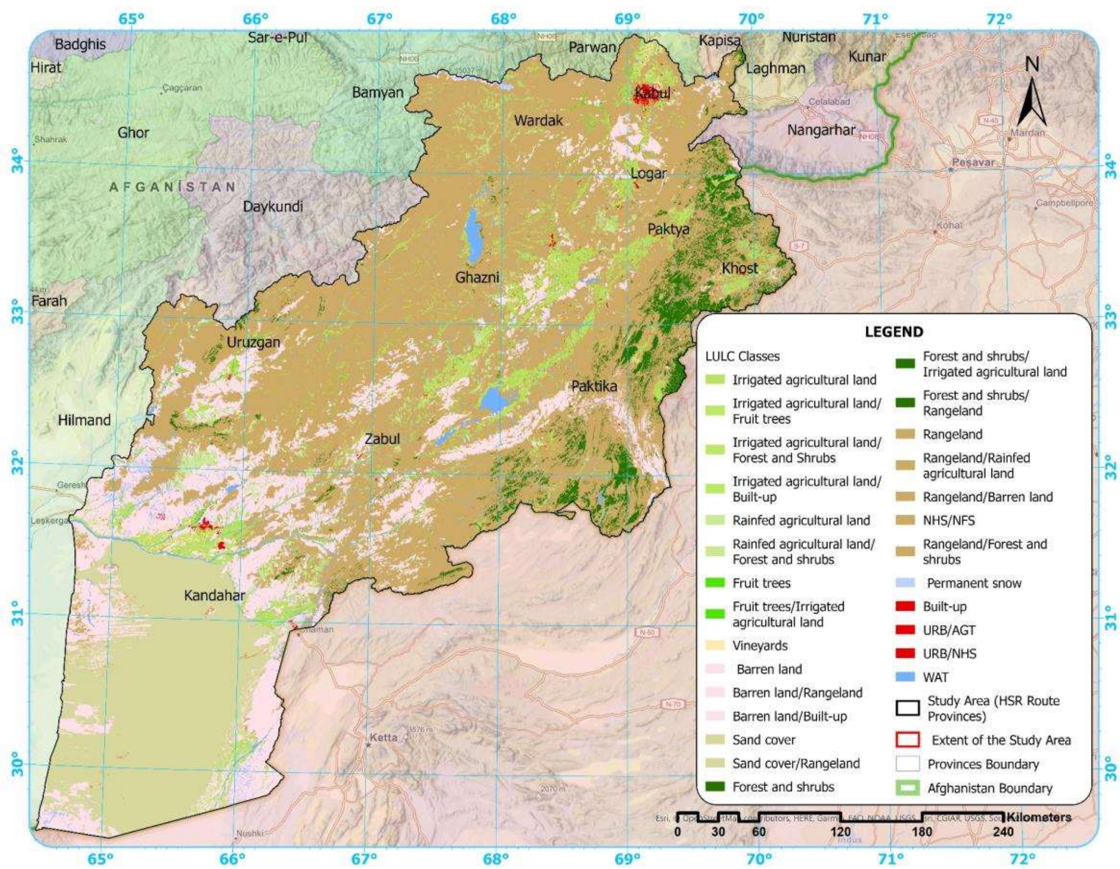


**Figure 4.2.** *The LULC map of the study area, obtained from FAO*

This layer is subjected to a simplification process to better rank and reclassify it for further processing steps. In addition, this layer was updated with the most recent urban developments and land cover changes. The simplified and updated LULC map is shown in Figure 4.3. The simplified and updated LULC map classes are ranked (Table 4.3).

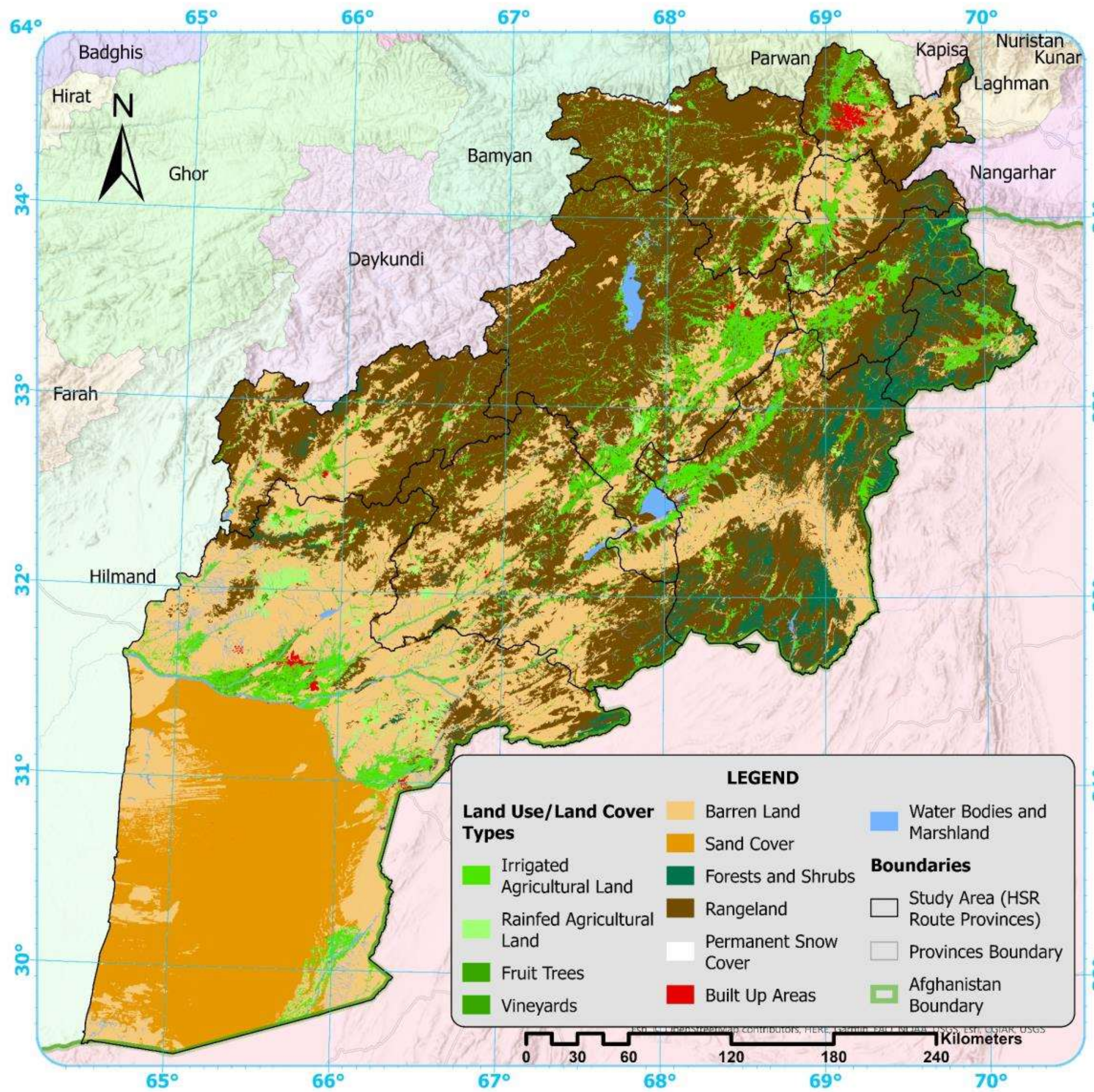


**Figure 4.3.** *The simplified and updated LULC map of the study area*

### 4.1.3. Soil types

Soil is the primary material for foundations and embankments and has great importance in transportation engineering. In soil classification for the HSR track bed, it is very imperative to identify areas where the groundwater level is high, as it can increase construction costs, future maintenance costs of the route, and decrease the route efficiency. From the environmental perspective, erosion-sensitive soils are severely affected by track construction operations and should be avoided. The soil can be classified based on two major categories; textural classification and particle-size distribution and plasticity (Das, Emeritus, & Sobhan, 2012). The soil classification based on particle-size distribution and plasticity is commonly used for engineering purposes (Das, Emeritus, & Sobhan, 2012). There are two widely used classification systems in this regard: The American Association of State Highway and Transportation Officials (AASHTO) classification system and the Unified Soil Classification System (Das, Emeritus, & Sobhan, 2012).

The study area has different types of soil in distinct locations. The agricultural productive soils are not considered suitable in most of the areas, but in some areas the HSR route can pass through agricultural areas with suitable soil for HSR route. The soil types data layer has a comprehensive classification of soil (Figure 4.4). Therefore, a simplification process is also performed on this layer to decrease the number of soil classes considering the technical requirements of the HSR alignment (Figure 4.5). The simplified soil map classes are then ranked (Table 4.3).

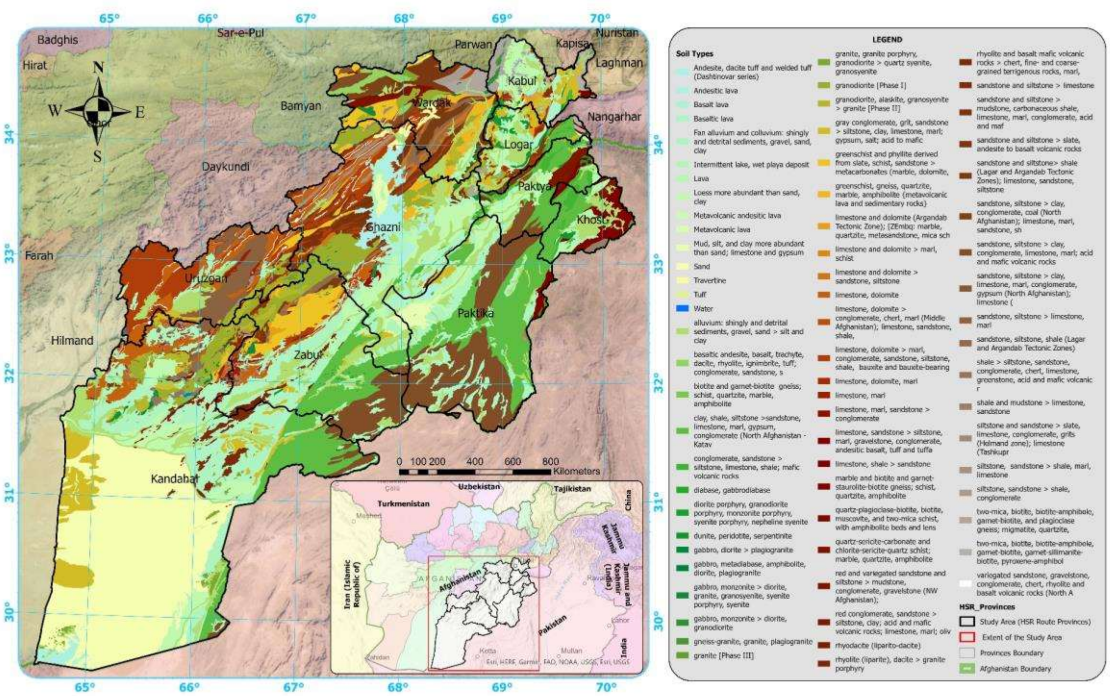


**Figure 4.4.** *The soil map of the study area acquired from USGS*

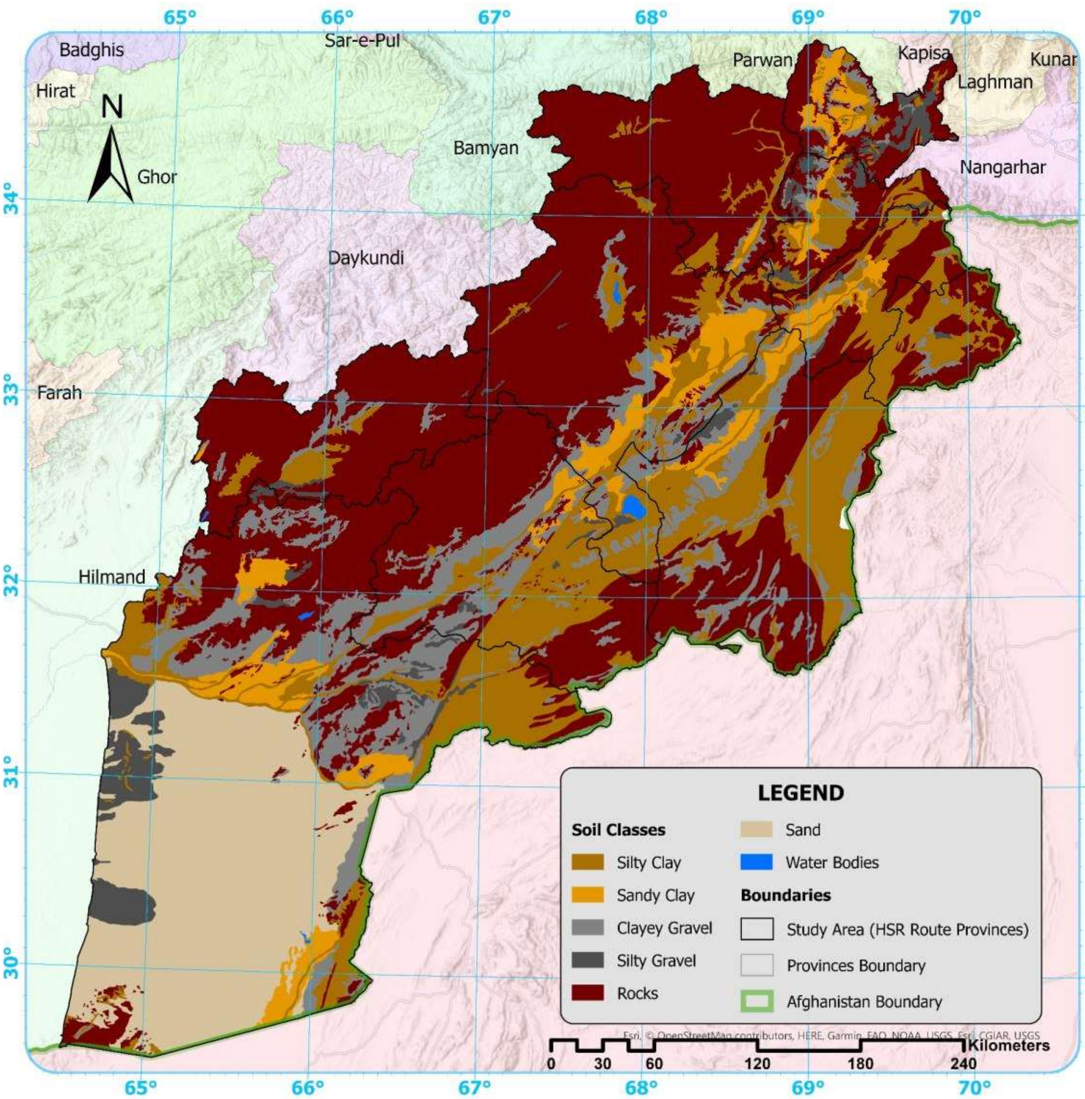


**Figure 4.5.** *The simplified soil map of the study area*

### 4.1.4. Distance from rivers

Distance from rivers and streams is essential for reducing the flood and erosion risk of the route embankment, and minimizing intersection with the route; consequently, minimizing the construction costs by decreasing the number of bridges and other protective infrastructures. The infrastructure building costs are typically between 10 to 25% of the total project cost and having more intersections with rivers and streams can easily double the costs (Henn, Sloan, & Douglas, 2013). The rivers layer consists of the generated streams from the DEM layer combined with the extracted streams from the LULC map (Figure 4.6).

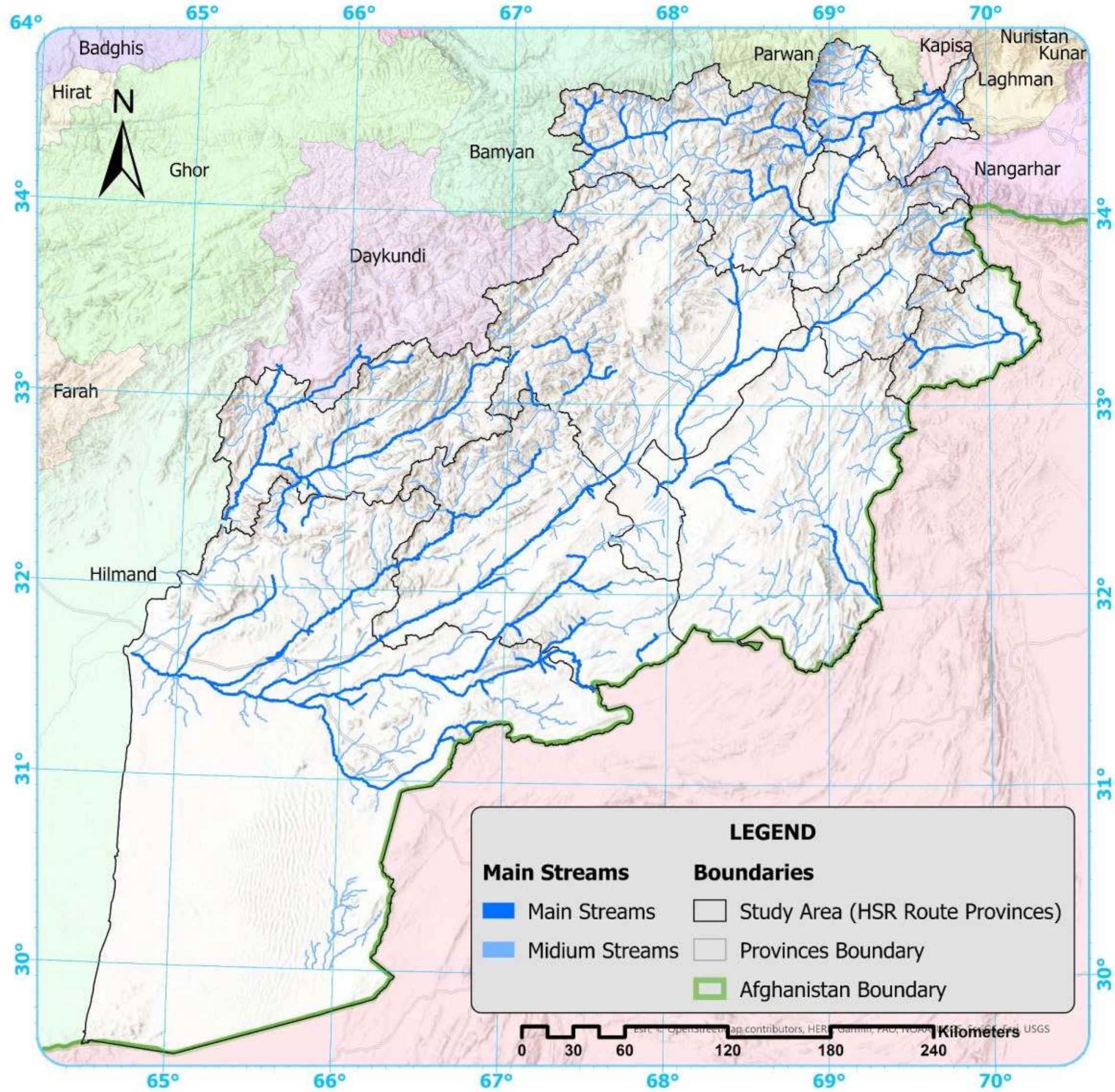


**Figure 4.6.** *The rivers map of the study area*

Based on the setbacks used in the literature, a minimum 200 m setback from streams and riverbeds is considered satisfactory. As a result, the layer is classified into the following three classes: streams and riverbeds as restricted areas, areas at <200 m distance from streams and riverbeds as restricted, areas at 200-500 m as very low suitable, 500-1000 m low suitable, 1000-1500 m moderately suitable, 1500-2000 m highly suitable, and >2000 m distance as very highly suitable. These classes are ranked (Table 4.3), and a reclassified map is produced considering these rankings (Figure 4.7).

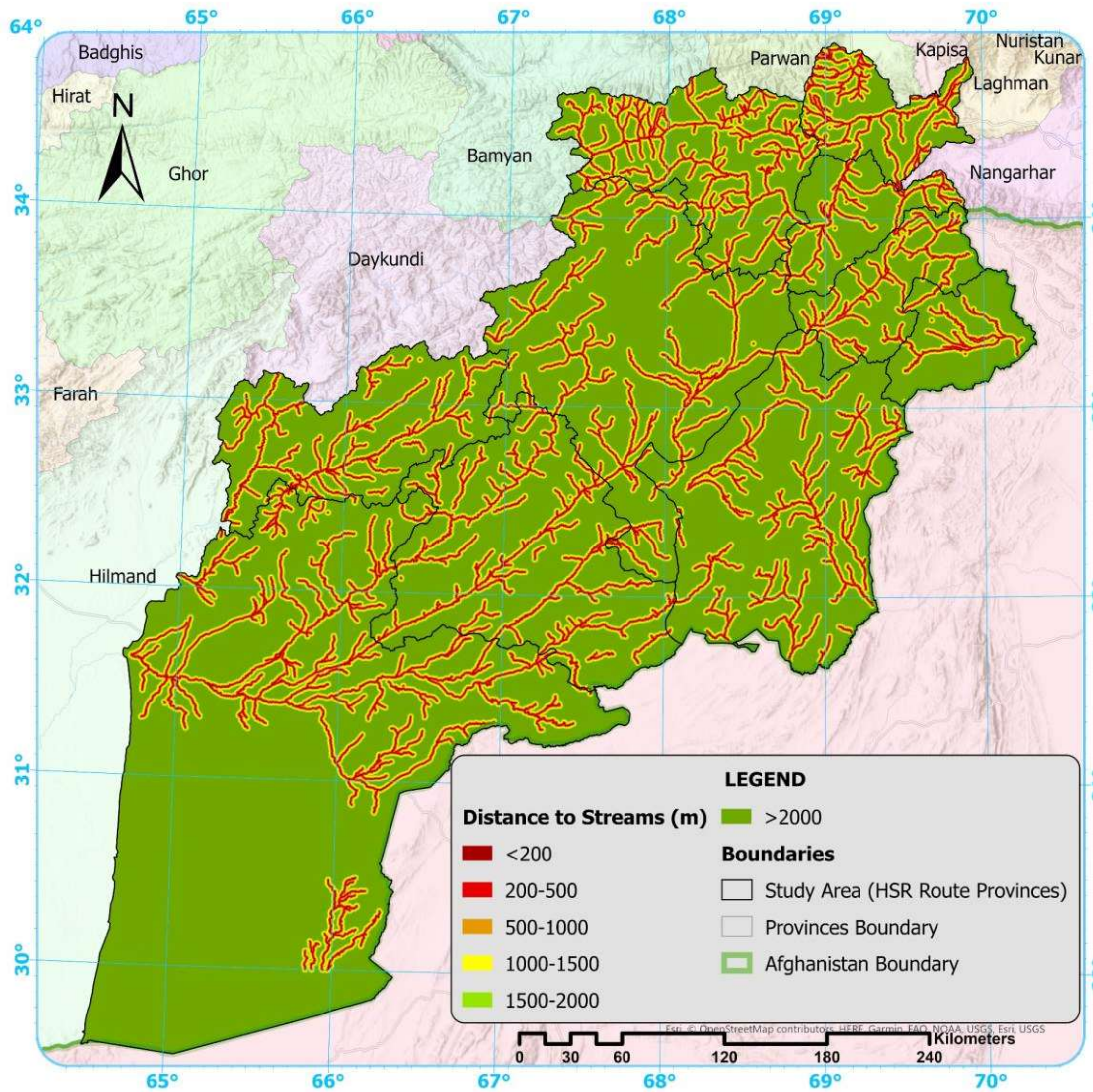


**Figure 4.7.** *The classified buffer distances from rivers, considered in the HSR route location assessment*

### 4.1.5. Proximity to roads

To minimize the chance of intersection with roads, it is very important to create restriction buffer zones around the roads, reducing the construction cost significantly. On the other hand, the maintenance and routine patrol will be easy for the HSR line near roads. The roads layer is presented in Figure 4.8.

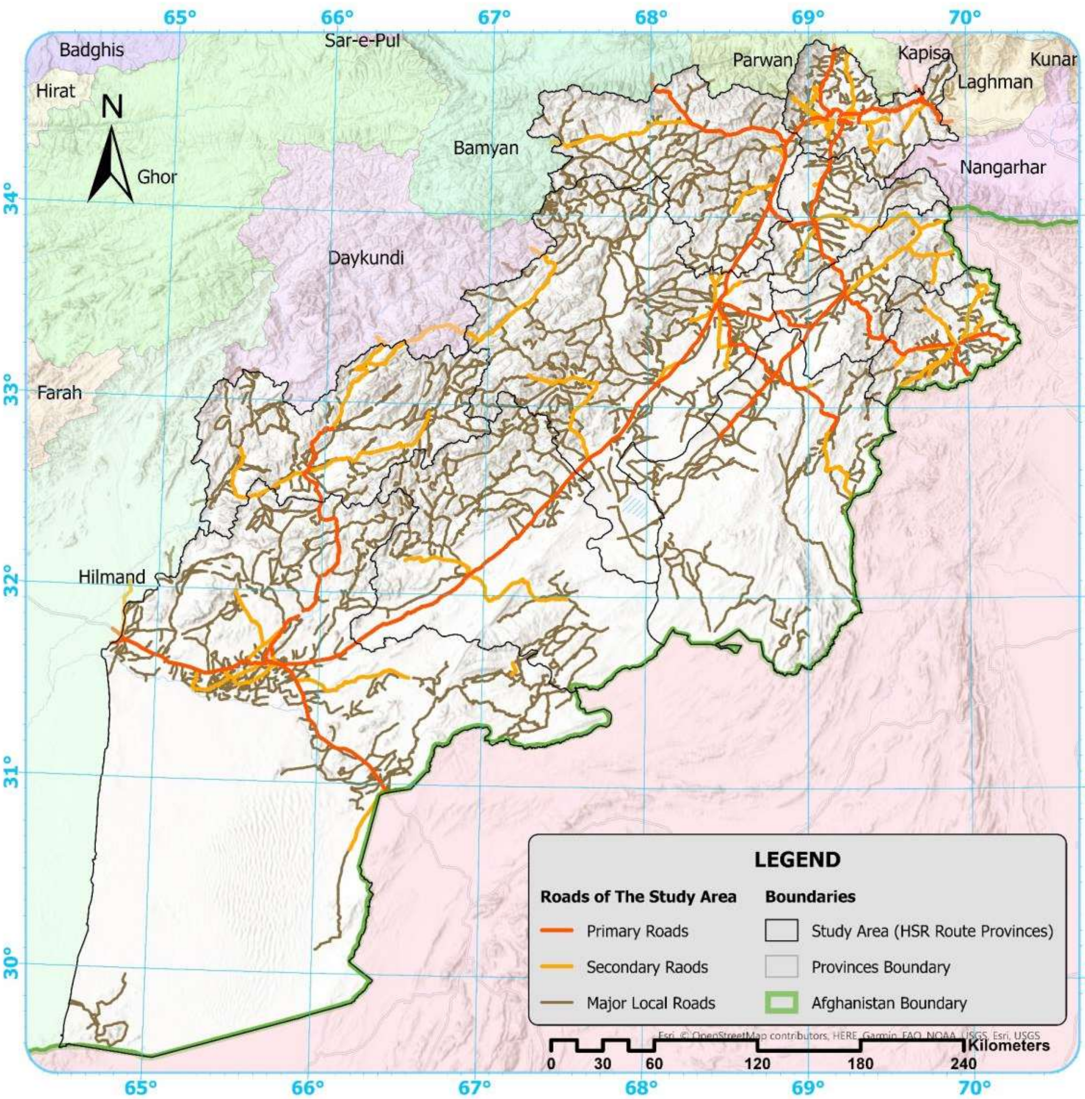


**Figure 4.8.** *The roads map of the study area*

Considering the literature, a 200 m restricted buffer zone is created around the roads to limit intersections with roads. After 200 m, the HSR route is considered more optimal in locations near the roads. Therefore, four buffer zone were created around the roads and are ranked accordingly. The map was reclassified and is shown in Figure 4.9.

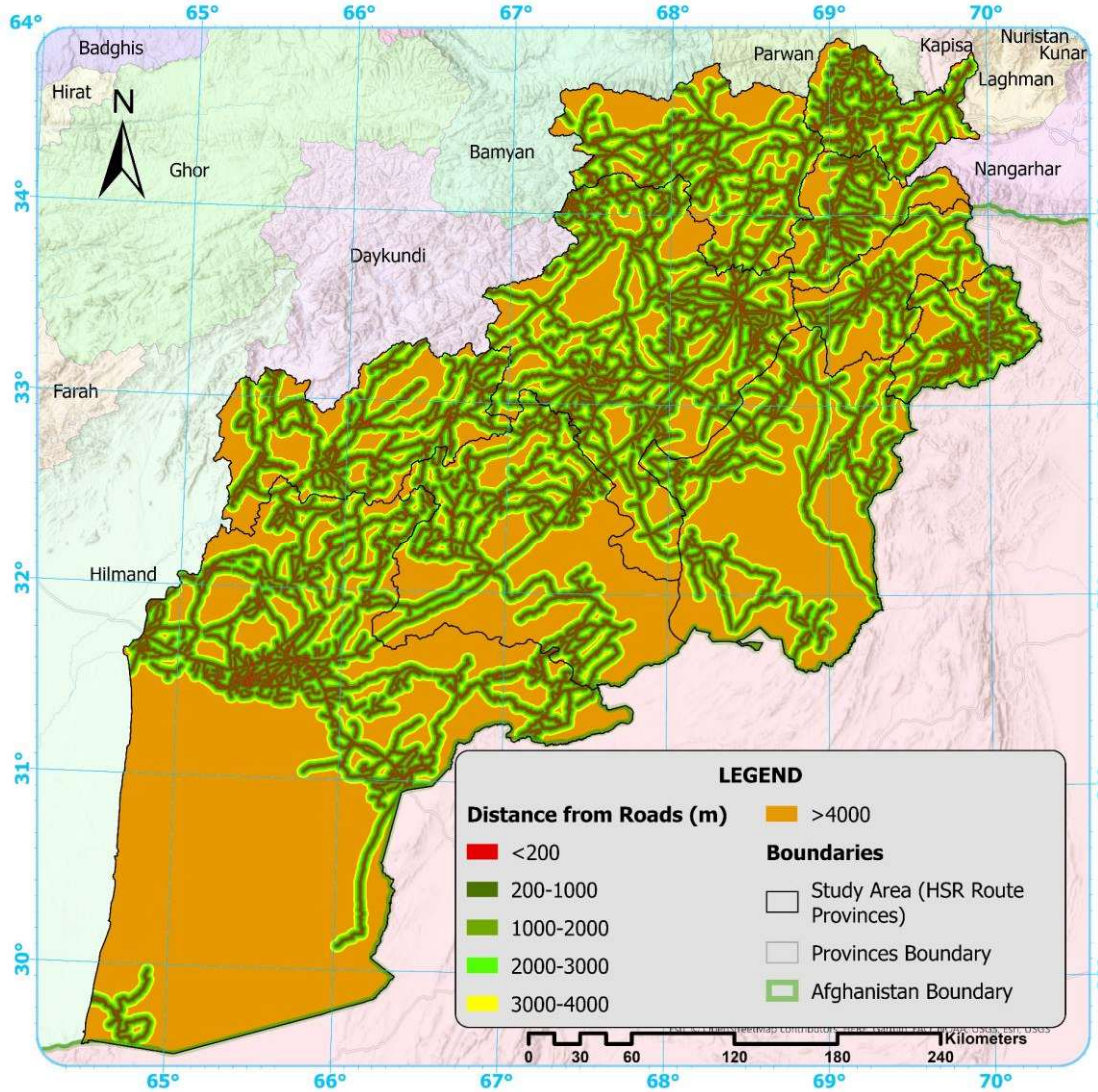


**Figure 4.9.** *The classified buffer distances from the roads, considered in the HSR route location assessment*

### 4.1.6. Proximity to towns/cities

One of the most important factors in the development of population centers is their access to transportation networks. Therefore, transportation systems should be as close as possible to population centers. The primary purpose of the HSR line is to serve the largest number of people and connect multiple cities and regions along the route, which results in creating an economic corridor and improving regional economic development (Saat and Serrano 2015; Li et al. 2020a). Thus, the towns and cities between the start and end points of the route should have accessibility to the HSR services. Hence, proximity to towns and cities is very important for attracting passengers and ensuring the efficiency of the HSR line. The towns and cities are extracted from the LULC map and integrated with open street map data for updating purposes (Figure 4.10). This layer contains centers of 10 cities located along the HSR route. The goal is to have the maximum number of cities connected by the HSR line which is one of the study's objectives.

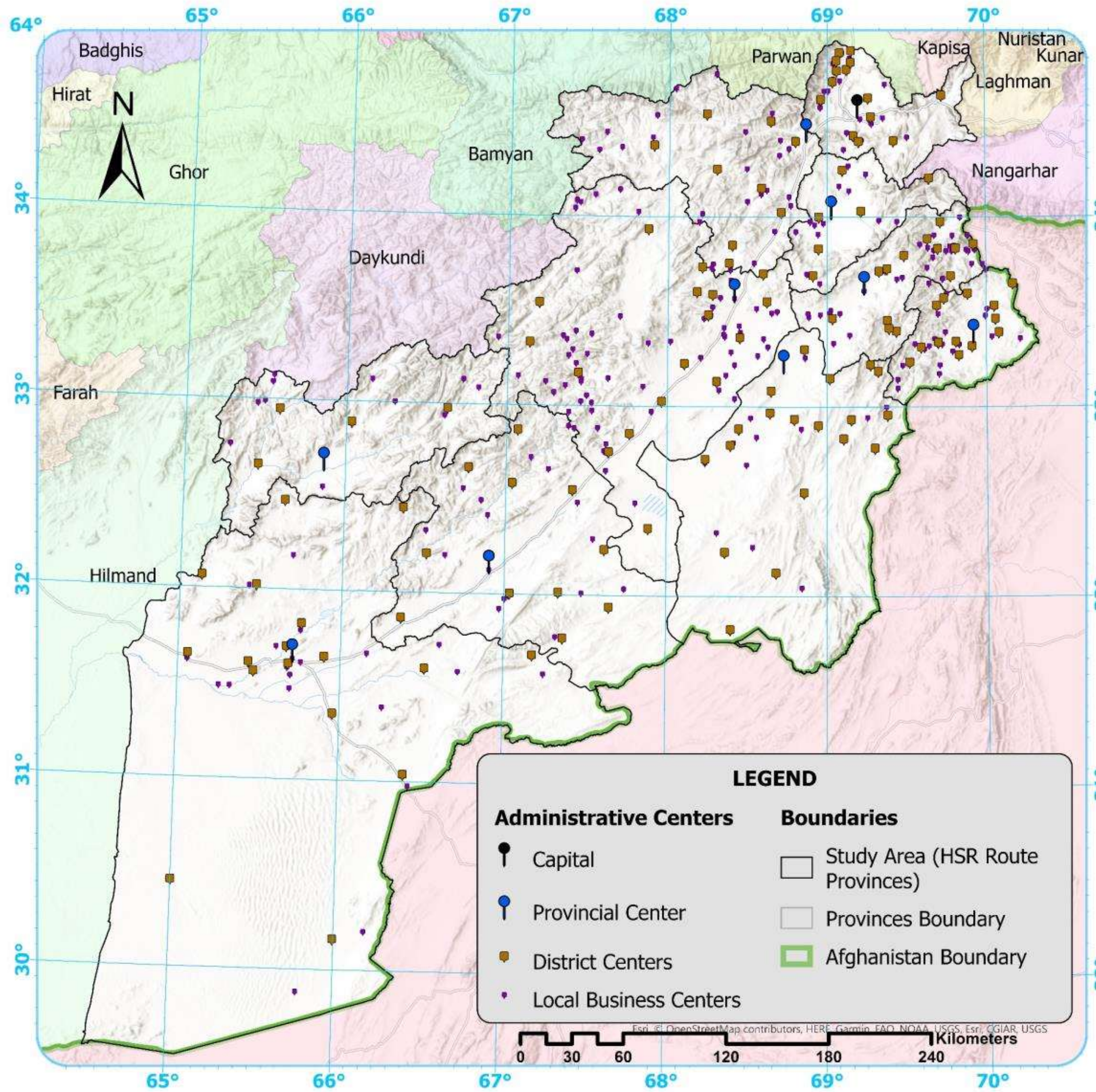


**Figure 4.10.** *The towns and cities centers map of the study area*

Following the literature, the following five buffer zones are created around the towns and cities: ≤1 km as very highly suitable, 1-2 km highly suitable, 2-3 km moderately suitable, 3-4 km low suitable, and more than 4 km very low suitable (Table 4.3). These buffer zones are ranked, and the final map was generated considering these rankings (Figure 4.11).

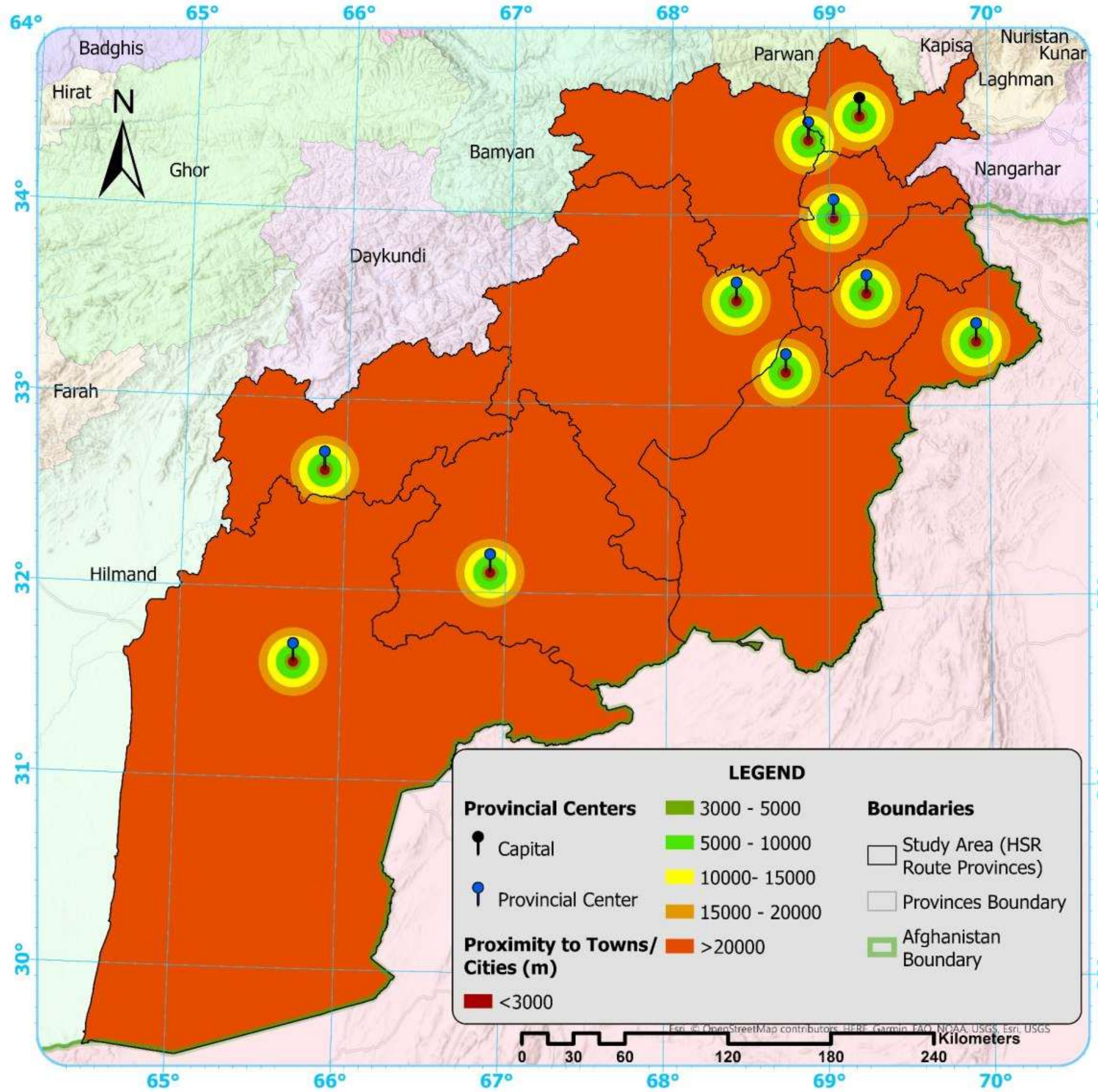


**Figure 4.11.** *The classified buffer distances from towns and cities, considered in the HSR route location assessment*

### 4.1.7. Landslide susceptibility

The risk of landslides is one of the natural problems that always lurks in roads and residential areas, especially in rainy regions. Landslides can destroy HSR infrastructures, block the route, decrease incomes, create unexpected service delay, case fatalities, and loss of money. Hence, the final route should be as far from the areas susceptible to landslides as possible. Landslide is the down-slope movement of a mass of rocks, debris, and soil due to the direct effect of gravitational force. Generally, landslides can be categorized into five classes based on their movement pattern: flows, falls, slides, spreads, and topples.

The landslide susceptibility can be assessed by quantitative and qualitative methods (Yan et al., 2019). Quantitative methods such as frequency ratio, the weight of evidence (WoE), logistic regression (LR), GA, and neural networks require detailed landslide inventory data for hazard prediction or validation assessment (Ali et al., 2021; Goumrasa, Guendouz, & Guettouche, 2021; Yan et al., 2019). The qualitative method relies on the expert's knowledge about the phenomenon, characteristics of the study area, and the geomorphic analysis related to the slope instabilities for generating the hazard map (Ali et al., 2021; Goumrasa, Guendouz, & Guettouche, 2021; Yan et al., 2019). The qualitative method is widely used in literature for landslide susceptibility assessment.

Goumrasa, Guendouz, and Guettouche (2021) have used the integration of GIS, AHP, and weighted linear combination (WLC) method for generating landslide susceptibility map. They have chosen lithology, slope, daily temperature amplitude, rainfall, lineament density, NDVI, relative relief, drainage density, and distance to streams factors to construct the landslide susceptibility model.

In a similar study conducted by Yan et al. (2019), the AHP, normalized frequency ratio, and cloud model methods are used to calculate the landslide susceptibility. They have considered lithology, NDVI, slope angle, slope aspect, distance to rivers, distance to faultlines, rainfall, seismic intensity, distance to construction, and distance to roads as landslide inducing factors.

Meena, Mishra, and Piralilou (2019) developed a hybrid spatial multi-criteria evaluation (SMCE) method for landslide susceptibility mapping considering slope, aspect, elevation, drainage, distance to roads, faultlines, and lithology factors. They have used AHP, frequency ratio, and SMCE methods for landslide susceptibility mapping and compared the results of each method for determining the accuracy of the methods. They concluded that the SMCE method is more robust followed by frequency ratio and AHP methods.

In another study conducted by Sur et al. (2021), GIS and fuzzy MCDA methods have been used for landslide susceptibility mapping. They have used slope, rainfall, lithology, NDVI, proximity to road, and LULC conditioning factors to determine the landslide susceptibility zones. The landslide inventory data have been used for testing and validating the model.

There is no standard principle for selecting the landslide conditioning factors due to the nature of landslide, geological and environmental settings of the study area, and data availability (Ali et al., 2021; Vakhshoori et al., 2019; Yan et al., 2019). Rainfall is considered the most significant impact factor for landslide susceptibility in several studies, followed by slope, lithology, aspect, distance to faults, distance to streams, LULC, faults, proximity to roads, and TWI (Hammad, 2020; Lila, 2018; Meena, Mishra, & Piralilou, 2019; Paryani et al., 2020; Richard, 2020; Smith, 2017; Sur et al., 2021; Yan et al., 2019). Based on the observations, frequent landslides are commonly occurring in areas with a steeper slope, higher rainfall, and low vegetation (Sur et al., 2021).

In this study, the landslide susceptibility map is generated by adopting a GIS-based MCDA method and considering the most important factor involved in the process of forming a landslide. This method was chosen because of the study area's lack of sufficient/detailed landslide inventory data. The fuzzy-AHP method is used for weighing the factors. The relative importance of the factors is specified using questionary forms submitted to hydrology and geology experts. The general workflow and data processing steps in this study are presented in Figure 4.12.

In reference to the above literature, the landslide susceptibility inducing factors are determined as follows: slope, aspect, lithology, rainfall precipitation, LULC, distance to faults, distance to roads, distance to streams, NDVI, and TWI. The sub-categories of each factor are determined and ranked based on the literature and are shown in Table 4.4.

**Table 4.4.** *The most significant factors in landslide susceptibility, their subcategories, and their ratings*

| Factor/Criterion | Classes (Categories) | Ratings (%) |
|---|---|---|
| **Slope** | 0° - 15° | 1 |
| | 15° - 20° | 20 |
| | 20° - 30° | 100 |
| | 30° - 40° | 90 |
| | 40° - 45° | 30 |
| | >45° | 1 |
| **Aspect** | Flat (-1°) | 1 |
| | North (337.5°-0°-22.5°) | 100 |
| | Northeast (22.5°-67.5°) | 90 |
| | East (67.5°-112.5°) | 20 |
| | Southeast (112.5°-157.5°) | 10 |
| | South (157.5°-202.5°) | 5 |

**Table 4.4.** *(continue) The most significant factors in landslide susceptibility, their subcategories, and their ratings*

| | | |
|---|---|---|
| | Southwest (202.5°-247.5°) | 10 |
| | West (247.5°- 292.5°) | 20 |
| | Northwest (292.5°-337.5°) | 80 |
| **Lithology** | Carbonatic Rocks | 100 |
| | Gneiss, Schist, Quartzite | 90 |
| | Granites | 40 |
| | Surficial Deposits | 1 |
| | Ultramafic Rocks | 20 |
| | Volcanic Rocks | 10 |
| | Water Bodies | 1 |
| **Precipitation** | Micro rain (0-12 mm) | 0 |
| | Light rain (12-30 mm) | 30 |
| | Moderate rain (30-80 mm) | 70 |
| | Heavy rain (80-100 mm) | 85 |
| | Very heavy rain (100-180 mm) | 95 |
| | Torrential rain (>180 mm) | 100 |
| **LULC** | Barren Lands | 85 |
| | Rangelands | 90 |
| | Irrigated Agricultural Lands | 30 |
| | Rainfed Agricultural Lands | 100 |
| | Fruit Trees | 10 |
| | Vineyards | 10 |
| | Forests and Shrubs | 60 |
| | Sand Cover | 0 |
| | Water Bodies and Marshlands | 0 |
| | Permanent Snow Cover | 0 |
| | Build Up Areas | 10 |
| **Distance to Faults** | 0-300 m | 100 |
| | 300-500 m | 90 |
| | 500-1000 m | 75 |
| | 1000-2000 m | 50 |
| | 2000-3000 m | 30 |
| | >3000 m | 10 |
| **Distance to Roads** | <200 m | 100 |
| | 200-400 m | 70 |
| | 400-600 m | 70 |
| | 600-800 m | 70 |

**Table 4.4.** *(continue) The most significant factors in landslide susceptibility, their subcategories, and their ratings*

| | | |
|---|---|---|
| | 800-1000 m | 70 |
| | >1000 m | 5 |
| **Distance to Streams** | 0-200 m | 100 |
| | 200-300 m | 80 |
| | 300-400 m | 50 |
| | 400-500 m | 20 |
| | >500 m | 1 |
| **NDVI** | (-1) - (-0.05) | 1 |
| | 0 - 0.15 | 100 |
| | 0.15 - 0.45 | 70 |
| | 0.45 - 0.65 | 40 |
| | 0.65 - 1 | 5 |
| **TWI** | 0-2 | 1 |
| | 2-6 | 5 |
| | 6-10 | 10 |
| | 10-14 | 70 |
| | 14-18 | 90 |
| | >18 | 100 |

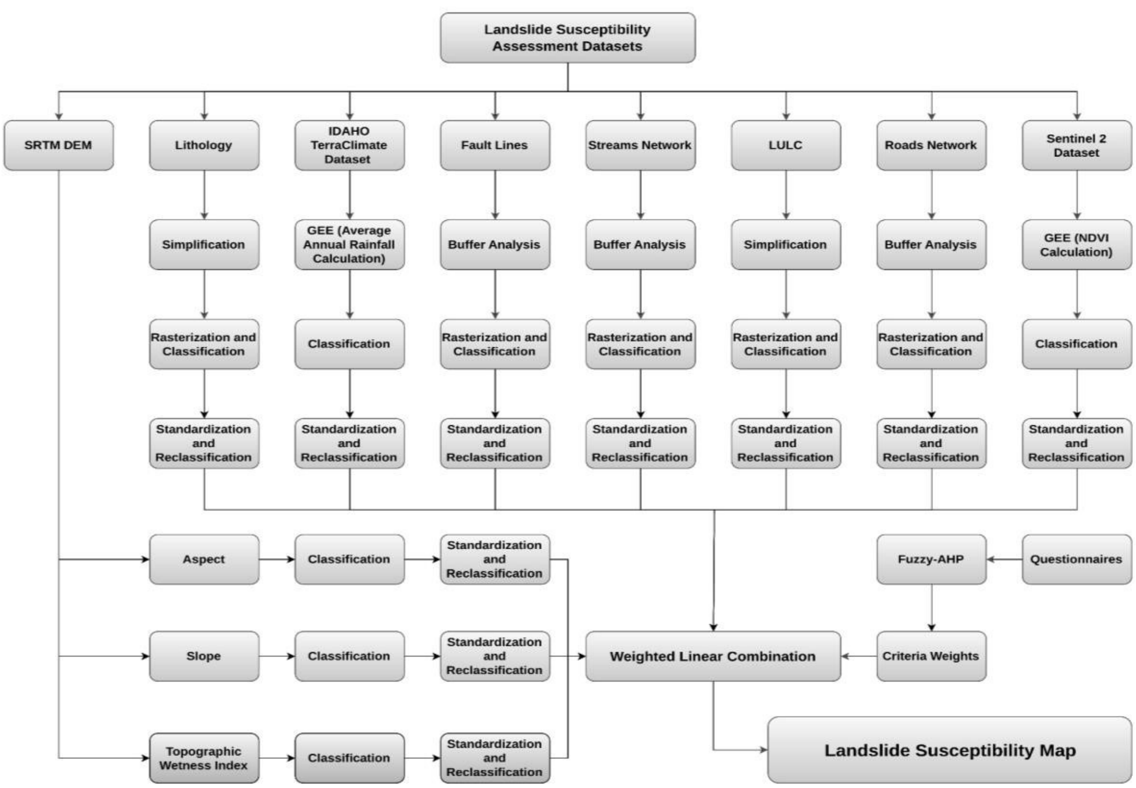


**Figure 4.12.** *The general workflow of the landslide susceptibility mapping*

#### *4.1.7.1. Slope*

Slope angle is the most crucial factor and is commonly used in landslide susceptibility modeling for its direct relation to slope failure, which is the leading cause of landslides (Abdı et al., 2021; Akinci & Yavuz Ozalp, 2021; Ali et al., 2021; Meena, Ghorbanzadeh, & Blaschke, 2019; Meena, Mishra, & Piralilou, 2019; Paryani et al., 2020; Singh et al., 2021; Sujatha & Sridhar, 2021; Sur et al., 2021; Tekin, 2021; Yan et al., 2019).

Slope directly affects the transportation of the material in the presence of gravity. Therefore, it significantly affects erosion potential, soil structure, and slope surface. The higher the slope, the greater the risk of landslide. In addition, it controls underground and surface waters through hydrological processes. Many studies have revealed that landslides are more common in slopes angles that exceed 20° or 15°, while there is a sharp decrease in landslide events at slopes more than 45° (Chun-hao et al., 2018; Gökceoglu & Aksoy, 1996; Nakileza & Nedala, 2020; Nseka et al., 2019; Shano, Raghuvanshi, & Meten, 2021; Sinarta et al., 2017; Yulianto, Suripin, & Purnaweni, 2019). Slopes with 20° to 30° angles are more prone to landslide (Nakileza & Nedala, 2020; Sinarta et al., 2017).

In this study, the slope layer is classified into six classes and is rated based on their significance in landslide susceptibility (Table 4.4). The highest rate was assigned to slopes greater than 20°-40°, while the lowest rating was given to slopes smaller than 15° (Table 4.4). The slope map is shown in Figure 4.13.

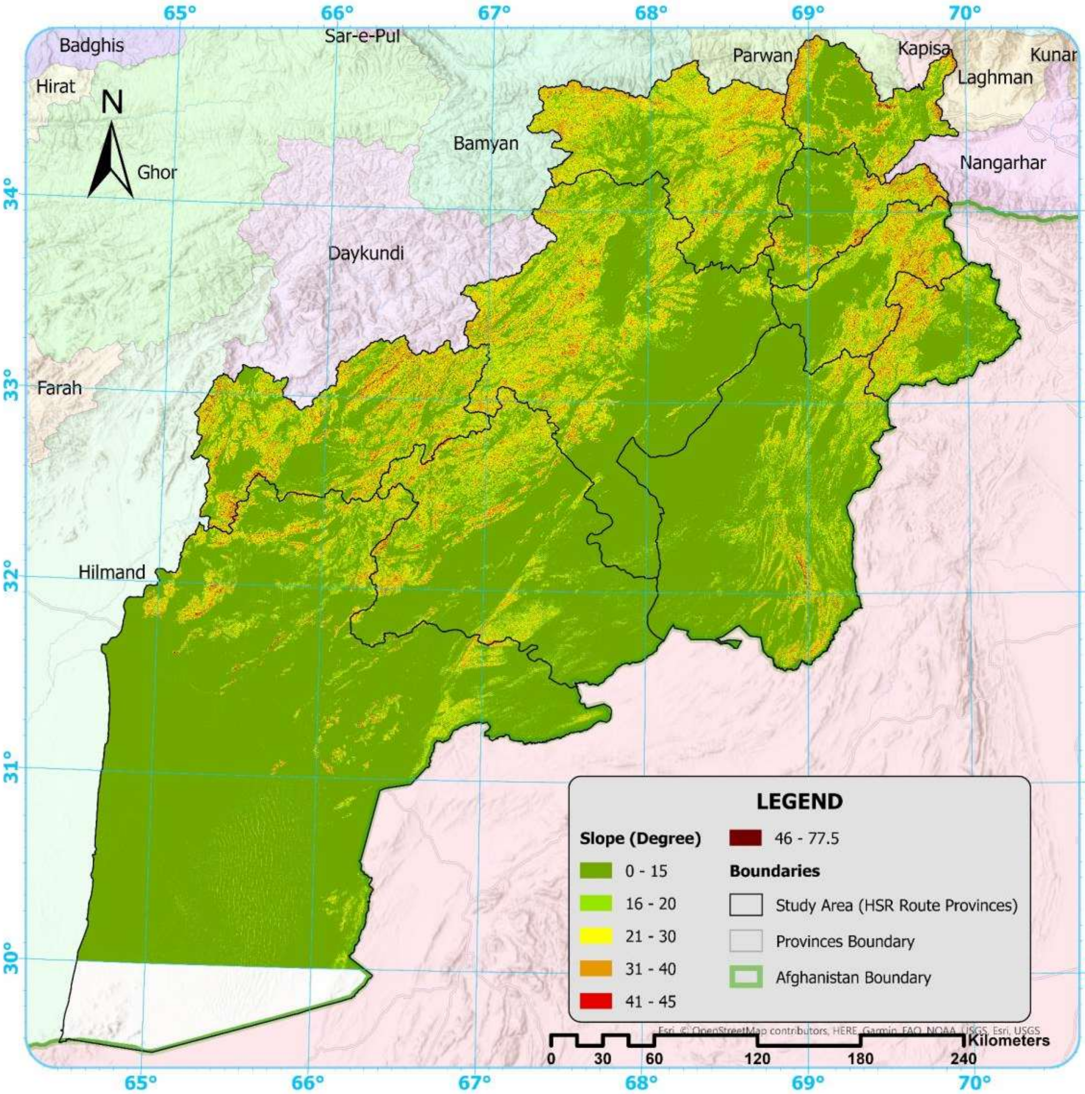


**Figure 4.13.** *The classified slope map, considered in landslide susceptibility mapping*

### *4.1.7.2. Aspect*

The slope aspect has a strong influence on hydrological processes, vegetation growth, amount of rainfall received, wind, and the average amount of sunshine (Abdı et al., 2021; Lila, 2018; Meena, Mishra, & Piralilou, 2019; Shano, Raghuvanshi, & Meten, 2021; Singh et al., 2021; Yan et al., 2019). The most influencing aspect directions are east, southeast, south, southwest, and west directions (Getachew & Meten, 2021; Hammad, 2020; Meena, Ghorbanzadeh, & Blaschke, 2019; Nakileza & Nedala, 2020; Nepal et al., 2019; Yan et al., 2019). The aspect layer is classified into the following nine sub-classes: north (337.5°-22.5°), northeast (22.5°-67.5°), east (67.5°-112.5°), southeast (112.5°-157.5°), south (157.5°-202.5°), southwest (202.5°-247.5°), west (247.5°-

292.5°), northwest (292.5°-337.5°), and flat (-1°) (Table 4.4). The highest ratings were allocated to slopes facing the south and southwest, while the lowest ratings were given to flat, north, and northeast facing slopes (Table 4.4). The slope aspect map is presented in Figure 4.14.

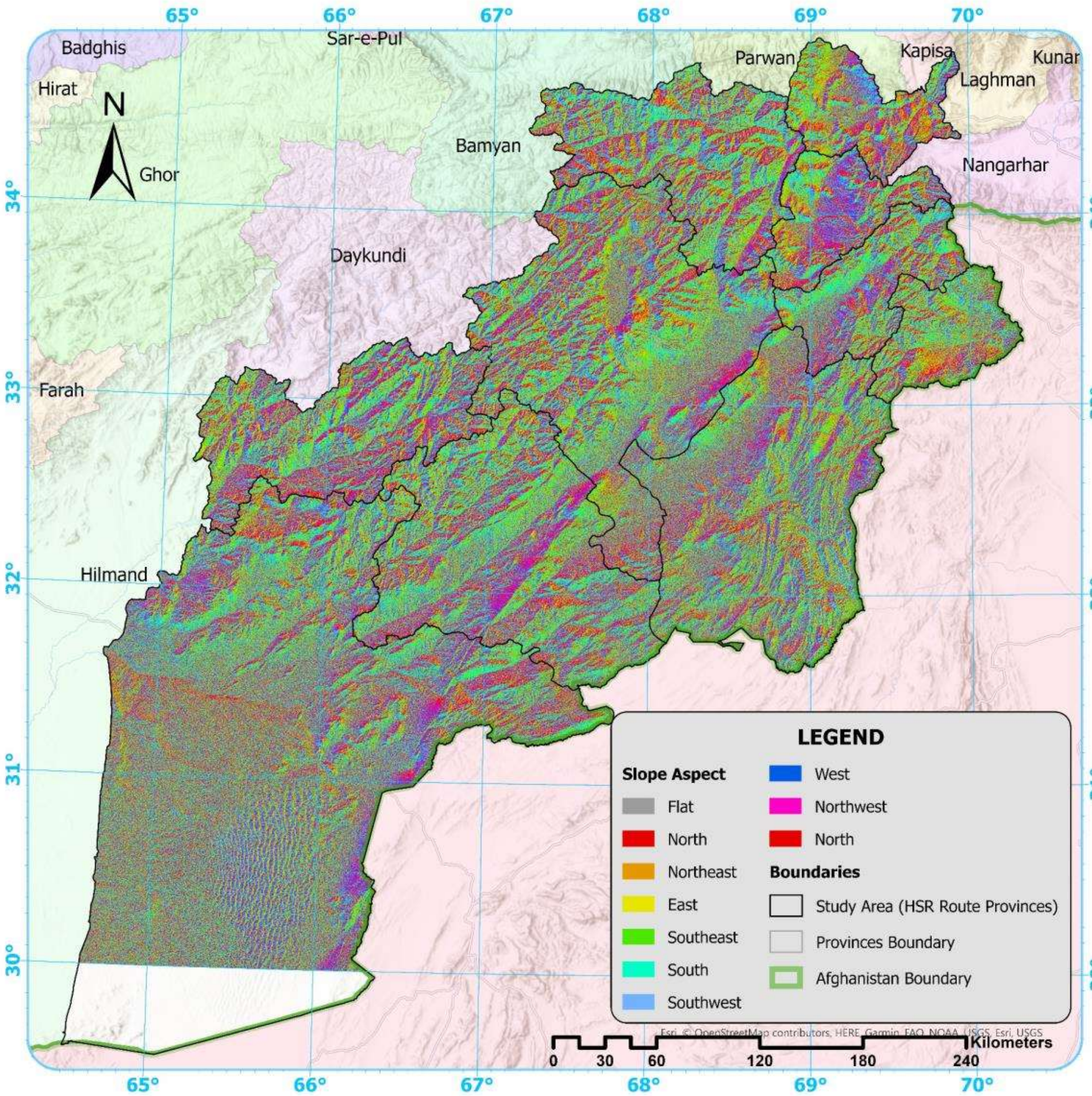


**Figure 4.14.** *The classified slope aspect map of the study area*

### *4.1.7.3. Lithology*

Lithology is another essential factor that determines rocks' strength and absorbency (Sur et al., 2021), and is crucial in landslide susceptibility and slope failure (Abdı et al., 2021; Getachew & Meten, 2021; Lila, 2018; Meena, Mishra, & Piralilou, 2019; Nepal et al., 2019; Wang et al., 2019). Different lithologies correspond to varying frequencies of landslide occurrence in a region (Abdı et al., 2021; Yan et al., 2019). The lithology data obtained from USGS was simplified based on the weathering level and impermeability of the lithological structures with the help of a geology professor from the Kabul Polytechnic University. The study area consists of the following lithological classes: carbonatic rocks, gneiss, schist, quartzite, granites, surficial deposits, ultramafic rocks, and volcanic rocks (Figure 4.15).

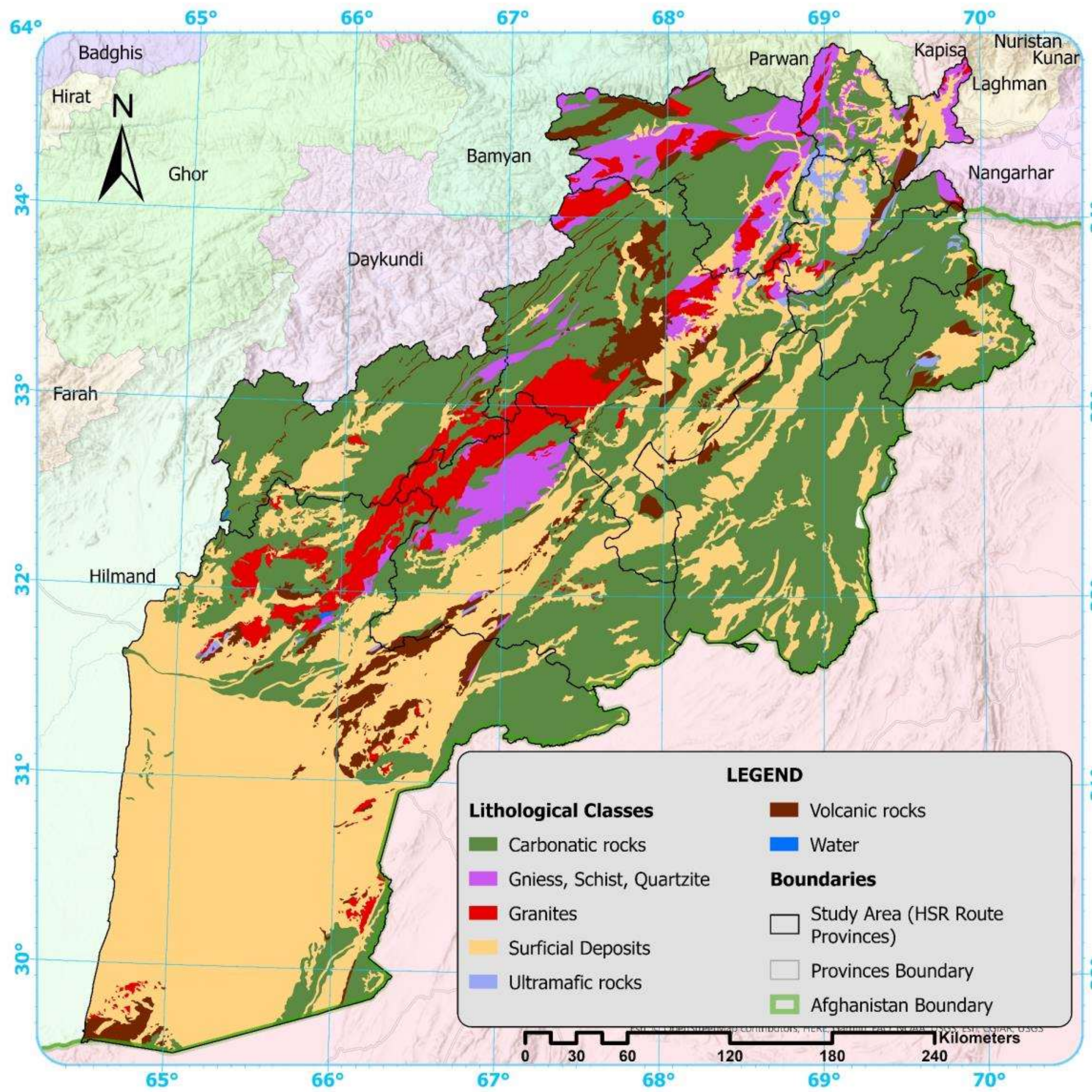


**Figure 4.15.** *The classified lithological map of the study area modified from (Abdullah, Chmyriov, & Dronov, 2008)*

Carbonatic rocks are considered to have the highest probability of forming landslides due to their high weathering level and impermeability (Yulianto, Suripin, & Purnaweni, 2019). Also, volcanic rocks have a high landslide susceptibility rate as a result of their bad shortage and moderate to high weathering levels (Yulianto, Suripin, &

Purnaweni, 2019). Geological fractures are very common in volcanic rocks that occur due to the burden of water infiltration in rocks and can trigger landslides (Yulianto, Suripin, & Purnaweni, 2019). The occurrence of fracture decreases the resistance level of rocks by affecting their bending power and creates a path for water, which can cause weathering and erosion that will lead to landslides (Yulianto, Suripin, & Purnaweni, 2019). The study area is covered dominantly by two lithologic units, carbonatic rocks and surficial deposits. The lithology layer was classified into seven classes. The highest ratings were assigned to carbonatic rocks and volcanic rocks, followed by ultramafic rocks, granites, gneiss, schist, quartzite, and surficial deposits (Table 4.4).

#### *4.1.7.4. Rainfall intensity*

High-intensity rainfall is the primary triggering factor of landslides (Getachew & Meten, 2021; Nakileza & Nedala, 2020; Nepal et al., 2019; Shano, Raghuvanshi, & Meten, 2021; Wang et al., 2019). Heavy rainfall in a short duration causes slope instability by increasing soil weight and pore water pressure (Getachew & Meten, 2021; Nepal et al., 2019; Shano, Raghuvanshi, & Meten, 2021; Wang et al., 2019). Heavy rainfall causes saturation in slope materials and adds extra weight; this leads to decreased shear strength and increased shear pressure in slope material and initiates a landslide (Getachew & Meten, 2021). The majority of the landslides occur during the wet season in the study area. The rainfall intensity must be greater than 40 millimeter per hour (mm/h) to trigger an avalanche (Liu, Deng, & Wang, 2021). The rainfall intensity is directly related to the landslide's earlier occurrence (Liu, Deng, & Wang, 2021). At rainfall intensity of 120 mm/h, the likelihood of landslide occurrence is very high and can trigger an avalanche in less than 39 minutes (Liu, Deng, & Wang, 2021).

The rainfall seasons start from mid-December and continue until the end of May in the study area. The rainfall data layer is prepared in GEE API using the TerraClimate dataset of IDAHO University (Abatzoglou et al., 2018). The average rainfall for the rainfall session was calculated in two intervals from 2000 to 2005 and 2016 to 2021. The rainfall map (Figure 4.16) was classified into six classes considering the rainfall intensity classification scale and is rated based on their influence on landslide susceptibility (Table 4.4). The highest rating was assigned to rainfall intensity of greater than 100 millimeters (mm) subclass and the lowest to 12 mm subclass (Table 4.4).

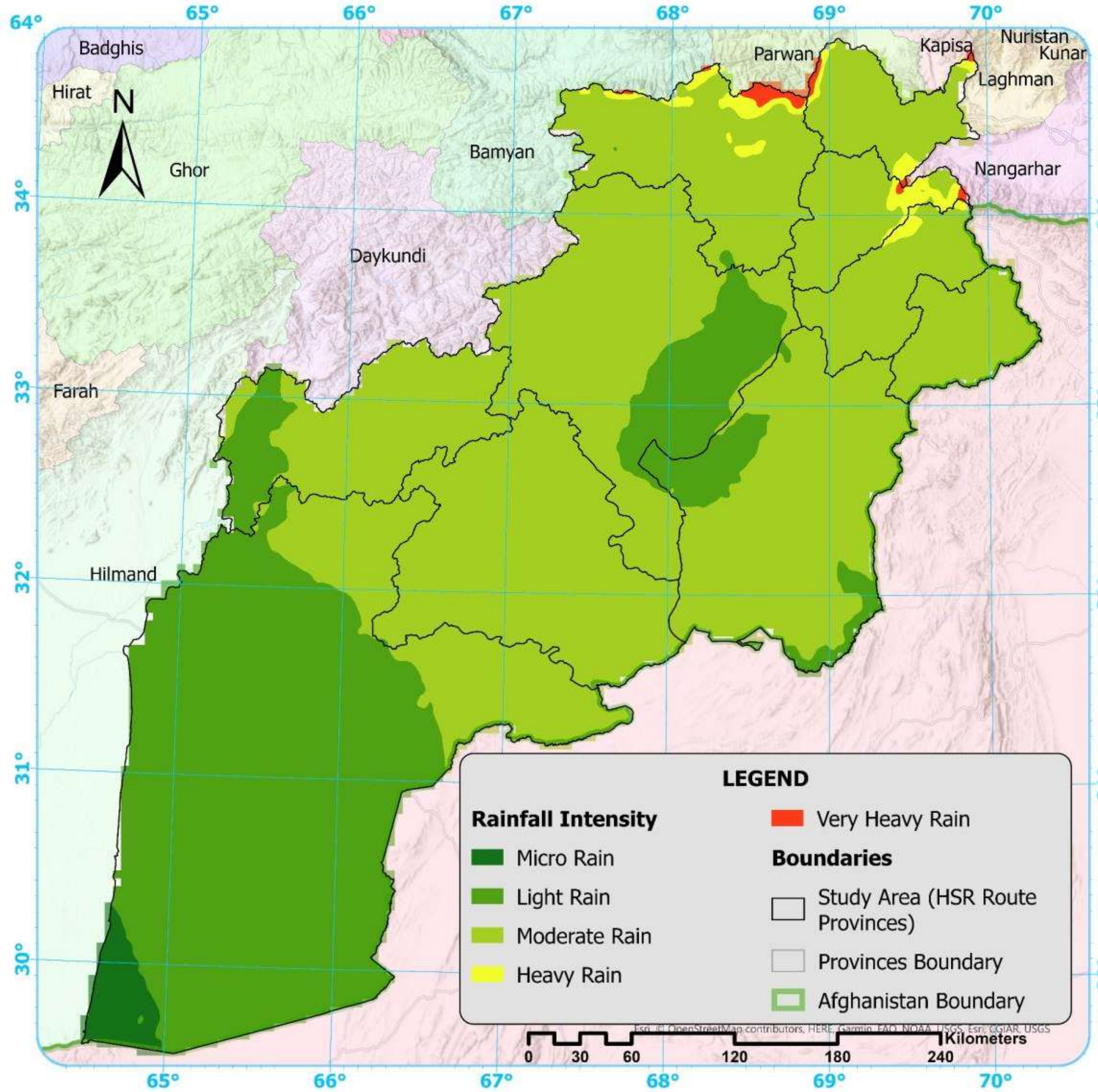


**Figure 4.16.** *The classified rainfall intensity map of the study area*

### *4.1.7.5. Distance from faultlines*

By creating gaps between two distinctive lithological units, generating fractures and joints within the lithological units, faults can have a more substantial effect on slope instability and cause a landslide (Abdı et al., 2021; Meena, Mishra, & Piralilou, 2019; Yan et al., 2019). Therefore, areas near faultlines are more susceptible to landslides, especially areas with active faultlines. Akinci and Yavuz Ozalp (2021) found that there is a high possibility of landslides occurrence at a distance up to 655 m from faultlines. Considering the geographical location of the study area, distance to faultlines shows variation. Jiao et al. (2019) stated that areas at 1200 m or closer to faultlines are more susceptible to landslides, while Wang et al. (2019) and Chen et al. (2019) concluded that areas closer than 1000 m are more prone to landslides. In another study conducted by Hammad (2020), it is revealed that 82.32% of landslides are occurred in a distance less than 500 m, with roughly 77.37% at a distance up to 300 m from faultlines, and 17.66% have occurred in the distance more than 500 m. According to the faultline dataset of Afghanistan, the study area contains more than 139 ascertained faults; some of these faultlines are active but most of them are inactive. The study area is prone to risk from 11 active faultlines considered in this study (Figure 4.17). Considering the intensity of earthquakes in the study areas, distance to faults was classified into five buffer zones at intervals of 0-300 m, 300-500 m, 500-1000 m, 1000-2000 m, 2000-3000 m, and >3000 m (Table 4.4). These sub-classes are rated based on their significance in landslide susceptibility (Table 4.4).

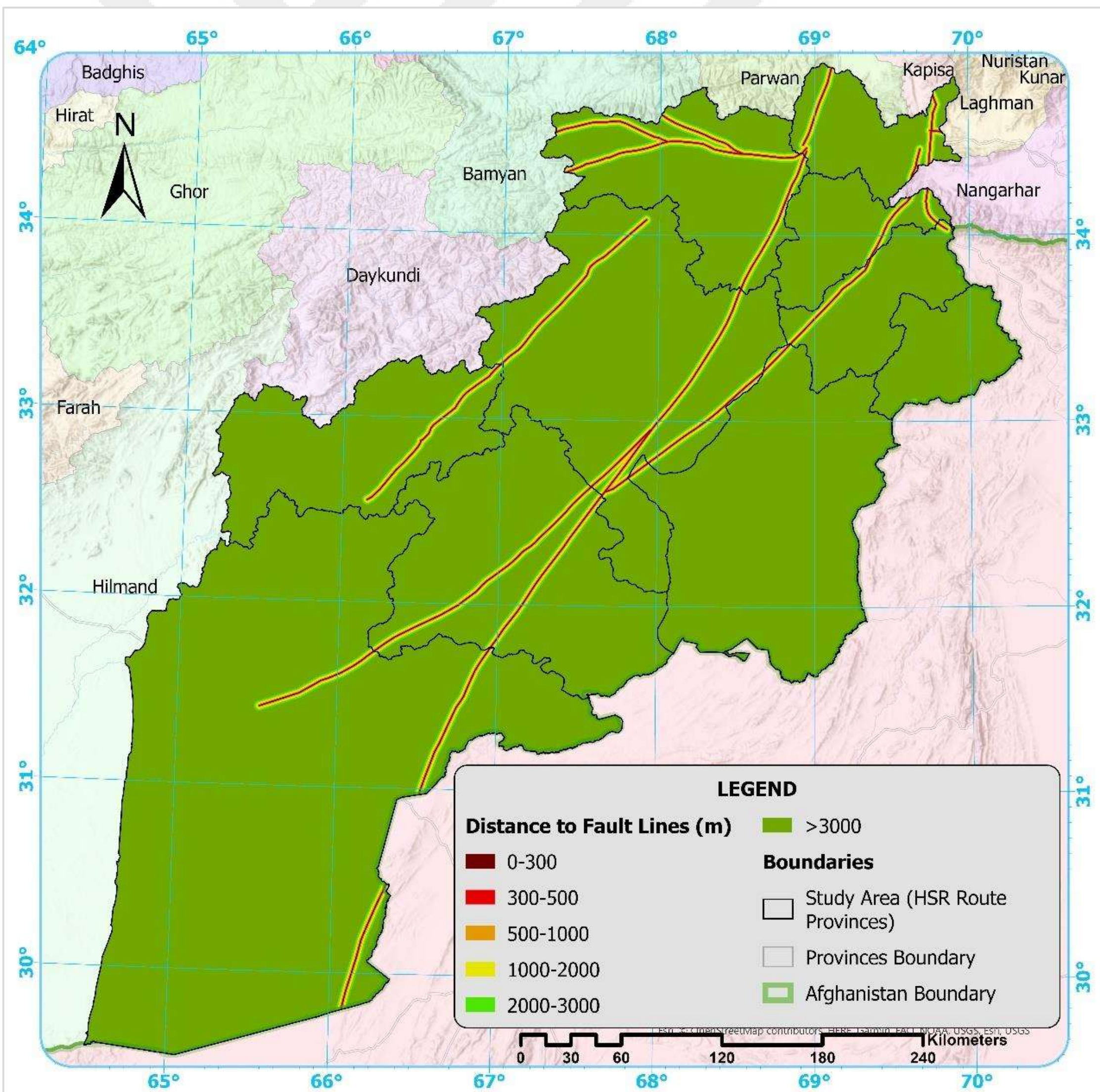


**Figure 4.17.** *The distances to faultlines, considered in landslide susceptibility mapping modified from (Abdullah, Chmyriov, & Dronov, 2008; Wheeler et al., 2005)*

#### *4.1.7.6. Distance from streams*

Streams are one of the significant factors that affect landslide susceptibility for their ability to cause erosion, a saturation of material, and debris flow in lower parts of the valleys (Getachew & Meten, 2021; Goumrasa, Guendouz, & Guettouche, 2021; Meena, Ghorbanzadeh, & Blaschke, 2019; Meena, Mishra, & Piralilou, 2019; Richard, 2020; Singh et al., 2021; Yan et al., 2019).

Landslides are more susceptible in areas at a distance smaller than 200 m (Wang et al., 2019). Landslides density can be high at a distance of more than 300 m compared to smaller distances as a result of the combination of other factors and their influence on the landslide susceptibility (Getachew & Meten, 2021; Jiao et al., 2019). The study conducted by (Jiao et al., 2019) stated that areas at 200-400 m and 400-600 m from a river have the highest landslide susceptibility rate.

Generally, at a distance smaller than 200 m from rivers, the erosion process causes slope instability and paves the way for landslide occurrence at a distance greater than 200 m. In this study, five buffer zones are created at distance intervals of 0-200 m, 200-300 m, 300-400 m, 400-500 m, and >500 m from the rivers (Table 4.4) (Figure 4.18). These buffer zones are rated according to their influence on the landslide producing potential (Table 4.4).

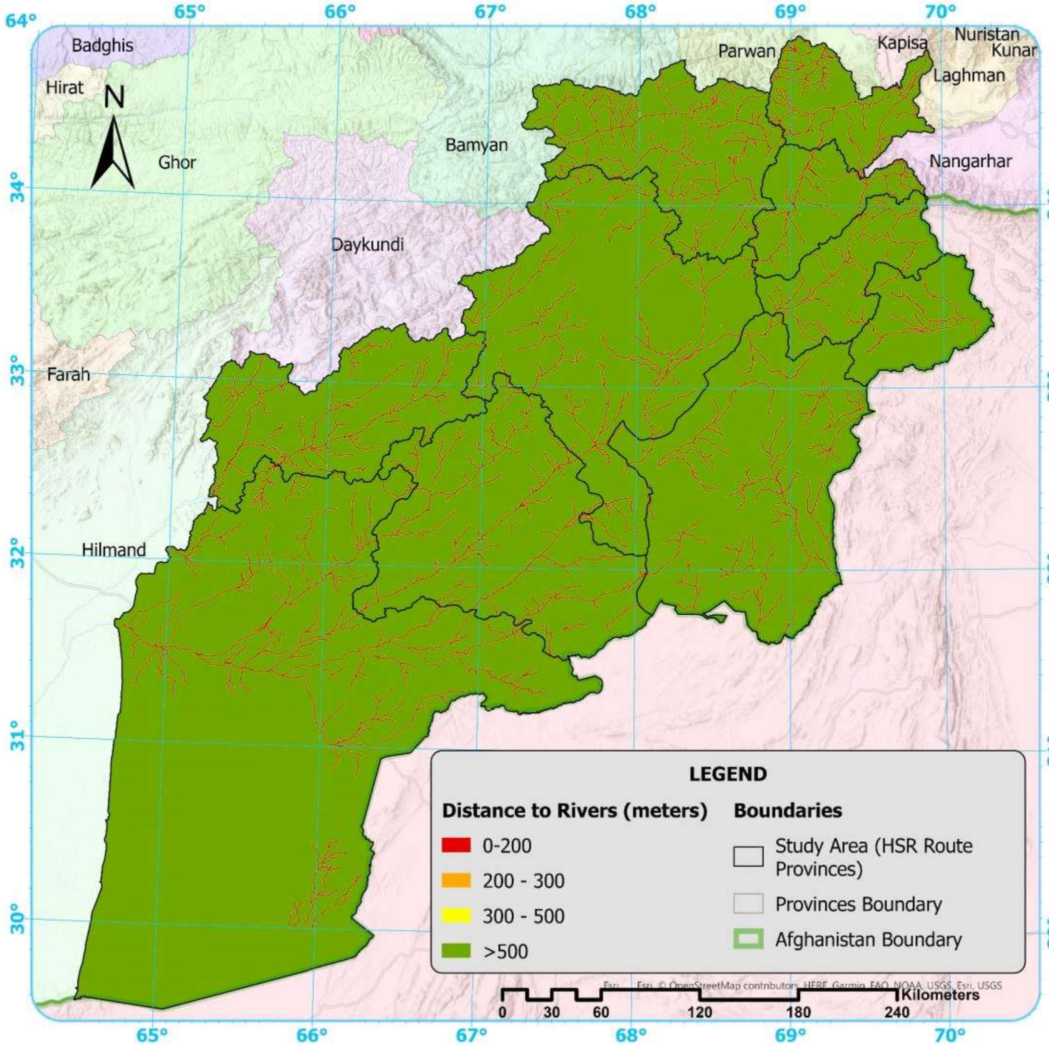


**Figure 4.18.** *The distance to rivers, considered in landslide susceptibility mapping*

### *4.1.7.7. Landuse/landcover*

LULC has a significant influence on landslide susceptibility, and a considerable number of landslides are occurred on slopes with sparse vegetation or bare lands compared to slopes having dense vegetation, forest, and settlements (Abdı et al., 2021; Lila, 2018). Several studies have showed that landslides are frequently triggered directly by the LULC changes in an area, which indicate a strong connection with the landslide susceptibility (Sur et al., 2021). Mostly, the rainfed agricultural, spare forest, and grassland with moderate coverage are highly prone to landslides (Liu, Wu, & Zhang, 2021), following by barren lands (Nepal et al., 2019). In this study, the highest ratings were given to rainfed agricultural lands, rangelands, and barren lands, while the lowest ratings are assigned to vineyards, fruit trees, and build up areas (Table 4.4). The LULC map of the study area is presented in Figure 4.3.

#### *4.1.7.8. Distance from roads*

Human intervention, specifically road construction, has a substantial role in increasing the landslide risk. Road undercutting during road construction causes a decrease in the load on the slope toe, which leads to slope instability (Abdı et al., 2021; Lila, 2018; Meena, Mishra, & Piralilou, 2019; Singh et al., 2021; Sujatha & Sridhar, 2021; Yan et al., 2019). The highest landslide risk is associated with the areas located at less than 200 m from roads, while regions at a distance more than 1000 m have a very low landslide susceptibility (Akinci & Yavuz Ozalp, 2021; Paryani et al., 2020; Wang et al., 2019). In this study, the distance from the roads layer is classified into six different classes considering their influence on landslide susceptibility (Table 4.4) (Figure 4.19). The highest rating was assigned to distances less than 200 m, while the lowest rate was assigned to areas at 1000 m or greater distance from roads (Table 4.4).

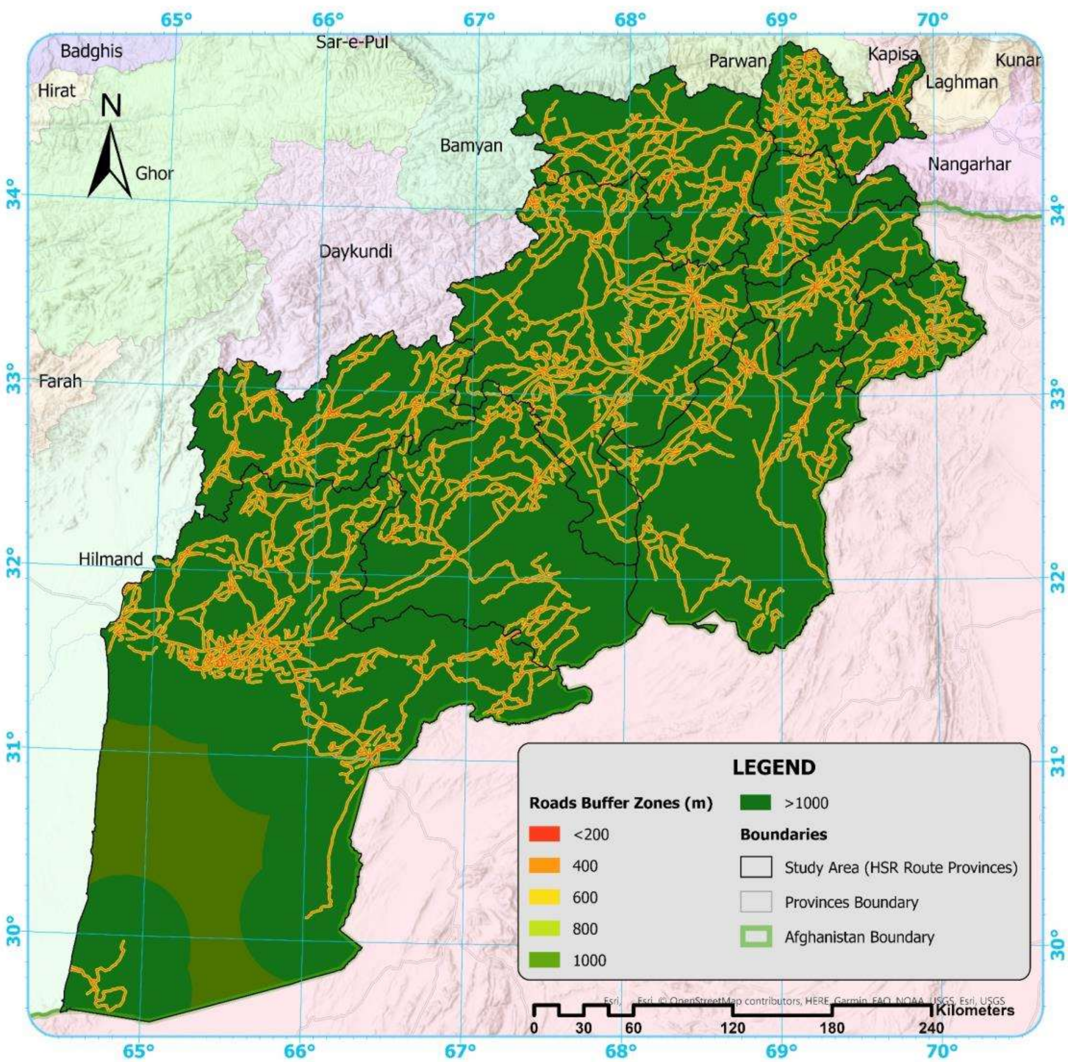


**Figure 4.19.** *The distances from roads, considered in landslide susceptibility mapping*

### *4.1.7.9. Normalized difference vegetation index*

Vegetations strengthen slopes, protect slopes from erosion, and stabilize slopes (Abdı et al., 2021; Goumrasa, Guendouz, & Guettouche, 2021). The likelihood of landslide in areas with higher NDVI values is very low compared to those with lower NDVI values (Abdı et al., 2021; Hammad, 2020; Wang et al., 2019). The NDVI was generated from Sentinel-2 satellite imagery products in the GEE API and was classified into five classes (Table 4.4) (Figure 4.20). Generally, plants have positive NDVI values, in the current study, from 0.15 to 1, while values between -1 to -0.05 and -0.05 to +0.15 represent water and bare rocks; soil, sands, and snow, respectively. The values between 0.15 to 0.45 corresponds to spare vegetation, 0.45 to 0.65 indicate moderate vegetations, and values greater than 0.65 represent very dense vegetations (Table 4.4).

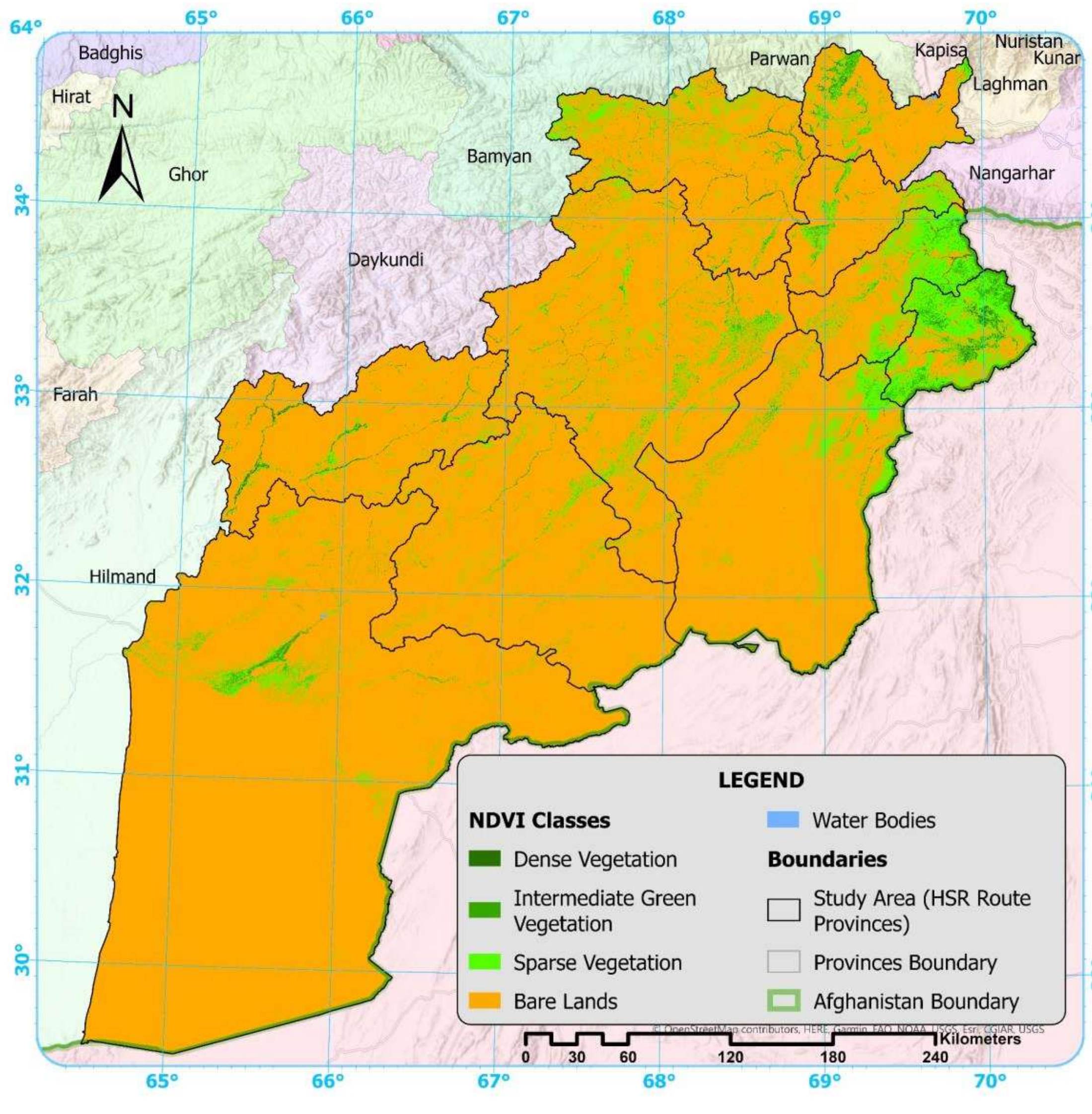


**Figure 4.20.** *The NDVI thematic map, considered in landslide susceptibility mapping*

*4.1.7.10. Topographic wetness index*

Soil moisture is the initial factor in landslide susceptibility that must be considered but it is very complicated to map it spatially; therefore, the TWI can be used as an alternative regardless of some of its shortcomings (Sujatha & Sridhar, 2021). The TWI can assist in detecting water-saturated zones with surface runoff potential (Abdı et al., 2021; Singh et al., 2021; Sujatha & Sridhar, 2021; Tekin, 2021). Generally, areas with high TWI are more saturated, resulting in slope failure due to the decrease in shear strength of the substances in the area (Nseka et al., 2019). Generally, valleys bottoms have the highest TWI values of >18 , corresponding to high saturation, but it does not lead to landslides in the valley's depths (Nseka et al., 2019). The TWI layer was produced from the DEM dataset using the TWI tool in SAGA-GIS software. In the study area, the TWI index values change between 2 to 26.8 and are classified into five subcategories by utilizing the commonly used classification in literatures (Table 4.4) (Figure 4.21).

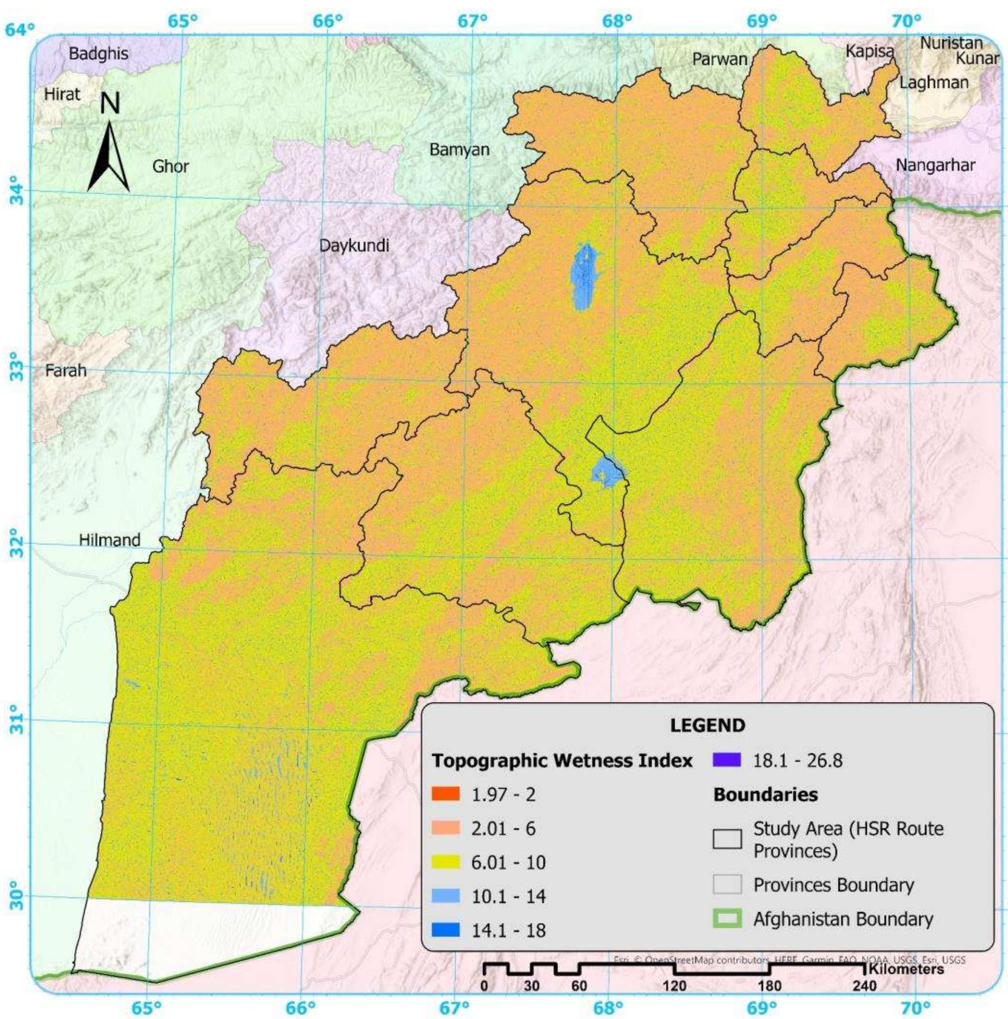


**Figure 4.21.** *The TWI thematic map of the study area*

#### 4.1.8. Snow avalanche susceptibility

Snow avalanches are also amongst the most devastating natural disasters that pose a serious threat to transportation networks. Snow avalanches are extremely devastative natural disasters with a flow speed of up to 200 km/h and a pressure up to 50 T/$m^3$ which can destroy every obstacle on their way and bring heavy casualties, property damage, and destruction to road and railway networks (Choubin et al., 2020; Nasery & Kalkan, 2021; Soteres, Pedraza, & Carrasco, 2020; Tiwari & Vishwakarma, 2021). Most of the railway tracks and roads routes in topographically complex regions are constructed in the depth of the valleys or hillsides that are prone to avalanches. Therefore, it is very important to assess the avalanche risk along the HSR alignment route thoroughly.

From the avalanche formation perspective, loose snow avalanches and slab avalanches are the two forms of avalanches occurring due to poor connection between snow crystals on the surface and failure in the depth of snow, respectively (Nasery & Kalkan, 2021). Snow avalanches' path has three characteristics, the starting zone, the track, and the runout zone (Akay, 2021). Avalanches can carry a massive amount of snow with debris containing rocks, soil, and vegetation to the runout zone (Choubin et al., 2020; Yariyan et al., 2020). External forces such as the weight of fresh snow, wind gusts, tourism, and winter sports activities have a substantial role in triggering avalanches combined with other factors (Singh et al., 2021; Yariyan et al., 2020). The factors triggering or preparing the atmosphere for forming an avalanche are classified as static terrain and dynamic metrological factors (Nasery & Kalkan, 2021; Singh et al., 2018; Varol, 2022; Yariyan et al., 2020). Static terrain factors are elevation, slope, curvature, aspect, land cover, and so on; dynamic factors include snowpack attributes and metrological conditions (temperature, snowfall, wind speed, precipitation) (Kumar, Srivastava, & Snehmani, 2018; Parshad et al., 2017; Singh et al., 2018). Numerous studies conducted on snow avalanche susceptibility mapping adopted static terrain factors combined with dynamic metrological factors (Akay, 2021; Choubin et al., 2020; Nasery & Kalkan, 2021; Singh et al., 2021; Varol, 2022).

In this context, the primary goal of this part of the research is to create an avalanche susceptibility model based on GIS and MCDA methodologies to produce a reliable avalanche susceptibility map. The susceptibility maps are produced using fuzzy-AHP method. Slope, elevation, aspect, curvature, LULC, length of slope, terrain roughness, temperature, precipitation, and wind are considered effective factors in snow avalanche formation and triggering in the study area. The general workflow of the study and data processing steps are shown in Figure 4.22.

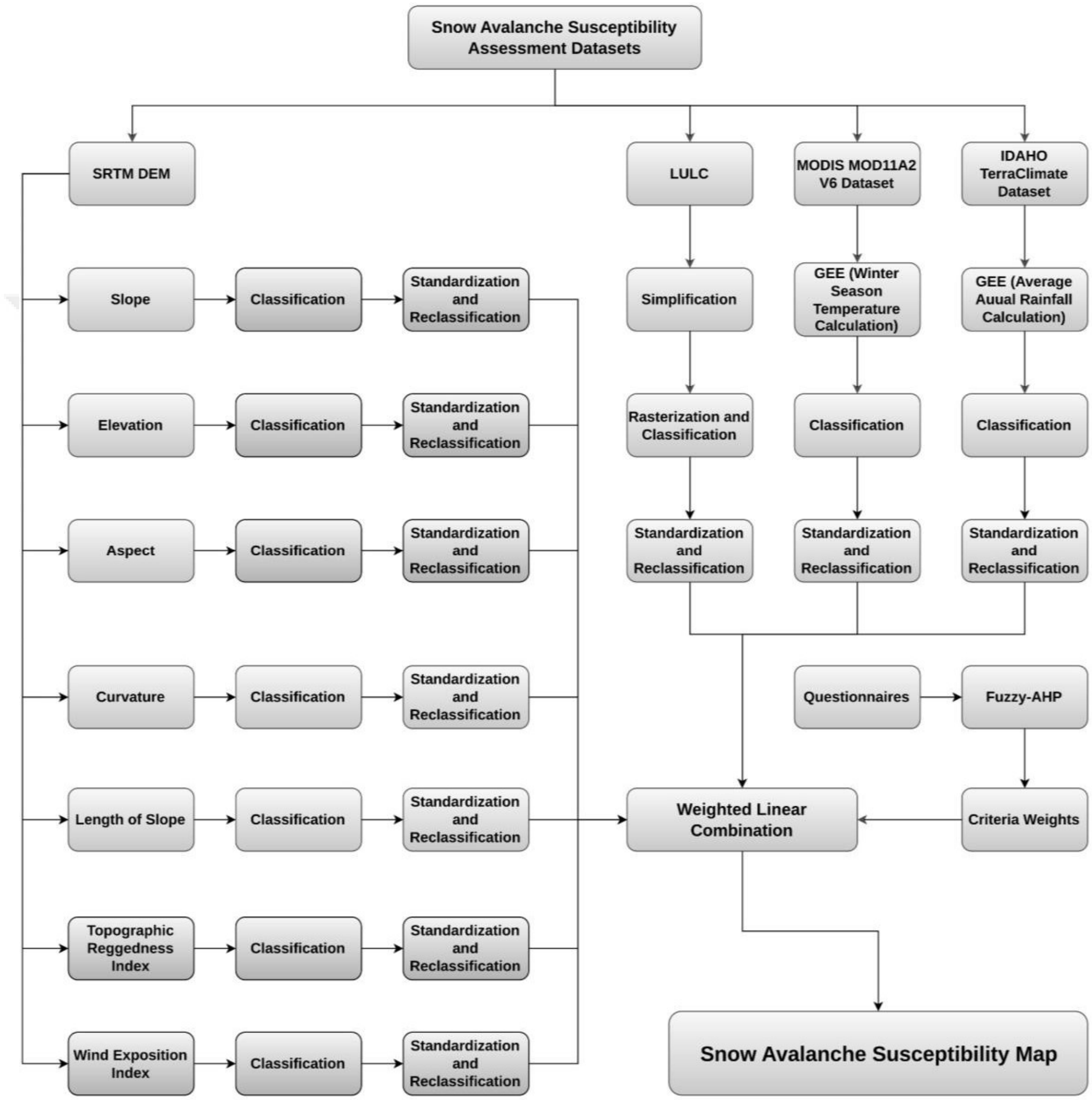


**Figure 4.22.** *The general workflow of the snow avalanche susceptibility analysis*

#### *4.1.8.1. Slope*

The slope is the most prominent terrain factor for avalanches which is directly related to the starting motion, path, velocity, and employing pressure of avalanches (Kumar et al., 2019; Kumar, Srivastava, & Snehmani, 2018; Nasery & Kalkan, 2021; Parshad et al., 2017; Rahmati et al., 2019; Singh et al., 2018; Varol, 2022; Yariyan et al., 2020). Avalanches are frequently occurring in areas with 25° to 45° slope (Kumar et al., 2019; Kumar, Srivastava, & Snehmani, 2018; Nasery & Kalkan, 2021; Parshad et al., 2017; Singh et al., 2018), majority of devastative and big avalanches occur at slopes between 28° to 45° (Kumar et al., 2019; Nasery & Kalkan, 2021; Parshad et al., 2017). The accumulated snow on slopes more than 55° is low and small avalanches are frequent in these areas (Choubin et al., 2020; Kumar et al., 2019; Nasery & Kalkan, 2021; Parshad et al., 2017). The slope layer was categorized into six classes considering the snow avalanche generation potential of the slope (Table 4.5) (Figure 4.23). The highest rating was allocated to the slope range of 35-45°, while slopes smaller than 12° were assigned the lowest rating (Table 4.5).

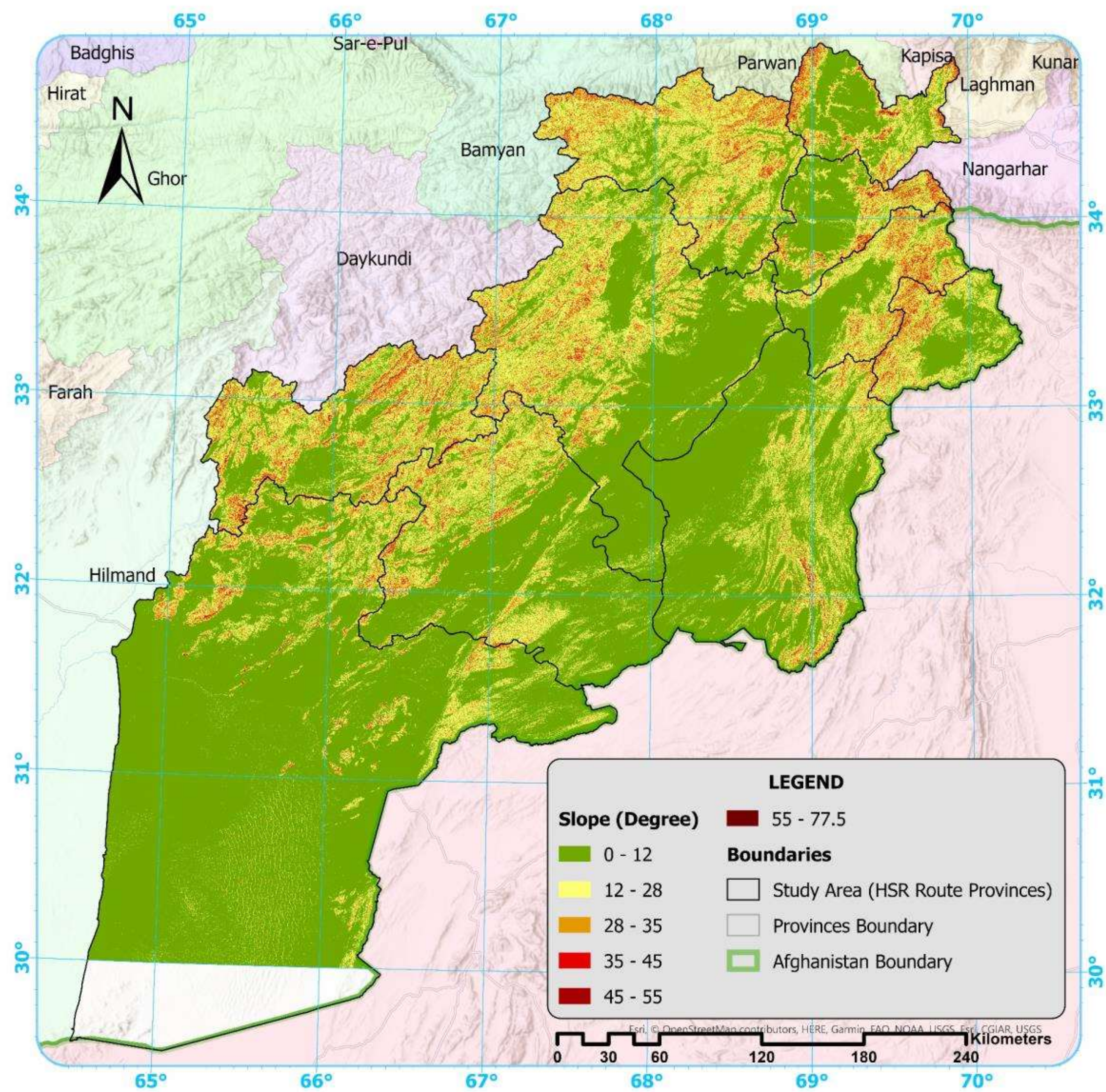


**Figure 4.23.** *The classified slope map, considered in snow avalanche susceptibility analysis*

### *4.1.8.2. Elevation*

Elevation has an indirect effect in increasing avalanche susceptibility, but through its influence on metrological factors (Choubin et al., 2020; Nasery & Kalkan, 2021; Rahmati et al., 2019). The low temperature and gale in high altitudes ensure snow deposition for a longer duration, thus increasing the avalanche susceptibility (Kumar et al., 2019; Nasery & Kalkan, 2021; Parshad et al., 2017; Yariyan et al., 2020). Furthermore, elevation can help avalanches deposit more debris in the runout zone by increasing the relative density of snow that destroys the rocky outcrops and top layers of soil on the avalanche track (Choubin et al., 2020). The elevation layer is classified into 7 classes (Table 4.5) and is shown in Figure 4.24.

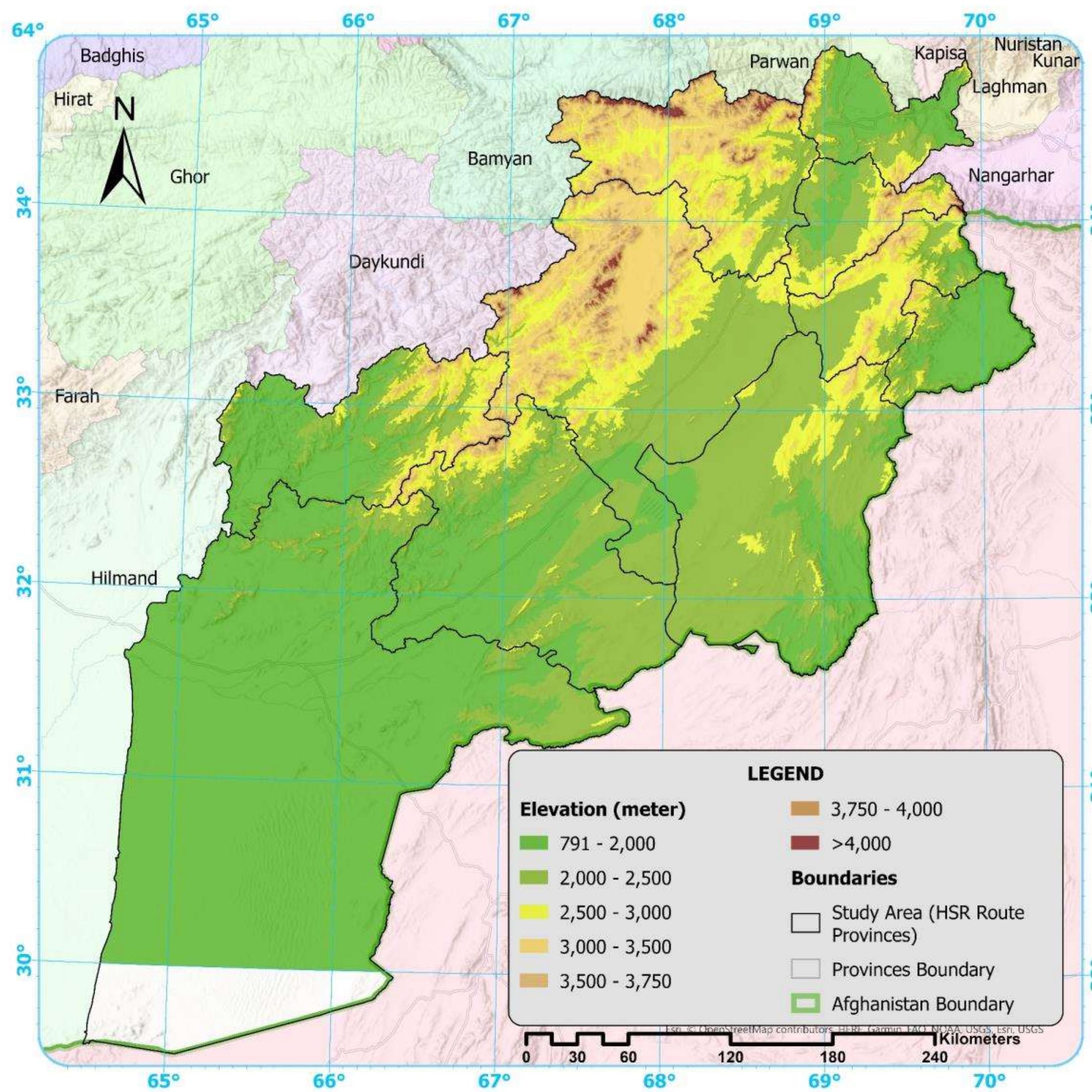


**Figure 4.24.** *The classified elevation map, considered in snow avalanche susceptibility analysis*

#### *4.1.8.3. Aspect*

Avalanches can happen on any slope aspect (Singh et al., 2018; Yariyan et al., 2020), but the amount of solar radiations have variation on the different orientation of slope which has a direct relation with snowpack stability (Choubin et al., 2020; Kumar, Srivastava, & Snehmani, 2018; Nasery & Kalkan, 2021; Varol, 2022; Yariyan et al., 2021). Snowpacks on shady slopes are unstable compared to slopes facing the sun (Kumar, Srivastava, & Snehmani, 2018; Parshad et al., 2017). Aspect is classified into nine classes which are shown in (Table 4.5) (Figure 4.14). In the study area, slopes facing north, and northeast directions receive a minimum amount of sunshine during a day, therefore they were assigned the highest rating. The lowest rating was assigned to flat areas where the avalanche susceptibility is very low (Table 4.5).

#### *4.1.8.4. Curvature*

Curvature has an essential role in snow avalanche susceptibility. Convex slopes are more prone to avalanches compared to concave and flat slopes (Kumar et al., 2019; Nasery & Kalkan, 2021; Parshad et al., 2017; Singh et al., 2018; Varol, 2022; Yariyan et al., 2021). In an ideal situation for an avalanche, the snowpack cracking first starts in convex slopes (Choubin et al., 2020). Generally, snowpacks on convex slopes are unstable while stabilized on concave slopes and flat regions. The study area was classified into convex, concave, and flat categories and are rated based on their significance to avalanche susceptibility (Table 4.5) (Figure 4.25).

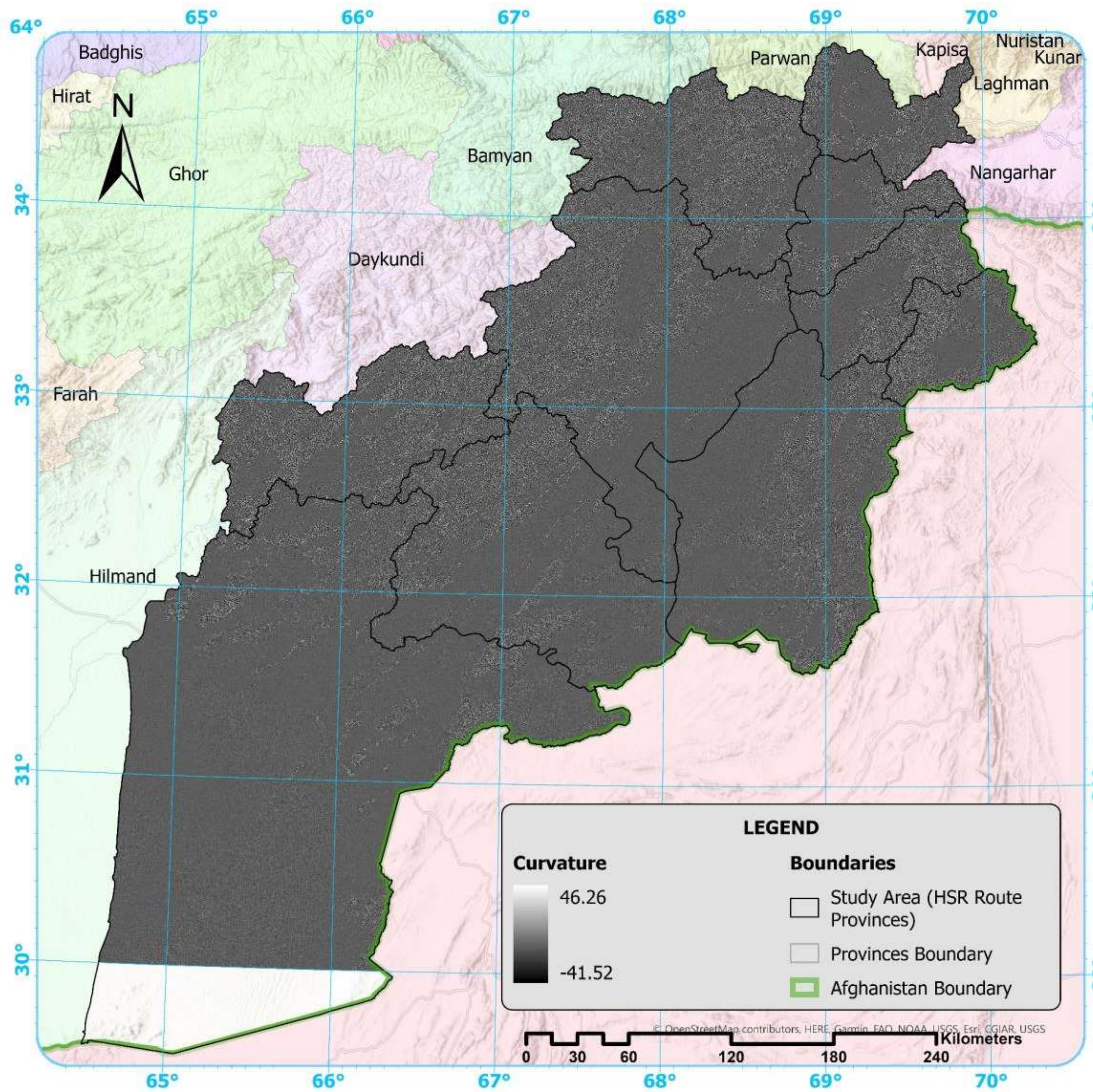


**Figure 4.25.** *The classified curvature map of the study area*

### *4.1.8.5. Landuse/landcover*

LULC is a crucial factor for avalanche susceptibility (Kumar et al., 2019; Nasery & Kalkan, 2021; Rahmati et al., 2019; Singh et al., 2018). Specific land cover types contribute to avalanche susceptibility while others decrease avalanche initiation. Generally, vegetated and forestry areas are reducing the initiation chance and intensity of avalanches by providing anchoring to snow on slopes, while bare lands and rangelands have the highest avalanche susceptibility rate (Choubin et al., 2020; Kumar et al., 2019; Nasery & Kalkan, 2021; Parshad et al., 2017; Rahmati et al., 2019; Singh et al., 2018). There are 11 LULC classes in the study area that are shown in Table 4.5. The highest rating was allocated to barren lands, permanent snow cover, and rangelands, and the lowest ratings are given to build-up areas, water bodies, and sand cover classes (Table 4.5) (Figure 4.3).

#### *4.1.8.6. Length of slope*

The length of the slope is also significant in triggering and expanding avalanches at the starting zone. The length of the slope is calculated perpendicular to the contours in an area (Mosavi et al., 2020). Normally a steep slope with a short length cannot trigger an avalanche or assist it is getting bigger at the starting zone (Teich et al., 2012). Slope lengths longer than 200 m are posing moderate, while slopes longer than 400 m pose a high risk in forested areas, combined with other factors (Teich et al., 2012; Weir, 2002). (Mosavi et al., 2020) classified the slope length into five classes of 0-11 m, 11-18 m, 18-25 m, 25-35 m, and 35-104 m. Similarly, (Margreth, 2013) categorized the slope length into three classes of 0-15 m, 15-30 m, and greater than 30 m. Generally, the avalanche start-zone with a slope length of 20 m or greater is highly prone to initiate avalanches. The slope length layer was classified into six classes considering their avalanche initiation risk level (Table 4.5) (Figure 4.26). The highest rating was given to slope lengths smaller than 20 m, whereas the highest rating was assigned to slope lengths greater than 400 m (Table 4.5).

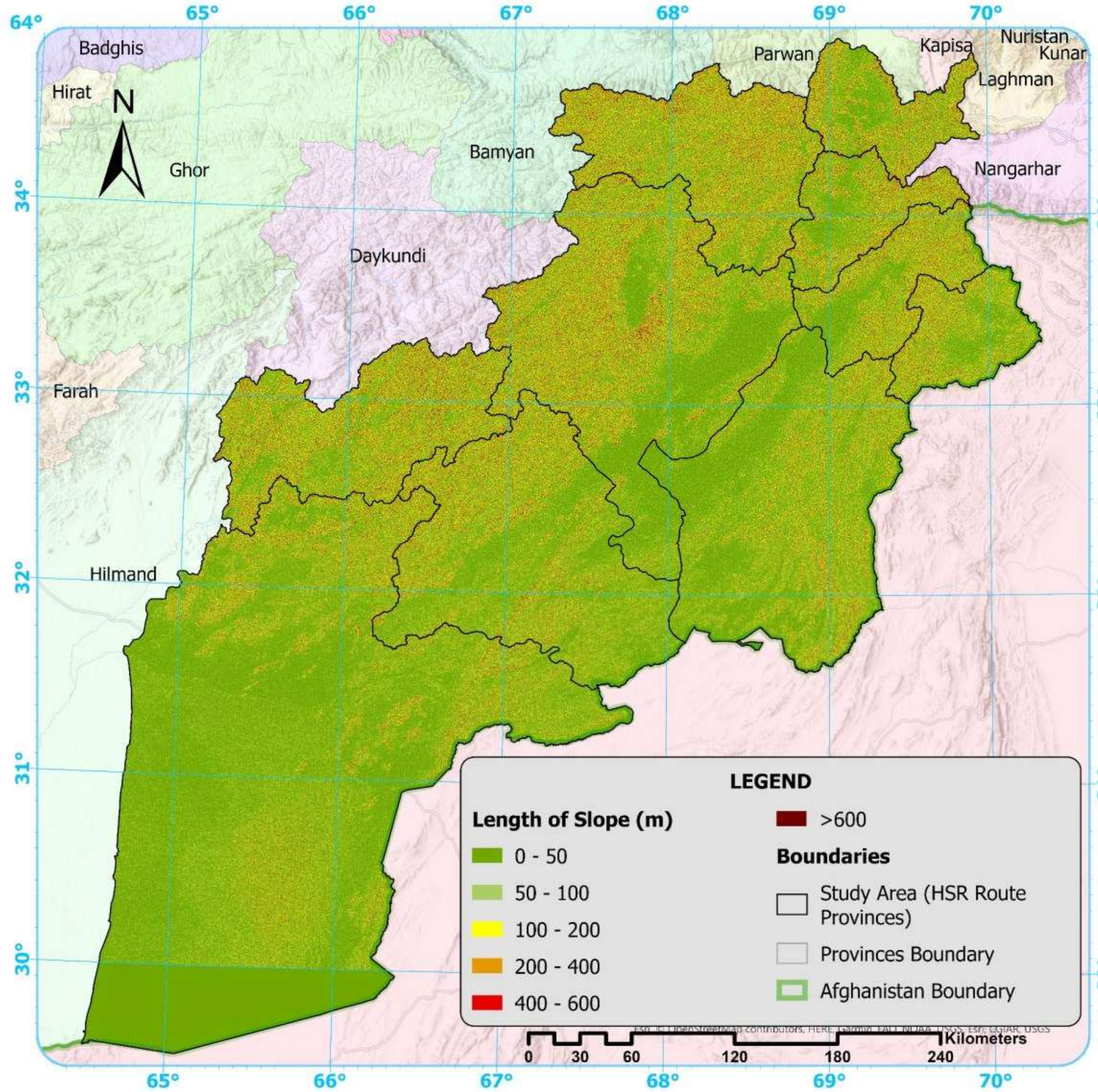


**Figure 4.26.** *The classified slope length map, considered in snow avalanche susceptibility analysis*

### *4.1.8.7. Topographic ruggedness index*

The snowpacks on rough surfaces are not uniformly formed; hence terrain roughness/ruggedness provides a good grip for snowpacks in every layer of snow and prevents its sliding (Brožová et al., 2021; Kumar, Srivastava, & Snehmani, 2016; Rahmati et al., 2019; Veitinger, 2015). Typically, large avalanches have a more homogeneous snowpack, while small avalanches have more variations in their snowpacks (Veitinger, 2015). Terrain roughness determines the avalanche path and runout distance (Brožová et al., 2021). The terrain roughness can be effectively mapped using the TRI index developed by (Riley, DeGloria, & Elliot, 1999), representing the terrain heterogeneity.

TRI was calculated in SAGA-GIS software and was classified into seven classes (Table 4.5) (Figure 4.27). The resulting TRI layer was subjected to rating based on their influence on avalanche occurrence (Table 4.5).

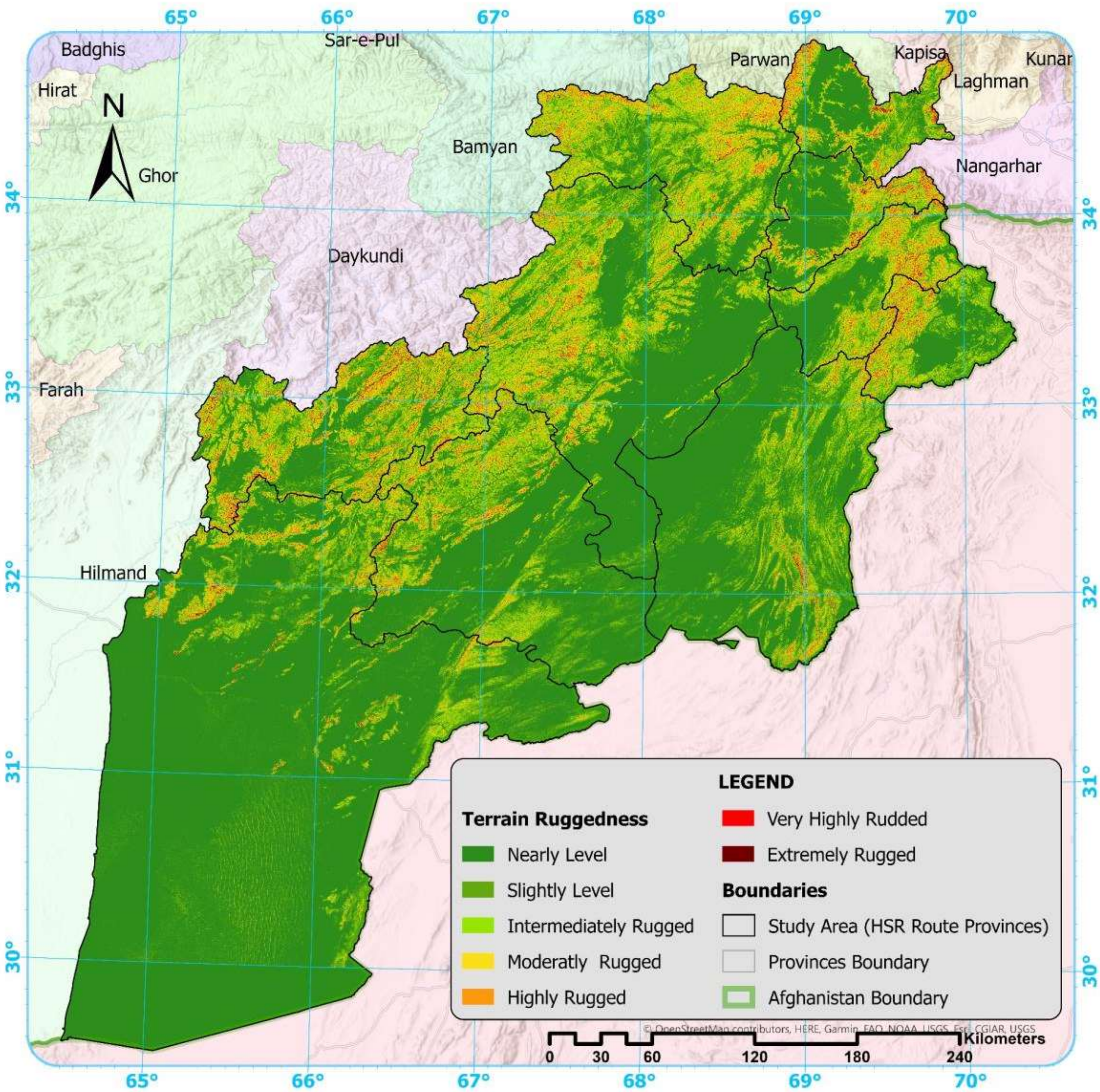


**Figure 4.27.** *The classified TRI map, considered in snow avalanche susceptibility analysis*

### *4.1.8.8. Temperature*

Temperature is a very important factor in forming wet snow avalanches (Choubin et al., 2020; Kumar et al., 2019; Mosavi et al., 2020; Varol, 2022; Yariyan et al., 2020). Regional warming after a snowfall mobilizes the snowpacks by reducing the bond between the snowpack and floor (Mosavi et al., 2020; Yariyan et al., 2020). Changes in temperature cause snowflakes to melt, which leads to weakening the upper layers of snow; consequently, the new cohesive snow layers forming after the snowfall over the weaker layers results in slab avalanches (Tiwari & Vishwakarma, 2021; Yariyan et al., 2020). The average temperatures for February over the years 2015 to 2020, was calculated in GEE API using the MOD11A2 V6 product (Wan, Hook, & Hulley, 2015); the results were downloaded for further processing in the ArcGIS Pro environment. The temperature layer was classified into seven classes considering the freezing degree and the critical variation of temperature over 0°C for avalanche triggering (Figure 4.28). These classes were rated based on their avalanche triggering potential (Table 4.5).

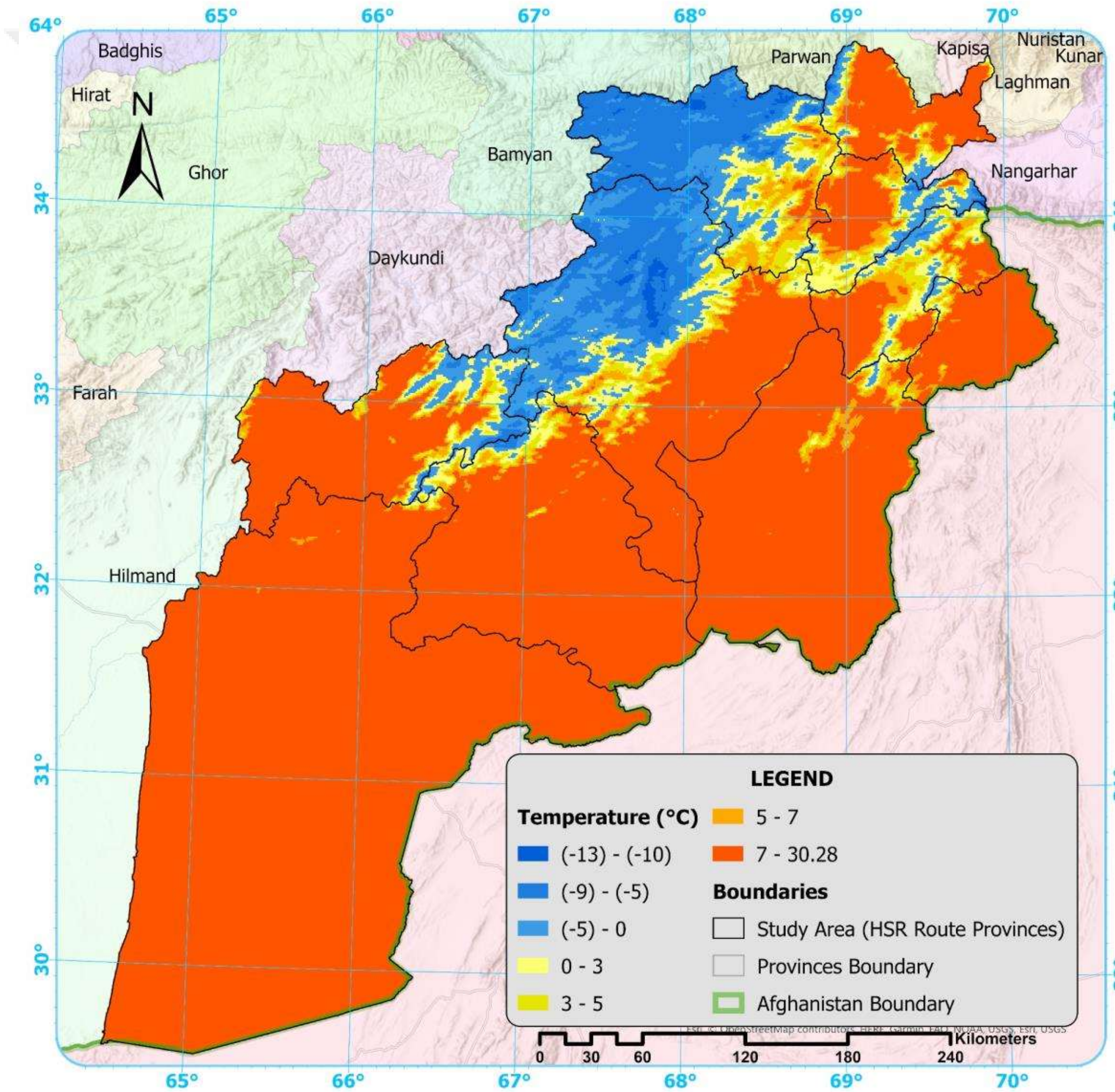


**Figure 4.28.** *The classified temperature map, considered in snow avalanche susceptibility analysis*

#### *4.1.8.9. Precipitation*

Precipitation is another important metrological factor with a significantly high influence in forming avalanches (Kumar et al., 2019; Rahmati et al., 2019; Sethia et al., 2018; Tiwari & Vishwakarma, 2021; Varol, 2022; Yariyan et al., 2020, 2021). The accumulation of new snow increases shear stress on weak layers and causes shear deformation that leads to slab avalanches (Choubin et al., 2020; Nasery & Kalkan, 2021; Rahmati et al., 2019; Tiwari & Vishwakarma, 2021; Yariyan et al., 2021). The frozen surface of the old snow can contribute to sliding the new snowpack and cause an avalanche (Yariyan et al., 2021).

The average precipitation for December to May over the years 2000 to 2005 and 2015 to 2020, was calculated in GEE API, and the results were downloaded for further processing in the ArcGIS Pro environment. The snowfall precipitation measurements are given in centimeters (cm) or millimeters (mm) of water equivalent; 10 cm equals 10 mm of water equivalent, and 1 cm/h equals to 1 mm/h of water equivalent (Perla & Martinelli, 2004). The snowstorm, which eventually causes snow avalanche, has three phases and has different perception intensities (Perla & Martinelli, 2004). The precipitation intensity for phases 1, 2, and 3 are 1.1 mm/h, 2.5 mm/h, and 0.6 mm/h, respectively. The precipitation layer was classified into six classes considering the water equivalent of the precipitation intensity and was rated based on their avalanche triggering potential (Table 4.5) (Figure 4.29).

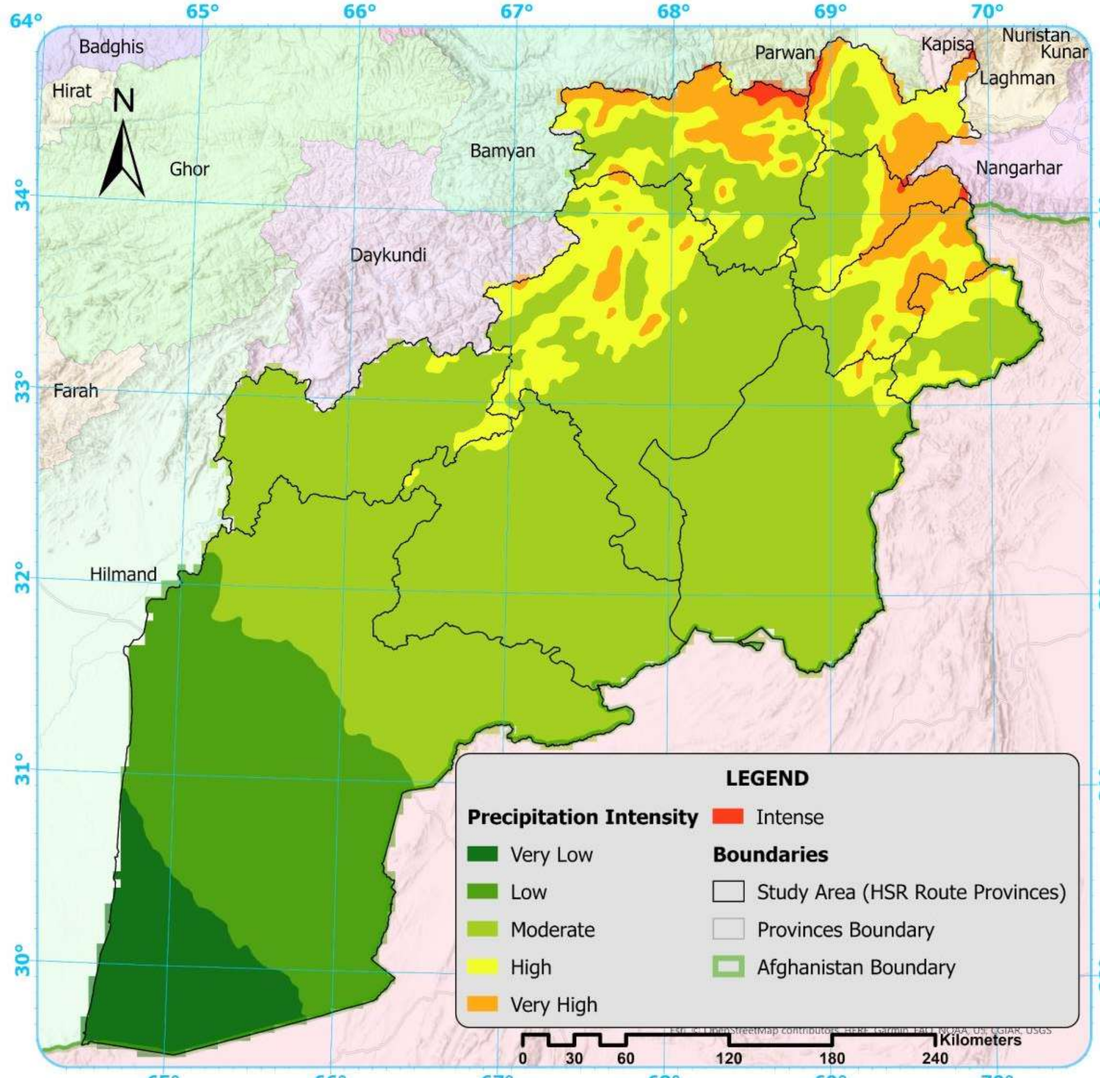


**Figure 4.29.** *The classified precipitation intensity, considered in snow avalanche susceptibility analysis*

#### *4.1.8.10. Wind exposition index*

Wind speed and direction have a very crucial role in snow avalanche susceptibility due to their ability to deposit snow on leeward sides and cause scouring on windward sides (Choubin et al., 2019; Rahmati et al., 2019; Tiwari & Vishwakarma, 2021; Yariyan et al., 2021). The high volume of the accumulated snow on leeward slopes can form avalanches (Rahmati et al., 2019; Yariyan et al., 2021). High winds form weak snowpacks and can trigger avalanches after new snowfall in the future (Tiwari & Vishwakarma, 2021). The snow drift peaks are mainly at a wind speed of about 20-25 meters per second (m/s) (Schweizer, Jamieson, & Schneebeli, 2003). The WEI estimates the wind effect on snow accumulation for all angular step-wise directions (Akay, 2021).

The WEI was calculated in SAGA-GIS; the output values below +1 corresponds to wind shadowed regions while values greater than +1 corresponds to regions exposed to wind. The WEI layer was classified into five classes and is rated accordingly (Table 4.5) (Figure 4.30).

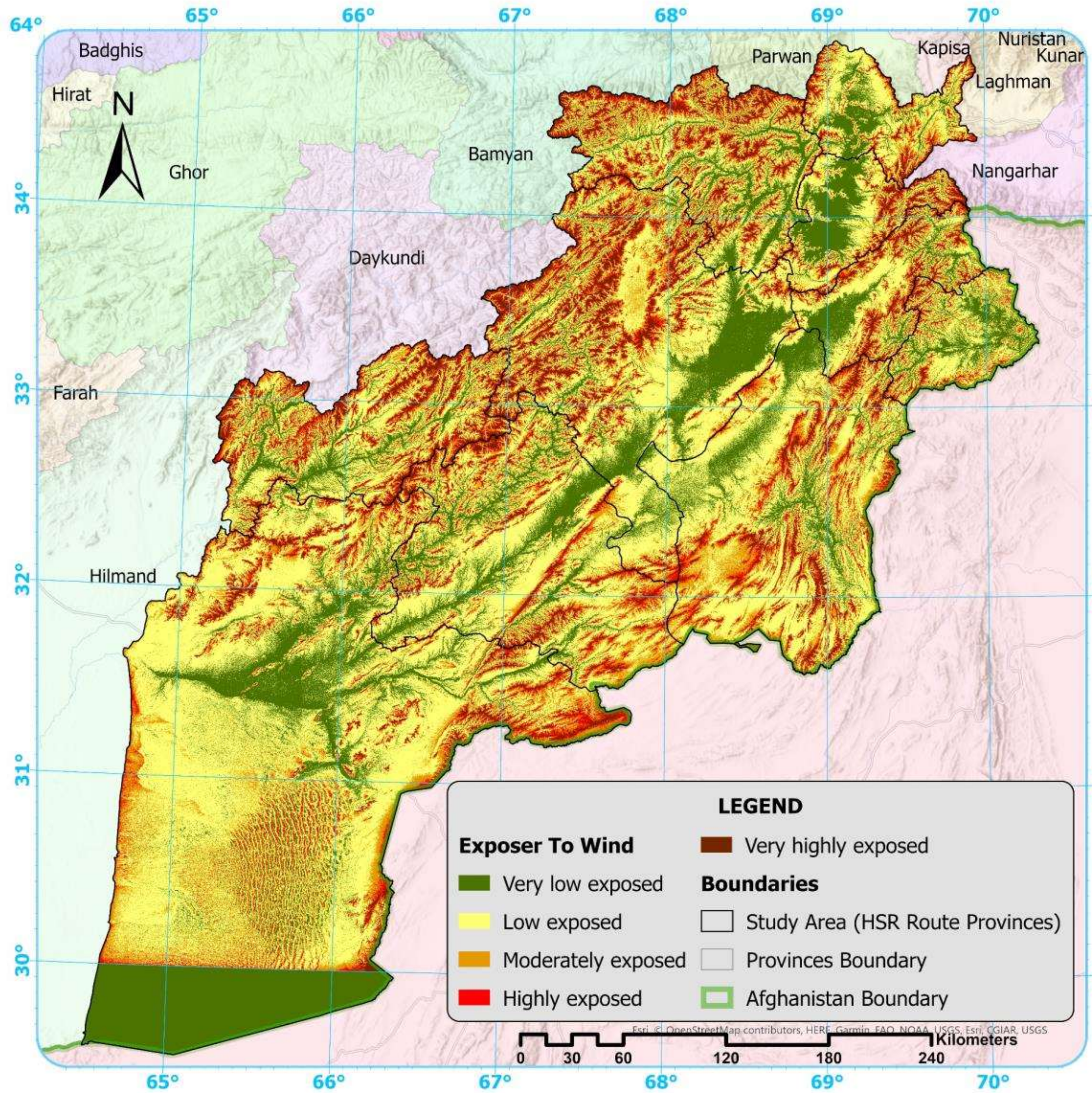


**Figure 4.30.** *The classified WEI map, considered in snow avalanche susceptibility analysis*

**Table 4.5.** *The most important factors in snow avalanche susceptibility, their subcategories, and their ratings*

| Factor/Criterion | Classes (sub-categories) | Ratings (%) |
|---|---|---|
| **Slope** | 0° - 12° | 1 |
| | 12° - 28° | 20 |
| | 28° - 35° | 95 |
| | 35° - 45° | 100 |
| | 45° - 55° | 30 |
| | >55° | 1 |
| **Aspect** | Flat (-1°) | 0 |
| | North (337.5°-0°-22.5°) | 100 |
| | Northeast (22.5°-67.5°) | 100 |
| | East (67.5°-112.5°) | 40 |
| | Southeast (112.5°-157.5°) | 25 |
| | South (157.5°-202.5°) | 25 |
| | Southwest (202.5°-247.5°) | 25 |
| | West (247.5°- 292.5°) | 40 |
| | Northwest (292.5°-337.5°) | 80 |
| **Elevation** | 790-2000 m | 0 |
| | 2000-2500 m | 10 |
| | 2500-3000 m | 35 |
| | 3000-3500 m | 60 |
| | 3500-3750 m | 80 |
| | 3750-4000 m | 95 |
| | 4000-5067 m | 100 |
| **Curvature** | Concave | 1 |
| | Flat | 20 |
| | Convex | 100 |
| **LULC** | Barren Lands | 100 |
| | Rangelands | 90 |
| | Irrigated Agricultural Lands | 25 |
| | Rainfed Agricultural Lands | 85 |
| | Fruit Trees | 10 |
| | Vineyards | 5 |
| | Forests and Shrubs | 40 |
| | Sand Cover | 0 |
| | Water Bodies and Marshlands | 0 |
| | Permanent Snow Cover | 100 |
| | Build Up Areas | 0 |

**Table 4.5.** *(continue) The most important factors in snow avalanche susceptibility, their subcategories, and their ratings*

| | | |
|---|---|---|
| **Length of Slope** | <50 m | 1 |
| | 50-100 m | 1 |
| | 100-200 m | 80 |
| | 200-400 m | 90 |
| | 400-600 m | 95 |
| | >600 m | 100 |
| **TRI** | Nearly Level (0-2.5) | 100 |
| | Slightly Level (2.5-5) | 90 |
| | Intermediately Rugged (5-7.5) | 80 |
| | Moderately Rugged (7.5-10) | 70 |
| | Highly Rugged (10-13.5) | 50 |
| | Very Highly Rugged (12.5-15) | 20 |
| | Extremely Rugged (15-1572) | 5 |
| **Temperature** | Very Low (-15) – (-10) °C | 50 |
| | Low (-10) – (-5) °C | 50 |
| | Moderate (-5) - 0 °C | 70 |
| | High (0 - 3 °C) | 100 |
| | Very High (3 - 5 °C) | 10 |
| | Extreme (5 - 30.28 °C) | 1 |
| **Precipitation** | Very low (<14.4 mm) | 1 |
| | Low (14.4-24.4 mm) | 10 |
| | Moderate (24.4-45 mm) | 70 |
| | High (45-60 mm) | 90 |
| | Very high (60-100 mm) | 100 |
| | Intense (>100 mm) | 100 |
| **WEI** | 0-1 | 1 |
| | 1-1.1 | 5 |
| | 1.1-1.15 | 50 |
| | 1.15-1.2 | 80 |
| | >1.2 | 100 |

### 4.1.9. Flood susceptibility

Floods are the most common destructive natural disasters occurring worldwide with severe impacts on people, properties, infrastructure, and the environment. Flood is the most dominant railway disaster globally, which can severely damage the route embankment (Hu, Bian, & Tan, 2020; Johnston, Murphy, & Holden, 2021). For example, in China it accounts for more than 70% of disasters (Wang et al., 2021; Zhao, Liu, & Wang, 2020). Among all-natural disasters, floods account for a roughly 47.2% share in terms of fatality and missing toll and 72.1% economic damage (Doorga et al., 2022). Global warming and climate change have caused a continuous increase in the frequency and intensity of flood disasters (Das & Gupta, 2021; Doorga et al., 2022; Luu et al., 2021; Malik et al., 2021; Stamellou et al., 2021; Tiryaki & Karaca, 2018). Heavy rainfall, snowmelt, or hydrological structures failure can cause floods (Darabi et al., 2021; Goumrasa et al., 2021; Shahiri Tabarestani & Afzalimehr, 2021; Stamellou et al., 2021; Stavropoulos et al., 2020), but floods are mainly triggered by heavy rainfall (Malik et al., 2021).

Flash flood is a serious concern due to its rapid formation and unpredictable locality compared to coastal and river flooding (Haque et al., 2021). Flash flood is a rapid rise of water along a stream or low-lying regions within a few hours caused by intense rainfall. Flash floods are more common in urban areas, but they are very frequent in dry areas. Flash floods have high velocity due to their steep watersheds that have the capacity to transport rocks, trees, cars and so on (Stavropoulos et al., 2020). Therefore, the focus of this study is on flash floods that can pose serious threats to HSR infrastructures. In recent decades, studying and monitoring flood disasters have been done by creating risk and hazard maps. There are three main geospatial flood analysis methods, statistical, hydrological, and MCDA (Doorga et al., 2022). Statistical methods depend on the historical flood database for predicting flood occurrence in the future; hydrological modeling methods are based on shallow water equations initialized by rainfall; and MCDA methods that determine flood susceptibility through processing multiple influential factors simultaneously (Doorga et al., 2022).

In this study, GIS and MCDA methods have been integrated for deriving flood susceptibility maps. The fuzzy-AHP method is used for weighing the factors. The general workflow of the study and data processing steps are shown in Figure 4.31.

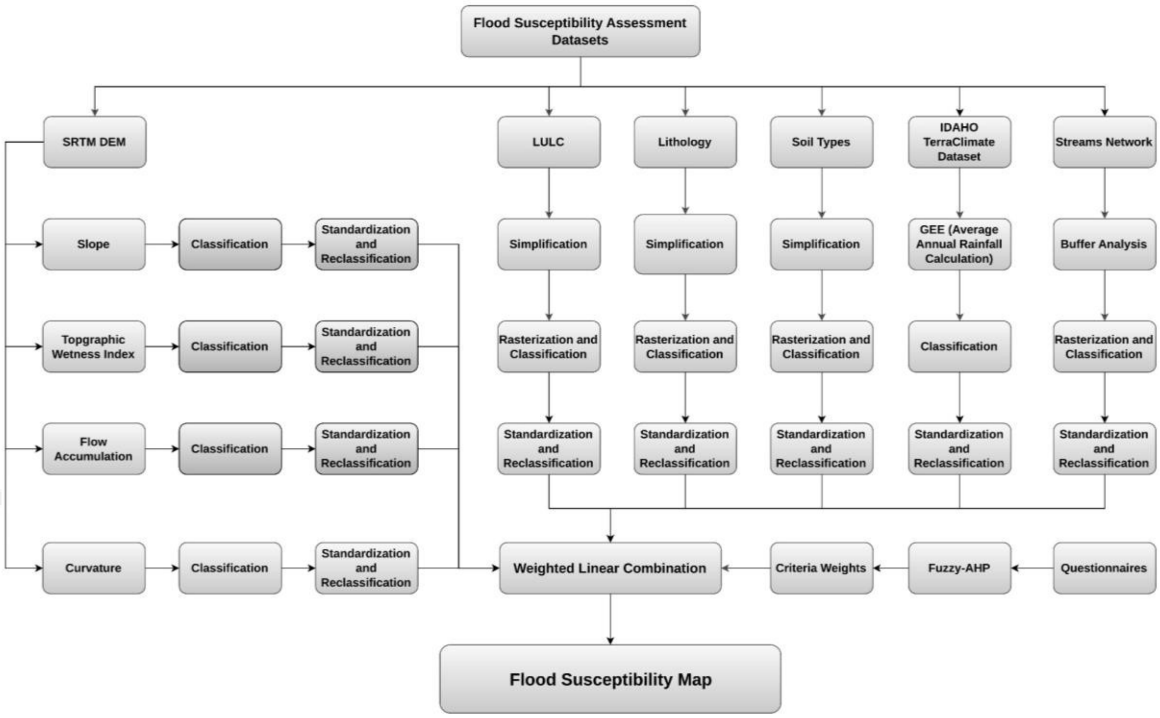


**Figure 4.31.** *The general workflow of the flood susceptibility assessment*

The most prominent factor in flood susceptibility has been identified through a detailed literature review. The following factors are considered in this study based on the geographical and climatological features of the study area: slope, flow accumulation, lithology, rainfall, LULC, soil types, distance to rivers, curvature, and TWI.

#### *4.1.9.1. Slope*

The surface slope strongly influences flood risk due to its direct relation with surface runoff velocity and water infiltration (Darabi et al., 2021; Doorga et al., 2022; Hamlat et al., 2021; Luu et al., 2021). The slope has an inverse relation with flood susceptibility; decreasing the watershed slope increases the flood risk and contrariwise (Das & Gupta, 2021; Sahu, Bose, & Samal, 2021; Shahiri Tabarestani & Afzalimehr, 2021). The slope factor was generated from the DEM layer and was classified into five classes (Figure 4.32) based on literature (Das & Gupta, 2021; Goumrasa, Guendouz, & Guettouche, 2021; Hamlat et al., 2021; Luu et al., 2021; Stavropoulos et al., 2020; Vojtek et al., 2021). After that, the reclassification process was carried out considering their corresponding ratings (Table 4.6).

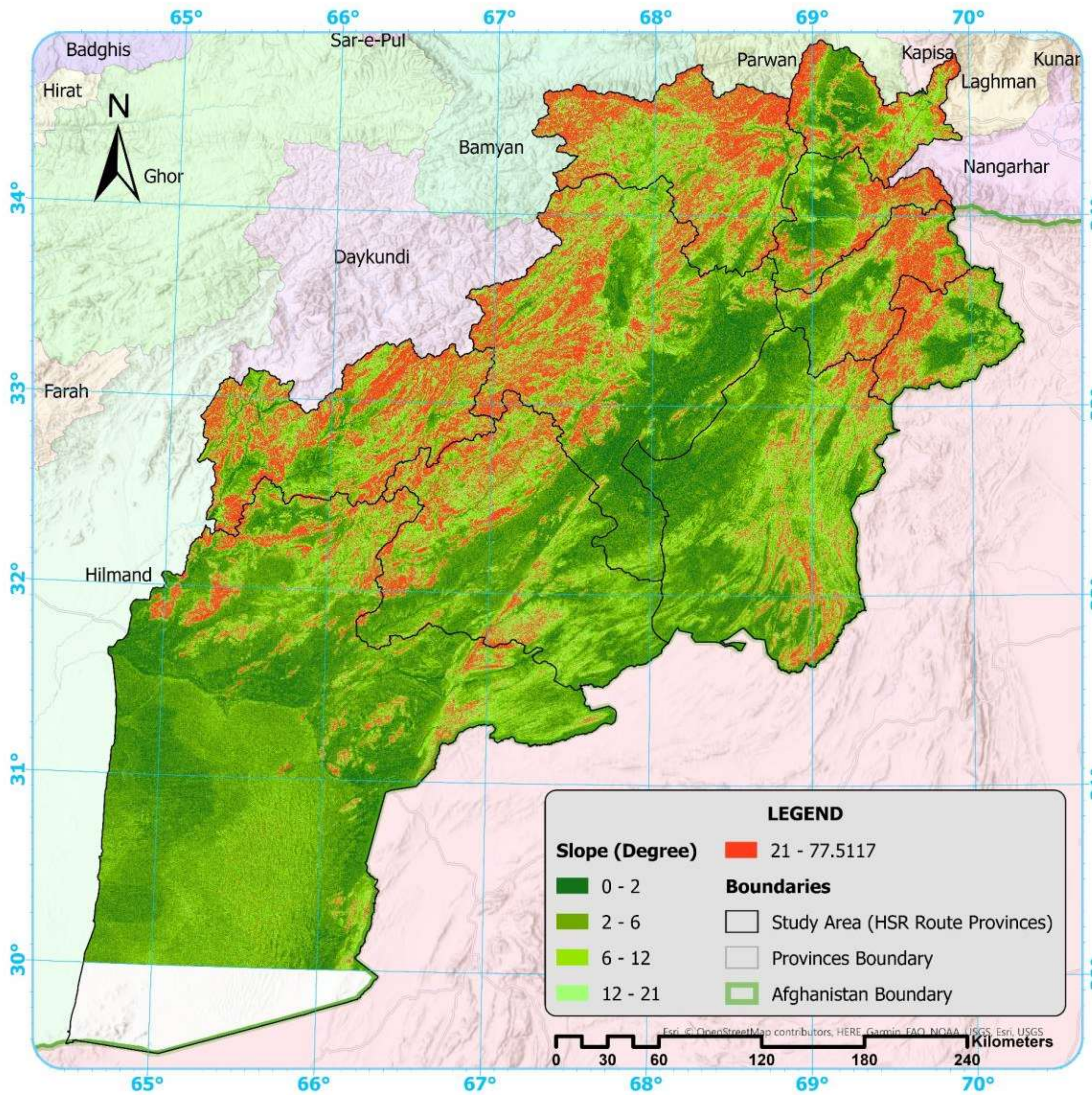


**Figure 4.32.** *The classified slope map, considered in flood susceptibility assessment*

#### *4.1.9.2. Flow accumulation*

Flow accumulation is the most important factor in flood susceptibility (Doorga et al., 2022; Goumrasa et al., 2021; Luu et al., 2021; Sahu, Bose, & Samal, 2021; Stamellou et al., 2021). Flow accumulation has a direct relation with drainage density and stream order in a region (Sahu, Bose, & Samal, 2021), thus controlling water concentration in different locations, consequently initiating high flood susceptibility. The existence of numerous flow accumulation paths in a river drainage basin feeding the main river can increase flood susceptibility by accumulating rainfall from a large catchment area (Doorga et al., 2022). Generally, areas located close to rivers and with high flow accumulation values are more prone to flood susceptibility (Goumrasa, Guendouz, & Guettouche, 2021; Hamlat et al., 2021). The flow accumulation layer was derived from the DEM dataset and was classified into 6 classes (Table 4.6) (Figure 4.33).

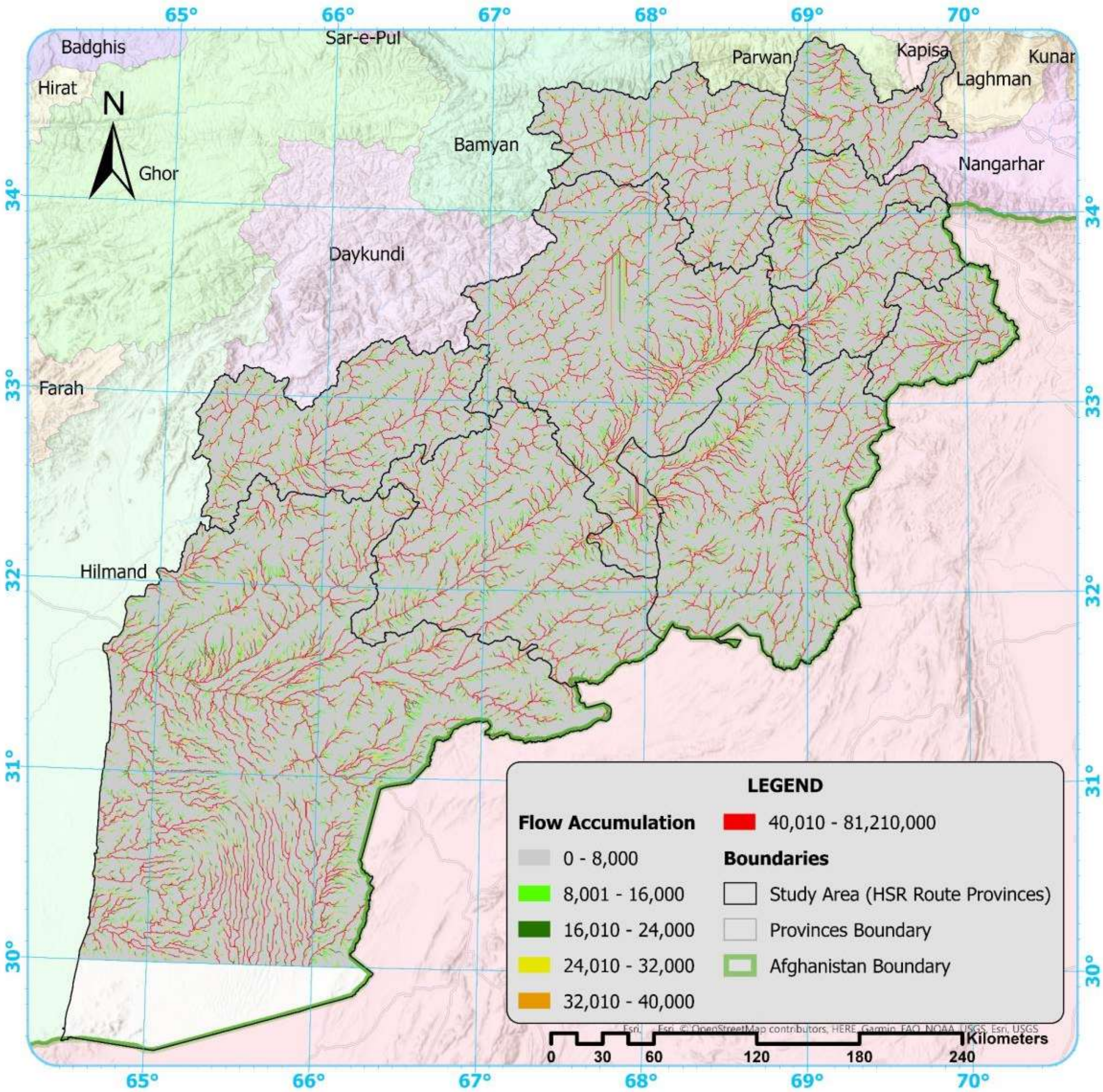


**Figure 4.33.** *The classified flow accumulation map, considered in flood susceptibility assessment*

### *4.1.9.3. Lithology*

Geological structures have a major influence on surface runoff and infiltration process through absorbing or conducting water, hence increasing flood susceptibility (Das & Gupta, 2021; Goumrasa et al., 2021; Luu et al., 2021; Shahiri Tabarestani & Afzalimehr, 2021). The infiltration process depends on the soil and rocks permeability and porosity. Among different lithological classes, sandstone has the highest permeability while granite and basalt have the lowest (Ku et al., 2009). The lithology layer was classified into 6 classes based on their permeability and the appropriate ratings were assigned to each class (Table 4.6) (Figure 4.15).

#### *4.1.9.4. Rainfall intensity*

Rainfall is the most important metrological factor leading to flooding disasters (Costache et al., 2020; Das & Gupta, 2021; Goumrasa et al., 2021; Hamlat et al., 2021; Malik et al., 2021). The intensity, occurrence rate, and intervals of rainfall define the spatial extent and severity of flood incidents (Goumrasa et al., 2021; Haque et al., 2021). The annual average daily rainfall data was generated from the GEE API. The TerraClimate dataset of IDAHO University in the GEE product library was used for deriving the precipitation data layer and statistics (Abatzoglou et al., 2018). The average rainfall for the rainfall session was calculated in two intervals from 2000 to 2005 and 2016 to 2021. The rainfall layer was classified into six classes, and the appropriate ratings were assigned to each class based on their potential in initiating flood disasters (Table 4.6) (Figure 4.16).

#### *4.1.9.5. Landuse/landcover*

By controlling the water infiltration rate by increasing surface runoff and reducing permeability, LULC is a vital factor for flood susceptibility assessment (Doorga et al., 2022; Goumrasa et al., 2021; Hamlat et al., 2021; Malik et al., 2021). The process of water infiltration and the progression of water to waterbodies can be performed much more efficiently in a dense vegetated surface cover than bare land (Haque et al., 2021). In contrast, urban areas and artificial structures such as roads, buildings, and concrete surfaces limit the absorbance capability of the soil, thus leading to spillover (Haque et al., 2021; Stavropoulos et al., 2020). The LULC map was classified into 11 classes that are rated based on water infiltration capability and flood susceptibility (Table 4.6) (Figure 4.3).

#### *4.1.9.6. Soil types*

Soil permeability also has a strong effect on rainwater infiltration and soil moisture (Doorga et al., 2022; Shahiri Tabarestani & Afzalimehr, 2021). The type of soil determines the surface runoff properties and contributes to flood occurrence (Malik et al., 2021). Permeable soil infiltrates rainwater, thus decreasing flood risk, while impermeable rocks increase surface runoff, thus increasing flood probability (Doorga et al., 2022). The soil types map of the study area is shown in Figure 4.5.

#### *4.1.9.7. Distance from rivers*

The flood susceptibility is very high in regions near discharge channel networks due to the water spillover after intense rainfall (Das & Gupta, 2021; Doorga et al., 2022). The study area is categorized into 6 groups considering the distance from rivers factor, and appropriate ratings were assigned to each group (Table 4.6) (Figure 4.34).

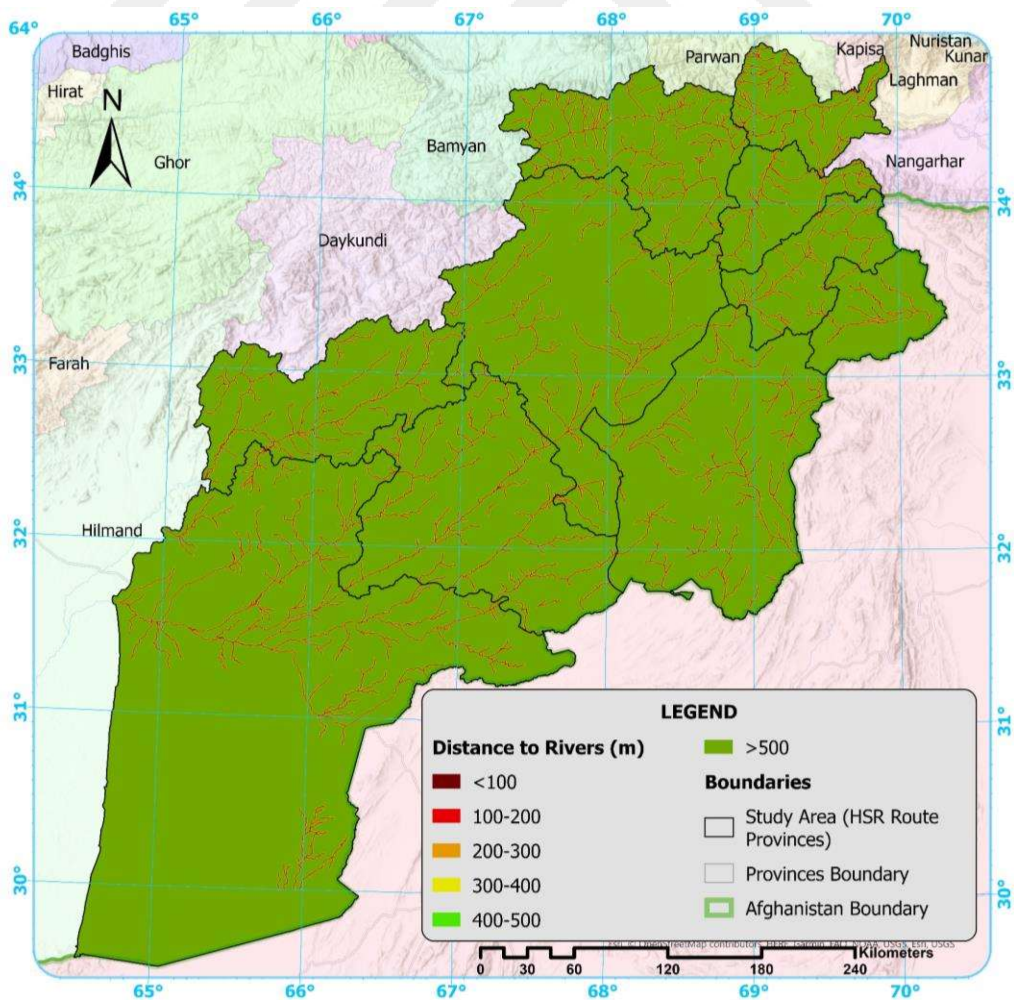


**Figure 4.34.** *The classified distances to rivers, considered in flood susceptibility assessment*

#### *4.1.9.8. Curvature*

Surface curvature has an essential role in surface water flow. Concave and flat surfaces tend to hold water for a long period, thus slowing the water flow, and the surface runoff would be lower, while convex surfaces have a higher surface runoff potential (Doorga et al., 2022; Malik et al., 2021). The study area was classified into concave, flat, and convex classes, and proper rates were assigned to them, considering their influence on surface runoff and water flow potential (Table 4.6) (Figure 4.25).

#### *4.1.9.9. Topographic wetness index*

The TWI depicts the accumulation of water at any specific catchment area, which corresponds to flood inundation (Das & Gupta, 2021; Goumrasa et al., 2021). The TWI map was classified into 6 classes (Table 4.6). The classified TWI map of the area is shown in Figure 4.21.

**Table 4.6.** *The most prominent factors in flood susceptibility, their subcategories, and their ratings*

| Factor/Criterion | Classes (sub-categories) | Ratings (%) |
|---|---|---|
| **Slope** | 0° - 2° | 100 |
| | 2° - 6° | 80 |
| | 6° - 12° | 50 |
| | 12° - 21° | 5 |
| | >21° | 1 |
| **Flow Accumulation** | <8000 | 1 |
| | 8000-16000 | 5 |
| | 16000-24000 | 20 |
| | 24000-32000 | 50 |
| | 32000-40000 | 80 |
| | >40000 | 100 |
| **Lithology** | Carbonatic Rocks | 10 |
| | Gneiss, Schist, Quartzite | 20 |
| | Granites | 60 |
| | Surficial Deposits | 100 |
| | Ultramafic Rocks | 80 |
| | Volcanic Rocks | 90 |
| | Water Bodies | 100 |
| **Annual Average Rainfall** | Micro rain (0-12 mm) | 1 |

**Table 4.6.** *(continue) The most prominent factors in flood susceptibility, their subcategories, and ratings*

| | | |
|---|---|---|
| | Light rain (12-30 mm) | 5 |
| | Moderate rain (30-80 mm) | 50 |
| | Heavy rain (80-100 mm) | 90 |
| | Very heavy rain (100-180 mm) | 100 |
| | Torrential rain (>180 mm) | 100 |
| **LULC** | Barren Lands | 95 |
| | Rangelands | 100 |
| | Irrigated Agricultural Lands | 30 |
| | Rainfed Agricultural Lands | 50 |
| | Fruit Trees | 25 |
| | Vineyards | 25 |
| | Forests and Shrubs | 20 |
| | Sand Cover | 0 |
| | Water Bodies and Marshlands | 100 |
| | Permanent Snow Cover | 0 |
| | Build Up Areas | 95 |
| **Soil Types** | Silty Clay | 95 |
| | Sandy Clay | 70 |
| | Clayey Gravel | 50 |
| | Sand | 10 |
| | Silty Gravel | 85 |
| | Rocks | 30 |
| | Water Bodies | 100 |
| **Distance to Rivers** | <100 m | 100 |
| | 100-200 m | 90 |
| | 200-300 m | 80 |
| | 300-400 m | 70 |
| | 400-500 m | 60 |
| | >500 m | 20 |
| **Curvature** | Concave | 5 |
| | Flat | 40 |
| | Convex | 100 |
| **TWI** | 0-2 | 5 |
| | 2-6 | 20 |
| | 6-10 | 40 |
| | 10-14 | 70 |
| | 14-18 | 90 |
| | >18 | 100 |

#### 4.1.10. Distance from faultlines

Intensive earthquakes are generally close to faultlines, but local conditions, magnitude, and depth of earthquakes are the intensifying dynamics as well (Byers, 2004). The damage mechanism of the earthquake on railroads is mainly in the form of surface displacement across faultlines and can directly damage the rail routes that cross the faultline (Byers, 2004). Seismic waves can cause displacement of bridge pairs and permanent ground displacements through the liquefication nature of the soil that can lead to derailment (Byers, 2004; Lakušić et al., 2020; Xiao, Ling, & Jin, 2012). Earthquake is a major disaster that severely damages the railway's infrastructure with up to 1.2 billion US dollars in worth annually (Zhu et al., n.d.). The 11 March 2011 earthquake in Japan damaged concrete structures of Shinkansen HSR and affected 27 high-speed trains on the line (Janic, 2015). The earthquake has resulted in several serious derailment accidents throughout the short history of HSR. For example, a Shinkansen train was derailed in 2004 Niigata earthquake in Japan, derailment accident caused by the Jiashian earthquake in Taiwan, another Shinkansen bullet train derailed during the Kumamoto earthquake; also seven trains were derailed during the Tangshan earthquake (Cao, Yang, & Zhang, 2020; Jin et al., 2016, 2020; Xiao, Ling, & Jin, 2012; Zeng & Dimitrakopoulos, 2018). Lateral earthquake motion is more significant for a train to run safely compared to vertical earthquake motion; it has a dominant relationship with the risk of derailment (Jin et al., 2016; Xiao, Ling, & Jin, 2012). The railway track's sensitivity to the earthquake directly relates to the track bed soil attributes (Lakušić et al., 2020). Modern HSR tracks are mostly installed on bridges that can exceed 50% of their total length; therefore, the derailment on bridges is a major concern (Jin et al., 2016; Zeng & Dimitrakopoulos, 2018). Most importantly, ballasted track which is the most common type of track model adopted in HSR systems, can become loose and experience lateral displacement during an earthquake and lead to derailment (Cao, Yang, & Zhang, 2020; Lakušić et al., 2020). Subsequently, constructing an HSR line within a safe distance from faultlines could reduce the risk of derailment by earthquakes and can significantly reduce the project cost by decreasing the need for adopting very sensitive rail track systems and HSR wheels. The faultlines map of the study area is shown in Figure 4.35.

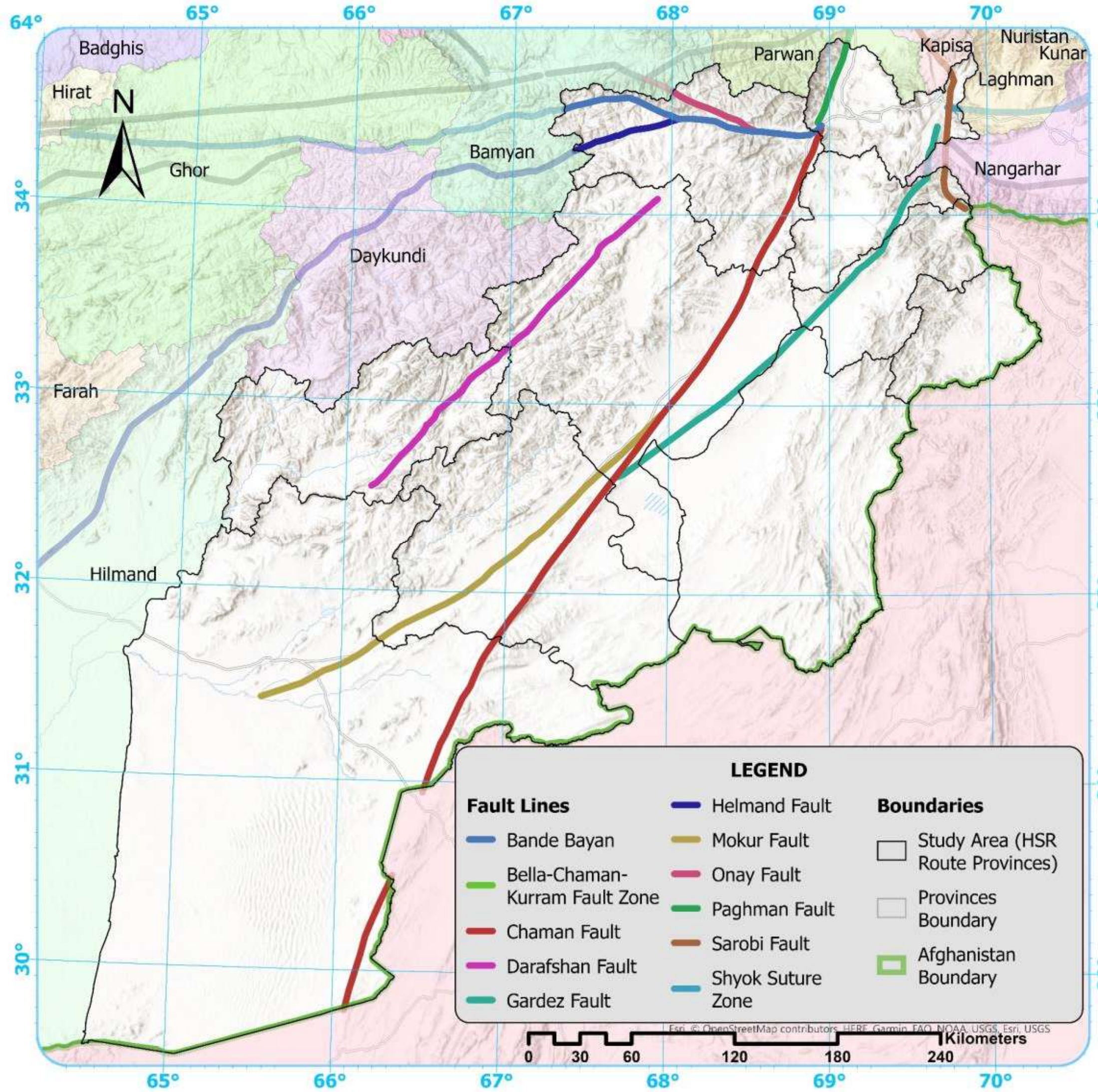


**Figure 4.35.** *The major active faultlines of the study area*

In this study, the distances from faultlines are defined into six classes considering literature to limit the HSR route intersection, maintain a feasible safe distance from faultlines, and minimize the risk of derailment (Figure 4.36). The buffer zones were created at intervals of 200 m from the faultlines and appropriate ratings were assigned to them based on the optimality perspective (Table 4.3).

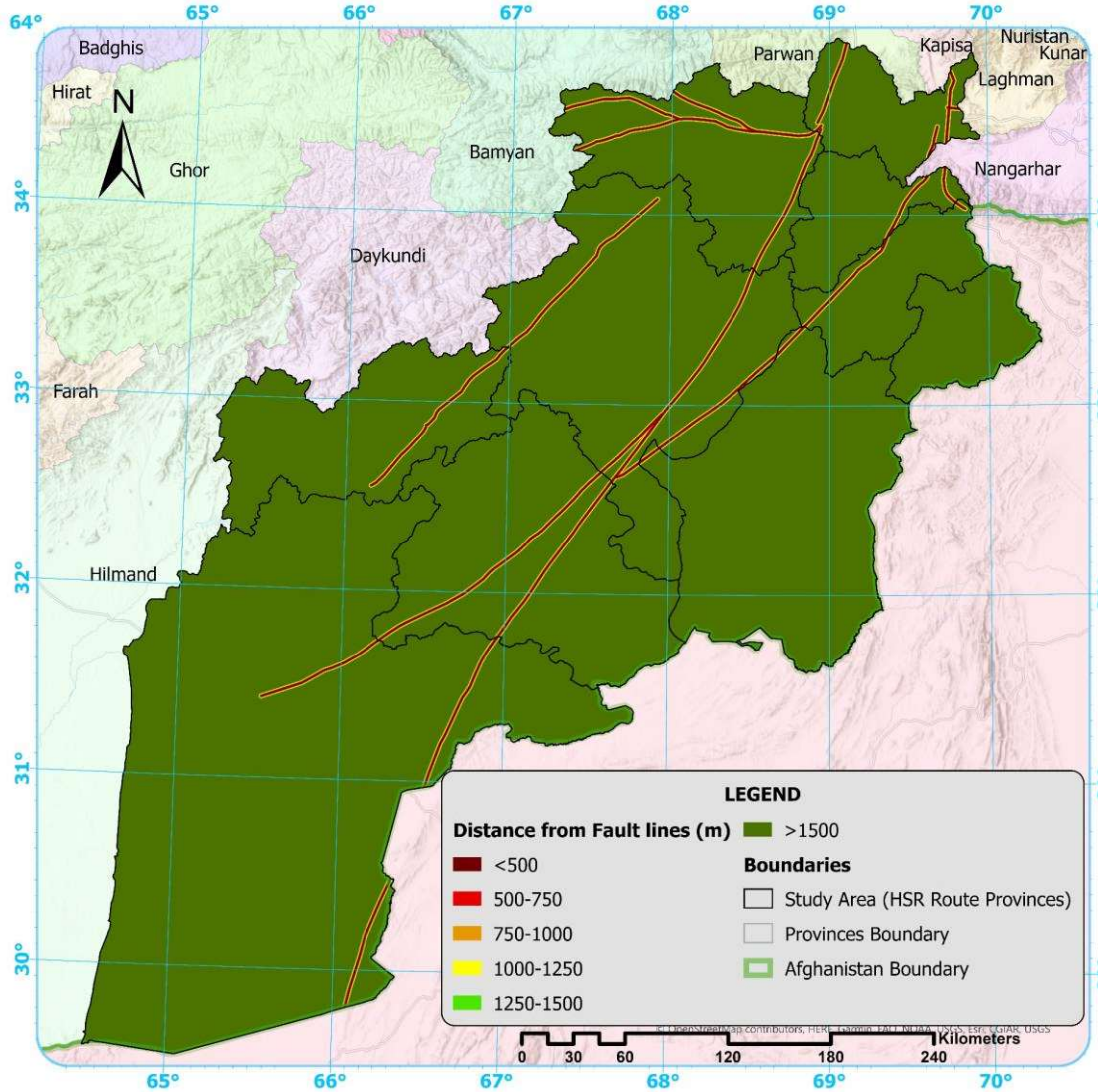


**Figure 4.36.** *The classified buffer distances from faultlines, considered in the HSR route location assessment*

### 4.1.11. Historical sites and protected areas

Preservation of historical places gives people a glimpse of a country's rich culture, social structure, political strategy, and military strength in the past. Historical sites are irreplaceable structures that convoy the cultural heritage value of a nation. These sites are generally protected by the law in most countries (Ivanic et al., 2020).

International Union for Conservation of Nature (IUCN) defines a protected area as: A protected area is a clearly defined geographical space, recognized, dedicated and managed, through legal or other effective means, to achieve the long term conservation of nature with associated ecosystem services and cultural values (Ivanic et al., 2020).

Protected areas have great importance in protecting the species that are being lost at a shocking rate and critical habitats for these species; furthermore, destroying protected areas unbalances the ecosystems, which can cause the spreading of infectious diseases as human and wildlife are coming closer (Ivanic et al., 2020). Most importantly, many of the earth's habitats store additional greenhouse gases like carbon; clearing these habitats makes us more vulnerable to the tragic effect of climate change (Ivanic et al., 2020).

The data for the historical and protected areas were not obtained despite contacting the ARCHAÏOS head office. The archeological map of Afghanistan is shown in Figure 4.37. The historical and protected areas are not included in the processing due to the lack of data.

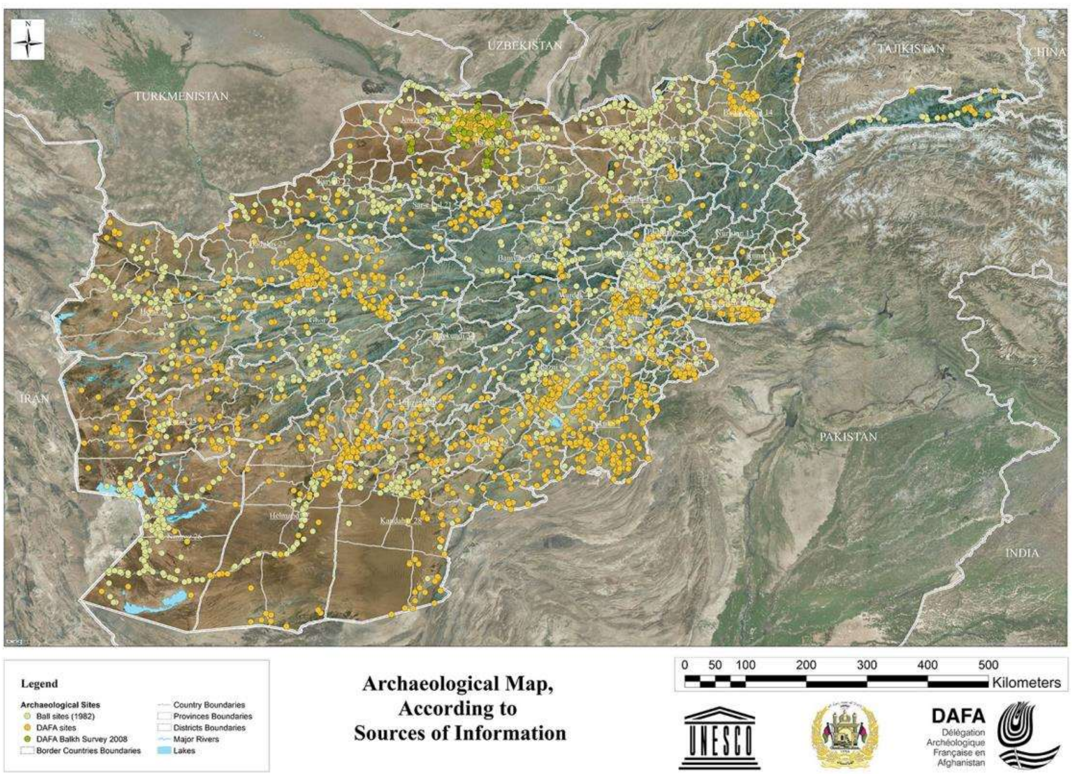


**Figure 4.37.** *The historical and protected areas map of the study area (https://www.archaios.fr)*

# 5. RESULTS

In the chapter, the results for HSR route location selection and landslide, snow avalanche, and flood susceptibility mapping are presented in separate sections. A short discussion has been made for landslide, avalanche, and flood maps, while a comprehensive discussion is presented for the HSR route in the following chapter.

## 5.1. Landslide Susceptibility

Landslides are devastative natural disasters that bring severe damage to transportation structures. Landslides are highly probable in regions with steep slopes, weak geological formations, and intense precipitation. The landslide susceptibility is considered an influential factor in selecting the optimal HSR route in the current study. The various landslide triggering and conditional factors considered in this study were slope, aspect, lithology, rainfall precipitation, LULC, distance to faults, distance to roads, distance to streams, NDVI, and TWI. The importance of the factors was determined based on the questionaries performed by hydrology and geology experts and their weights were calculated by adopting the fuzzy-AHP method; the calculations for deriving weights of the criteria can be found in Appendix A. The results showed that slope and lithology are the most dominant factors in landslide occurrence. The resulting weights for each factor are given in Figure 5.1. The landslide susceptibility analysis was performed in ArcGIS Pro software.

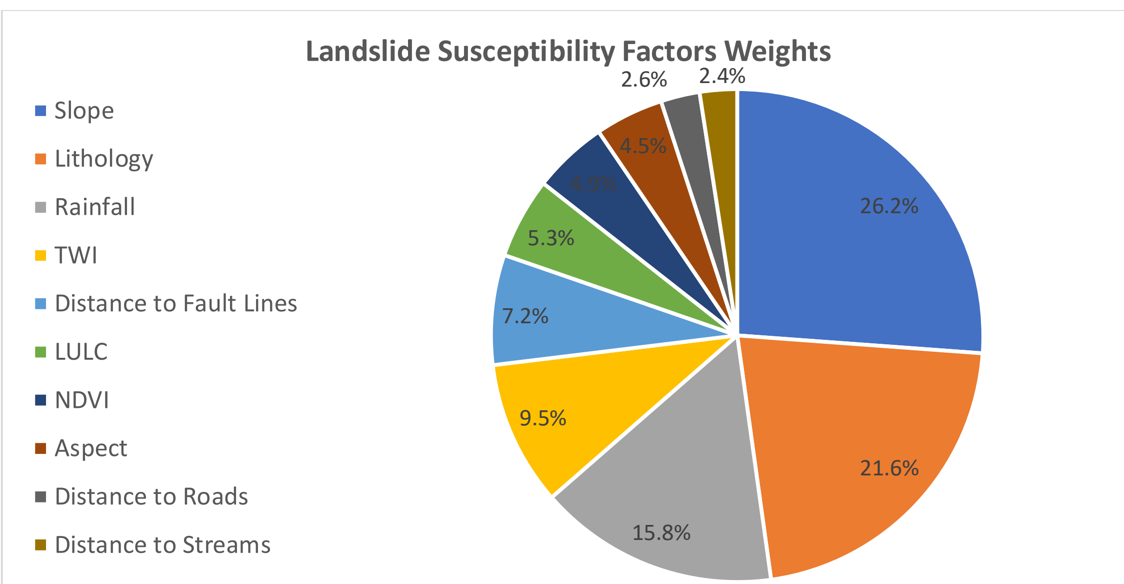


**Figure 5.1.** *The calculated weights of the factors effective in landslide susceptibility*

The resulted landslide susceptibility map was classified into the following five classes based on their susceptibility level: very low, low, moderate, high, and very high (Figure 5.2). The very highly susceptible areas cover 0.7% of the study area, while 40.7% is covered by the very low class (Table 5.1).

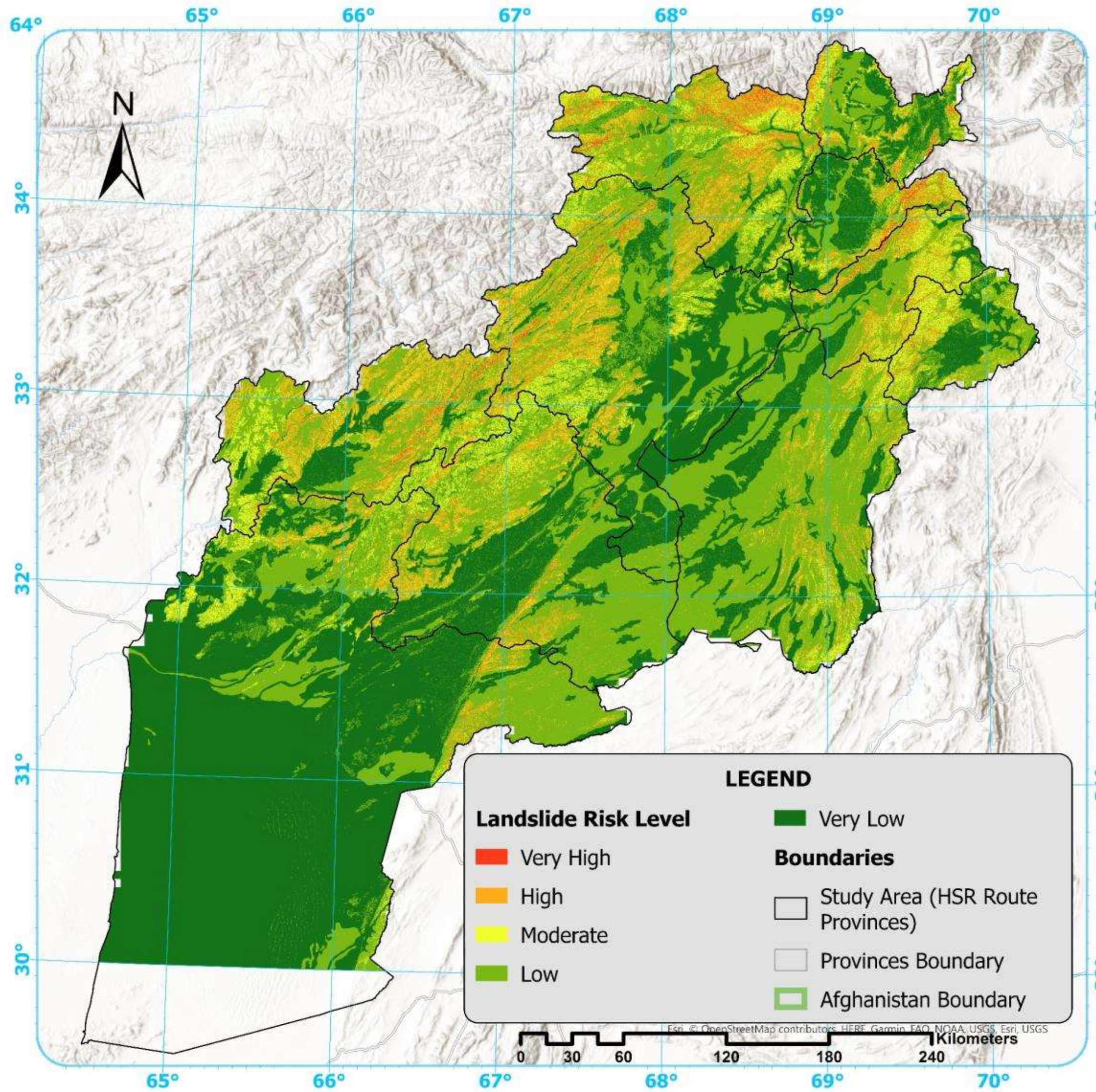


**Figure 5.2.** *The classified landslide susceptibility map of the study area*

**Table 5.1.** *The distribution of landslide susceptibility classes in the study area*

| Landslide Susceptibility | Area (km$^2$) | Percentage (%) |
|---|---|---|
| **Very High** | 58853.46 | 0.7 |
| **High** | 62077.79 | 7.7 |
| **Moderate** | 11536.94 | 8.0 |
| **Low** | 11178.71 | 42.9 |
| **Very Low** | 946.67 | 40.7 |

## 5.2. Snow Avalanche Susceptibility

Snow avalanches pose a superior risk to humans, properties, and infrastructures in the winter season each year. Snow avalanches are considered a deadly natural disaster that can demolish a wide area on their track due to the presence of debris containing rocks, with the snow mass. Snow avalanches are more likely to happen in regions with intense snowfall, low temperature, and steep slopes. In this study, snow avalanche is considered a factor in ascertaining the best optimal HSR route. The influential static and dynamic factors in snow avalanche triggering and formation considered in this study are slope, elevation, aspect, curvature, LULC, length of the slope, TRI, temperature, precipitation, and WEI. A questionary form was prepared, and experts were asked to assess the relative importance of each factor concerning snow avalanche risk in the area. The fuzzy-AHP method was applied for determining the weights of the factors; Appendix A presents the calculations made for deriving weights of the factors. The results indicate that slope, precipitation, and temperature are the most influential factors in snow avalanche formation and triggering. The calculated weights for each factor are given in Figure 5.3.

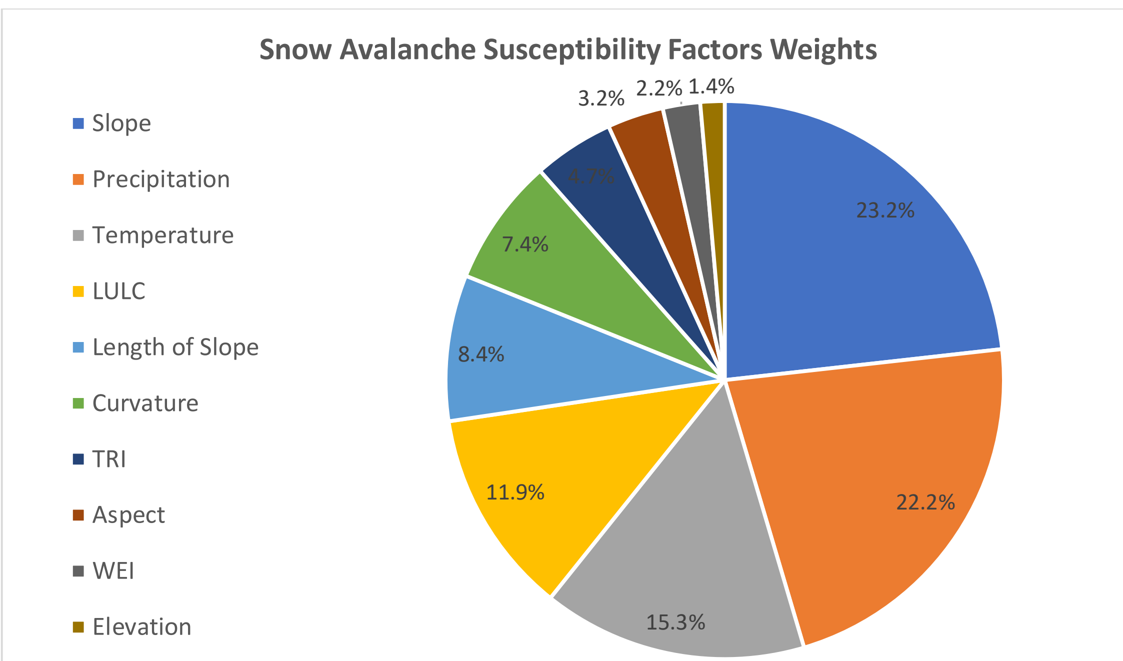


**Figure 5.3.** *The calculated weights of the factors effective in snow avalanche susceptibility*

The data processing for snow avalanche susceptibility assessment was performed in ArcGIS Pro software. The snow avalanche susceptibility map was classified into very low, low, moderate, high, and very high classes that are presented in Figure 5.4. According to the results, only 0.9% of the study area is susceptible to very high avalanches, although 69.8% have a high susceptibility; the distribution of avalanche susceptibility classes in the study area is shown in Table 5.2.

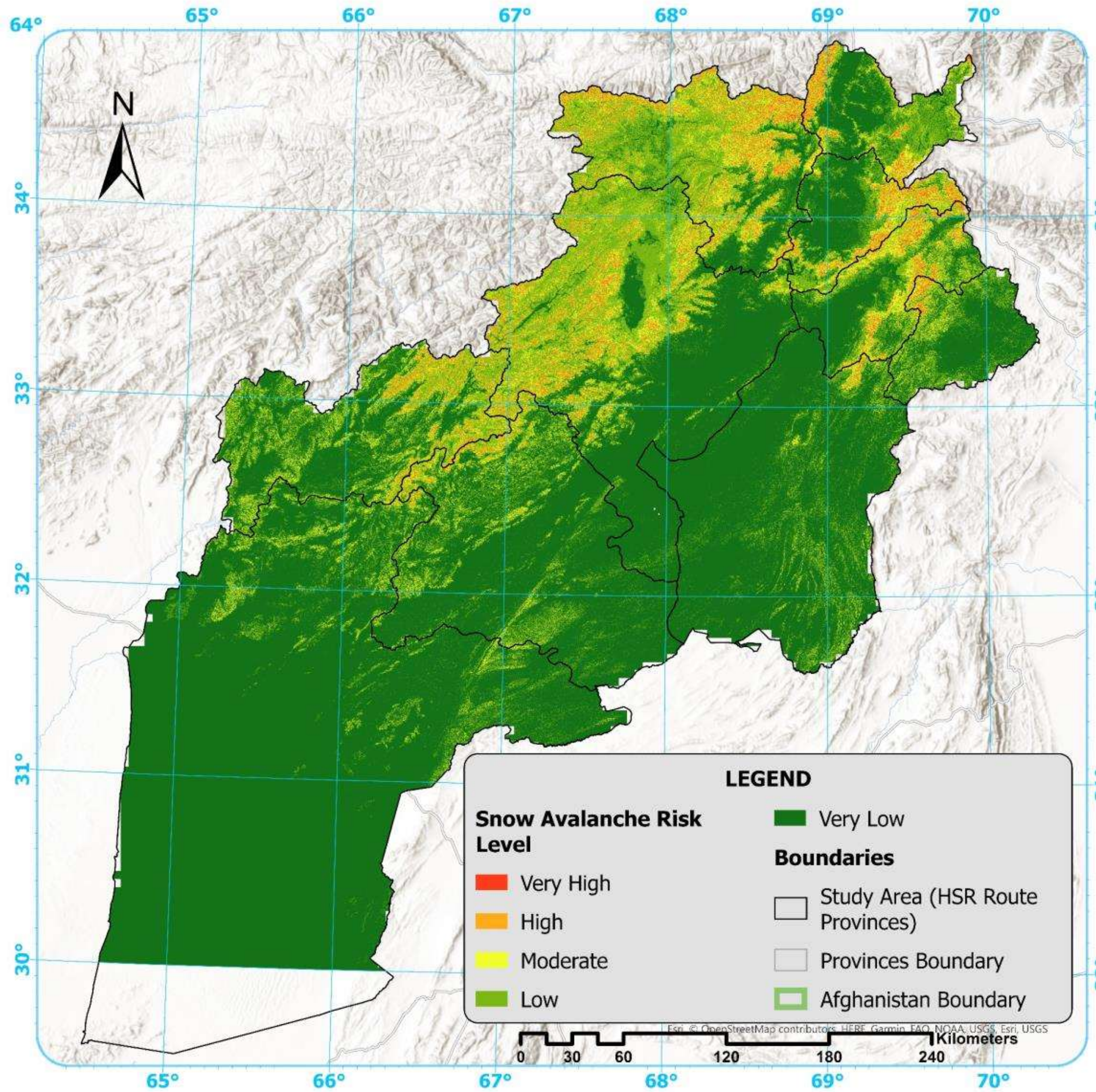


**Figure 5.4.** *The classified snow avalanche susceptibility map of the study area*

**Table 5.2.** *The distribution of snow avalanche susceptibility classes in the study area*

| Snow Avalanche Susceptibility | Area (km$^2$) | Percentage (%) |
|---|---|---|
| **Very High** | 100953.27 | 0.9 |
| **High** | 28408.31 | 2.7 |
| **Moderate** | 9939.27 | 6.9 |
| **Low** | 3932.99 | 19.7 |
| **Very Low** | 1359.81 | 69.8 |

## 5.3. Flood Susceptibility

Floods are the most dominant natural disasters worldwide, which brings the highest number of fatalities and heavy economic losses compared to other natural disasters. Floods can severely damage transportation networks, especially HSR route embankments which could lead to derailment and operation disruption. Intensive rainfall and low permeability of soil is the main cause of floods. The flood risk map is generated to be used as a constrain for HSR route locational assessment. Several factors can contribute to flooding in different geographical locations; the most prominent factors in flood susceptibility in the study area are as follow: slope, flow accumulation, lithology, rainfall, LULC, soil types, distance to rivers, curvature, and TWI. The fuzzy-AHP method is used for flood risk assessment; therefore, the expert's opinions were collected by questionaries to define the relative importance of the factors; the calculated weights are presented in Figure 5.5. The ArcGIS Pro product was used for data processing and generating the flood susceptibility map.

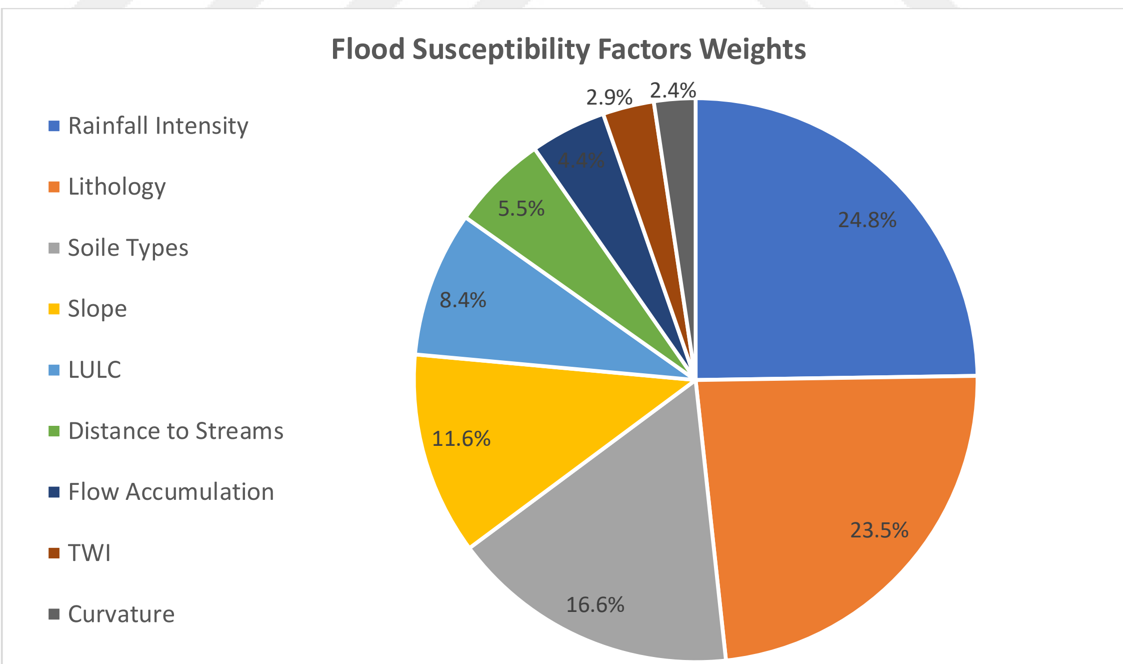


**Figure 5.5.** *The calculated weights of the factors effective in flood susceptibility*

The resulted flood susceptibility map was classified into the following five classes based on their susceptibility level: very low, low, moderate, high, and very high (Figure

5.6). The very highly susceptible areas cover 1.2% of the study area, while 20.8% is covered by the very low class (Table 5.3).

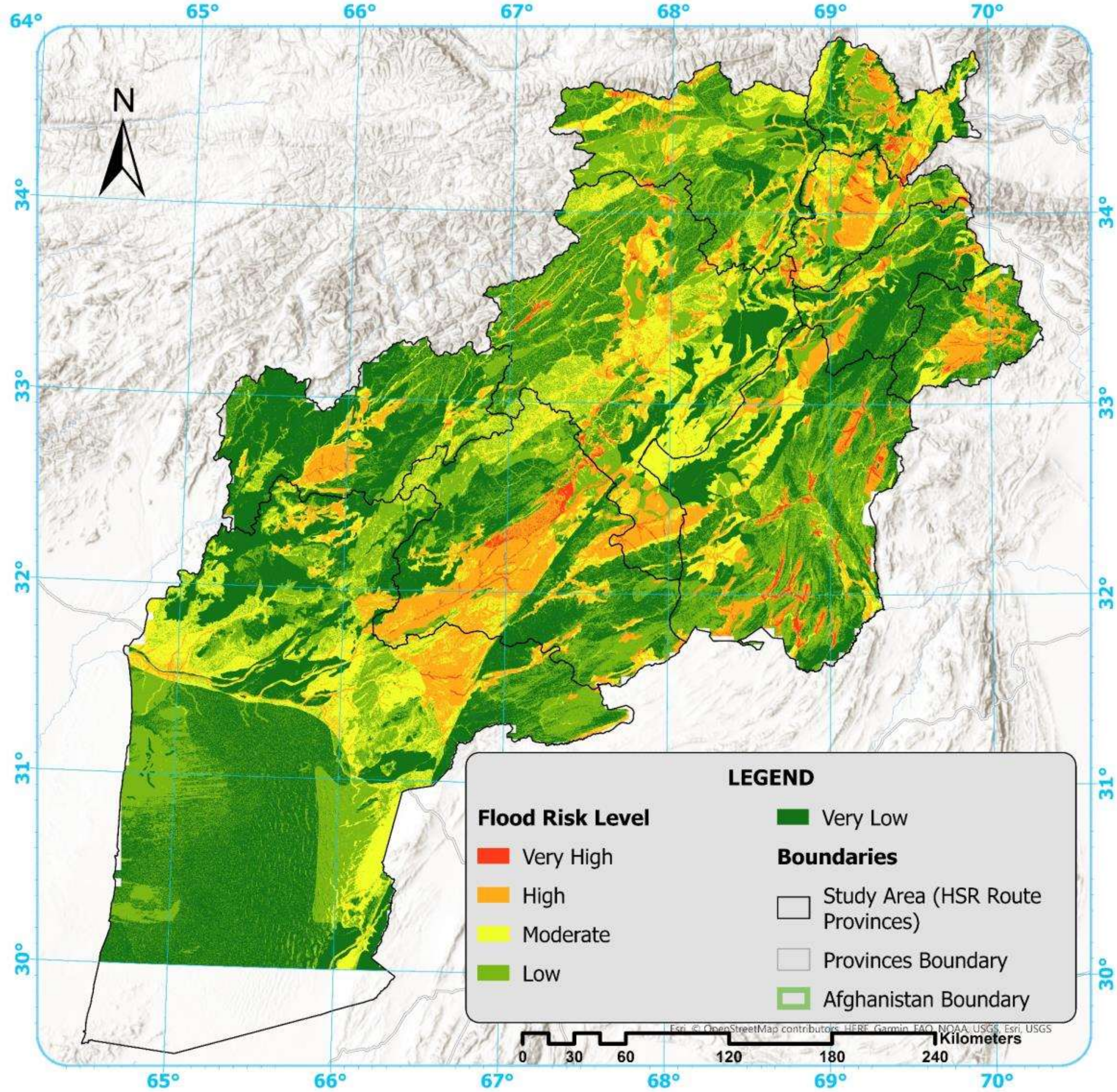


**Figure 5.6.** *The classified flood susceptibility map of the study area*

**Table 5.3.** *The distribution of flood susceptibility classes in the study area*

| Flood Susceptibility | Area (km$^2$) | Percentage (%) |
|---|---|---|
| **Very High** | 30074.74 | 1.2 |
| **High** | 71064.50 | 12.1 |
| **Moderate** | 24288.61 | 16.8 |
| **Low** | 17437.68 | 49.1 |
| **Very Low** | 1728.12 | 20.8 |

## 5.4. The Optimal HSR Route

In this study, a GIS-based MCDA method was adopted to generate the optimal HSR route between Kabul and Kandahar cities in Afghanistan. In addition, remotes sensing technology and data were also used in the HSR route assessment. The most significant factors affecting the HSR route alignment geographical location, economic feasibility, and the routes' geometry were determined through a comprehensive literature review and consultation with transportation sector experts. The factors considered in the HSR route assessment process in this study are as follows: slope, LULC, soil types, distance from rivers, proximity to roads, proximity to towns/cities, landslide susceptibility, snow avalanche susceptibility, flood susceptibility, and distance from faultlines. The AHP and fuzzy-AHP MCDA methods were used for determining the relative importance of the factors based on the expert's opinions collected through questionaries. These two methods are used at the same time to see the behavior of the LCP tool to the slightly different weights, thus showing the sensitivity of the model. The calculations for deriving the weights of the criteria were performed in both AHP and fuzzy-AHP methods and were used for generating the HSR route suitability maps. The AHP and fuzzy-AHP route alternatives were similar to each other in almost all places; these routes had insignificant differences in three locations with the lengths of 3 km, 2.5km, and 1.4km, respectively. Therefore, only the fuzzy-AHP route is presented as the optimal HSR route. The calculation for the fuzzy-AHP method is presented in Tables 5.4 and 5.5. The calculations for the AHP method are presented in Tables 5.6, 5.7, 5.8, and 5.9.

**Table 5.4.** *The fuzzified pairwise comparison matrix for the HSR route selection problem*

| Criteria/Criteria | Slope | | | LULC | | | Flood Risk | | | Distance To Rivers | | | Proximity To Roads | | | Proximity To Towns/Cities | | | Soil Types | | | Landslide Risk | | | Avalanche Risk | | | Distance to Fault Lines | | |
|---|---|---|---|---|---|---|---|---|---|---|---|---|---|---|---|---|---|---|---|---|---|---|---|---|---|---|---|---|---|---|
| **Slope** | 1 | 1 | 1 | 2 | 3 | 4 | 3 | 4 | 5 | 6 | 7 | 8 | 7 | 8 | 9 | 1 | 2 | 3 | 1 | 2 | 3 | 3 | 4 | 5 | 3 | 4 | 5 | 4 | 5 | 6 |
| **LULC** | 1/4 | 1/3 | 1/2 | 1 | 1 | 1 | 1/3 | 1/2 | 1 | 2 | 3 | 4 | 4 | 5 | 6 | 1/3 | 1/2 | 1 | 1/3 | 1/2 | 1 | 1 | 2 | 3 | 1 | 2 | 3 | 2 | 3 | 4 |
| **Flood risk** | 1/5 | 1/4 | 1/3 | 1 | 2 | 3 | 1 | 1 | 1 | 2 | 3 | 4 | 4 | 5 | 6 | 1/3 | 1/2 | 1 | 1/3 | 1/2 | 1 | 1/3 | 1/2 | 1 | 1/3 | 1/2 | 1 | 1 | 2 | 3 |
| **Distance to Rivers** | 1/8 | 1/7 | 1/6 | 1/4 | 1/3 | 1/2 | 1/4 | 1/3 | 1/2 | 1 | 1 | 1 | 1 | 2 | 3 | 1/6 | 1/5 | 1/4 | 1/6 | 1/5 | 1/4 | 1/4 | 1/3 | 1/2 | 1/4 | 1/3 | 1/2 | 1/3 | 1/2 | 1 |
| **Proximity to Roads** | 1/9 | 1/8 | 1/7 | 1/6 | 1/5 | 1/4 | 1/6 | 1/5 | 1/4 | 1/3 | 1/2 | 1 | 1 | 1 | 1 | 1/6 | 1/5 | 1/4 | 1/6 | 1/5 | 1/4 | 1/4 | 1/3 | 1/2 | 1/4 | 1/3 | 1/2 | 1/3 | 1/2 | 1 |
| **Population density** | 1/3 | 1/2 | 1 | 1 | 2 | 3 | 1 | 2 | 3 | 4 | 5 | 6 | 4 | 5 | 6 | 1 | 1 | 1 | 1 | 1 | 2 | 1 | 2 | 3 | 1 | 2 | 3 | 2 | 3 | 4 |
| **Geology** | 1/3 | 1/2 | 1 | 1 | 2 | 3 | 1 | 2 | 3 | 4 | 5 | 6 | 4 | 5 | 6 | 1/2 | 1 | 1 | 1 | 1 | 1 | 1 | 2 | 3 | 1 | 2 | 3 | 2 | 3 | 4 |
| **Landslide risk** | 1/5 | 1/4 | 1/3 | 1/3 | 1/2 | 1 | 1 | 2 | 3 | 2 | 3 | 4 | 2 | 3 | 4 | 1/3 | 1/2 | 1 | 1/3 | 1/2 | 1 | 1 | 1 | 1 | 1 | 1 | 2 | 1 | 2 | 3 |
| **Snow Avalanche risk** | 1/5 | 1/4 | 1/3 | 1/3 | 1/2 | 1 | 1 | 2 | 3 | 2 | 3 | 4 | 2 | 3 | 4 | 1/3 | 1/2 | 1 | 1/3 | 1/2 | 1 | 1/2 | 1 | 1 | 1 | 1 | 1 | 1 | 2 | 3 |
| **Dsitance to fault lines** | 1/6 | 1/5 | 1/4 | 1/4 | 1/3 | 1/2 | 1/3 | 1/2 | 1 | 1 | 2 | 3 | 1 | 2 | 3 | 1/4 | 1/3 | 1/2 | 1/4 | 1/3 | 1/2 | 1/3 | 1/2 | 1 | 1/3 | 1/2 | 1 | 1 | 1 | 1 |

**Table 5.5.** *The process of obtaining normalized weights by calculating the fuzzy geometric mean and fuzzy weights*

| Fuzzy Geometric mean value *ri* | | | Fuzzy Weights | | | Weights | Normalized Weights |
|---|---|---|---|---|---|---|---|
| **2 1/2** | **3 2/5** | **4 1/4** | 0.29 | 0.27 | 0.24 | 0.26 | 0.264 |
| **5/6** | **1 2/9** | **1 5/6** | 0.09 | 0.10 | 0.10 | 0.10 | 0.098 |
| **2/3** | **1** | **1 1/2** | 0.08 | 0.08 | 0.09 | 0.08 | 0.081 |
| **2/7** | **3/8** | **1/2** | 0.03 | 0.03 | 0.03 | 0.03 | 0.031 |
| **1/4** | **2/7** | **2/5** | 0.03 | 0.02 | 0.02 | 0.02 | 0.025 |
| **1 1/4** | **1 8/9** | **2 3/4** | 0.15 | 0.15 | 0.15 | 0.15 | 0.149 |
| **1 1/5** | **1 8/9** | **2 5/9** | 0.14 | 0.15 | 0.14 | 0.14 | 0.143 |
| **5/7** | **1** | **1 4/7** | 0.08 | 0.08 | 0.09 | 0.08 | 0.083 |
| **2/3** | **1** | **1 1/2** | 0.08 | 0.08 | 0.08 | 0.08 | 0.079 |
| **2/5** | **4/7** | **7/8** | 0.05 | 0.04 | 0.05 | 0.05 | 0.047 |

**Table 5.6.** *The AHP pairwise comparison matrix for the HSR route selection problem*

| Criteria/Criteria | Slope | Landuse/ Landcover | Flood risk | Proximity to Rivers | Proximity to Roads | Populatio n density | Geology | Landslide risk | Snow Avalanche risk | Proximity to fault lines |
|---|---|---|---|---|---|---|---|---|---|---|
| **Slope** | 1 | 3 | 4 | 7 | 8 | 2 | 2 | 4 | 4 | 5 |
| **Land Use/Land Cover** | 1/3 | 1 | 1/2 | 3 | 5 | 1/2 | 1/2 | 2 | 2 | 3 |
| **Flood risk** | 1/4 | 2 | 1 | 3 | 5 | 1/2 | 1/2 | 1/2 | 1/2 | 2 |
| **Proximity to Rivers** | 1/7 | 1/3 | 1/3 | 1 | 2 | 1/5 | 1/5 | 1/3 | 1/3 | 1/2 |
| **Proximity to Roads** | 1/8 | 1/5 | 1/5 | 1/2 | 1 | 1/5 | 1/5 | 1/3 | 1/3 | 1/2 |
| **Population density** | 1/2 | 2 | 2 | 5 | 5 | 1 | 1 | 2 | 2 | 3 |
| **Geology** | 1/2 | 2 | 2 | 5 | 5 | 1 | 1 | 2 | 2 | 3 |
| **Landslide risk** | 1/4 | 1/2 | 2 | 3 | 3 | 1/2 | 1/2 | 1 | 1 | 2 |
| **Snow Avalanche risk** | 1/4 | 1/2 | 2 | 3 | 3 | 1/2 | 1/2 | 1 | 1 | 2 |
| **Proximity to fault lines** | 1/5 | 1/3 | 1/2 | 2 | 2 | 1/3 | 1/3 | 1/2 | 1/2 | 1 |

**Table 5.7.** *The normalized pairwise comparison matrix of the AHP method for the HSR route selection problem*

| Criteria/Criteria | Slope | Landuse/ Landcover | Flood risk | Proximity to Rivers | Proximity to Roads | Population density | Geology | Landslide risk | Snow Avalanche risk | Proximity to fault lines |
|---|---|---|---|---|---|---|---|---|---|---|
| Slope | 0.282 | 0.253 | 0.275 | 0.215 | 0.205 | 0.297 | 0.297 | 0.293 | 0.293 | 0.227 |
| Land Use/Land Cover | 0.094 | 0.084 | 0.034 | 0.092 | 0.128 | 0.074 | 0.074 | 0.146 | 0.146 | 0.136 |
| Flood risk | 0.070 | 0.169 | 0.069 | 0.092 | 0.128 | 0.074 | 0.074 | 0.037 | 0.037 | 0.091 |
| Proximity to Rivers | 0.040 | 0.028 | 0.023 | 0.031 | 0.051 | 0.030 | 0.030 | 0.024 | 0.024 | 0.023 |
| Proximity to Roads | 0.035 | 0.017 | 0.014 | 0.015 | 0.026 | 0.030 | 0.030 | 0.024 | 0.024 | 0.023 |
| Population density | 0.141 | 0.169 | 0.138 | 0.154 | 0.128 | 0.149 | 0.149 | 0.146 | 0.146 | 0.136 |
| Geology | 0.141 | 0.169 | 0.138 | 0.154 | 0.128 | 0.149 | 0.149 | 0.146 | 0.146 | 0.136 |
| Landslide risk | 0.070 | 0.042 | 0.138 | 0.092 | 0.077 | 0.074 | 0.074 | 0.073 | 0.073 | 0.091 |
| Snow Avalanche risk | 0.070 | 0.042 | 0.138 | 0.092 | 0.077 | 0.074 | 0.074 | 0.073 | 0.073 | 0.091 |
| Proximity to fault lines | 0.056 | 0.028 | 0.034 | 0.062 | 0.051 | 0.050 | 0.050 | 0.037 | 0.037 | 0.045 |

**Table 5.8.** *The consistency index and consistency ratio calculation matrix*

| Criteria/Criteria | Slope | Landuse/ Landcover | Flood risk | Proximity to Rivers | Proximity to Roads | Population density | Geology | Landslide risk | Snow Avalanche risk | Proximity to fault lines |
|---|---|---|---|---|---|---|---|---|---|---|
| Slope | 0.264 | 0.303 | 0.336 | 0.213 | 0.190 | 0.291 | 0.291 | 0.322 | 0.322 | 0.225 |
| Land Use/Land Cover | 0.088 | 0.101 | 0.042 | 0.091 | 0.119 | 0.073 | 0.073 | 0.161 | 0.161 | 0.135 |
| Flood risk | 0.066 | 0.202 | 0.084 | 0.091 | 0.119 | 0.073 | 0.073 | 0.040 | 0.040 | 0.090 |
| Proximity to Rivers | 0.038 | 0.034 | 0.028 | 0.030 | 0.048 | 0.029 | 0.029 | 0.027 | 0.027 | 0.022 |
| Proximity to Roads | 0.033 | 0.020 | 0.017 | 0.015 | 0.024 | 0.029 | 0.029 | 0.027 | 0.027 | 0.022 |
| Population density | 0.132 | 0.202 | 0.168 | 0.152 | 0.119 | 0.146 | 0.146 | 0.161 | 0.161 | 0.135 |
| Geology | 0.132 | 0.202 | 0.168 | 0.152 | 0.119 | 0.146 | 0.146 | 0.161 | 0.161 | 0.135 |
| Landslide risk | 0.066 | 0.051 | 0.168 | 0.091 | 0.071 | 0.073 | 0.073 | 0.081 | 0.081 | 0.090 |
| Snow Avalanche risk | 0.066 | 0.051 | 0.168 | 0.091 | 0.071 | 0.073 | 0.073 | 0.081 | 0.081 | 0.090 |
| Proximity to fault lines | 0.053 | 0.034 | 0.042 | 0.061 | 0.048 | 0.049 | 0.049 | 0.040 | 0.040 | 0.045 |

**Table 5.9.** *The calculated principal eigenvalue, consistency index, and consistency ratio of the AHP method*

| ʎmax | RI | CI | CR |
|---|---|---|---|
| 10.4 | 1.49 | 0.042 | 0.028 |

The results showed that the AHP and fuzzy-AHP weights have small differences which were not very significant in HSR route location. The results indicated that slope and proximity to towns/cities are the most important factors in HSR routing; the AHP and fuzzy-AHP weights are presented in Figure 5.7.

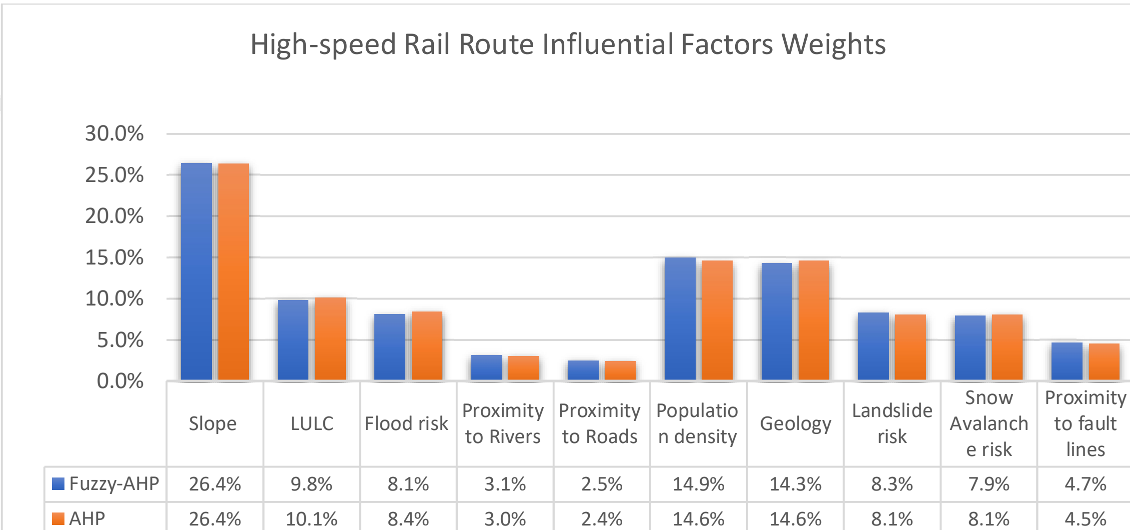


**Figure 5.7.** *The calculated weights of the influential factors in HSR route selection*

The data processing tasks were carried out in the ArcGIS Pro and SAGA-GIS software environments and GEE API. The data layers were combined using the raster calculator tool in ArcGIS Pro software, considering their weights to generate the HSR route suitability map (Figure 5.8). This map was classified into six classes of very highly, highly, moderately, low, and very low suitable; the distribution of the suitability classes is presented in Table 5.10.

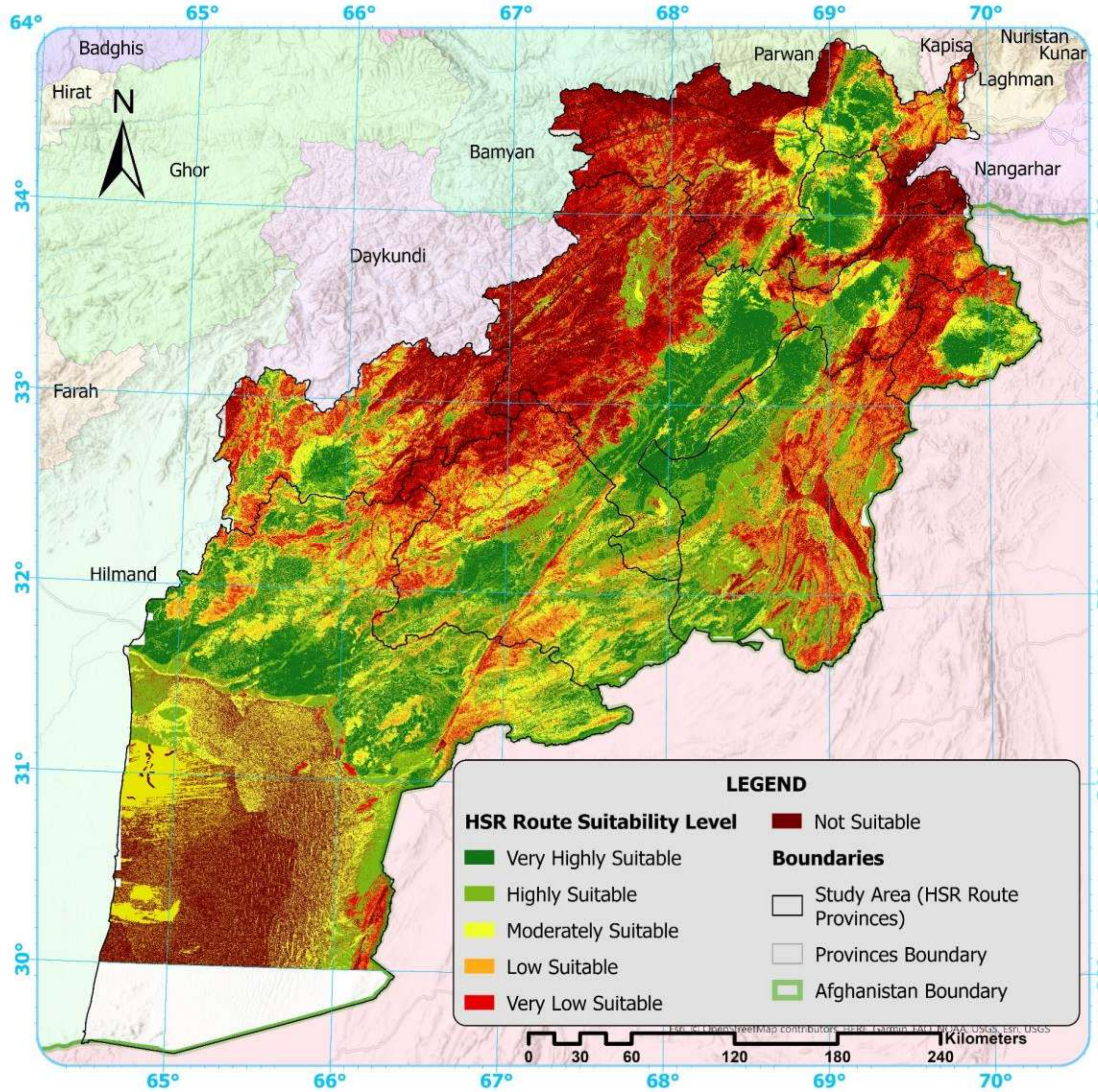


**Figure 5.8.** *The classified suitability map of the study area for the HSR route*

**Table 5.10.** *The distribution of the HSR route alignment location suitability classes in the study area*

| Suitability Level | Area (km$^2$) | Percentage (%) |
|---|---|---|
| **Very Highly Suitable** | 25086.46 | 17.3 |
| **Highly Suitable** | 20653.30 | 14.3 |
| **Moderately Suitable** | 23225.26 | 16.1 |
| **Low Suitable** | 20529.13 | 14.2 |
| **Very Low Suitable** | 22792.75 | 15.8 |
| **Not Suitable** | 32306.74 | 22.3 |

The HSR route alignment was determined as a result of the LCPA performed in the ArcGIS Pro software environment by employing the LCP tool; The LCP tool has generated the shortest optimal route automatically considering the suitability map/layer.

The resulted route alignment is converted to polyline feature (vector format) and a line smoothing was performed to eliminate its sharp edges (Figure 5.9).

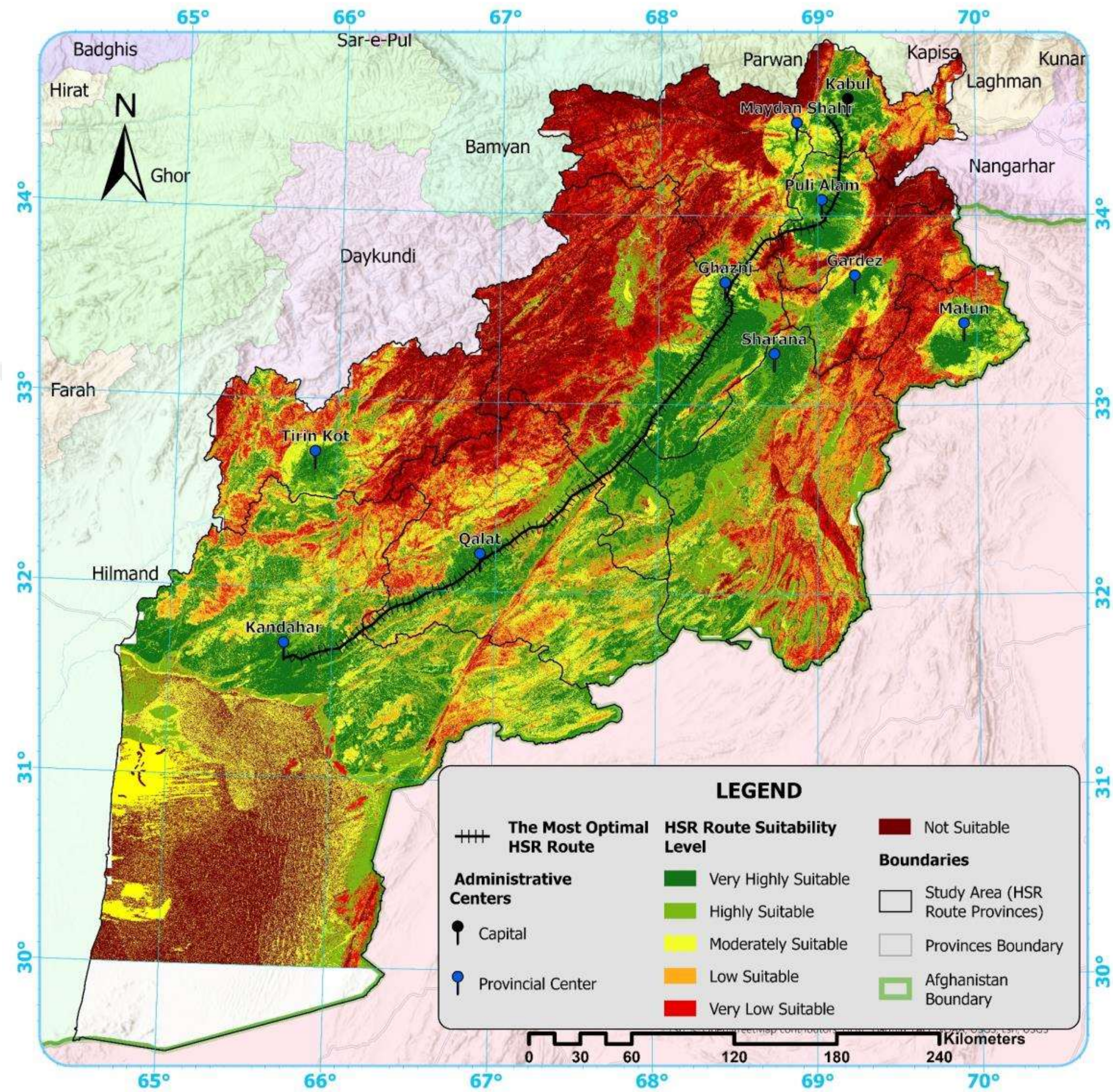


**Figure 5.9.** *The generated HSR route alignment between Kabul and Kandahar cities, passing in the vicinity of Puli Alam, Gazni, and Qalat cities.*

## 6. DISCUSSION

The results indicate that the optimal HSR route determined by GIS, MCDA, and RS techniques in this study, is geometrically the shortest, economically viable, safest in terms of natural disaster risks, and functionally with wide-range serviceability, which confirms the capability and robustness of the adopted methodology. The fuzzy-AHP method and the LCPA had an outstanding performance in determining the HSR route in this study; the performance of the method is highlighted in the following paragraphs through discussing the results.

The generated HSR suitability map revealed that 17.3% of the study area is very highly suitable and 14.3% highly suitable for establishing an HSR route, while 51.8% is not suitable and 22.3% is very low suitable. Furthermore, the very high and highly suitable areas are mostly stretched from Kabul toward the Kandahar direction. The generated optimal HSR route in this study has a 502 km length that creates a corridor by connecting Kabul and Kandahar cities and passing in the vicinity of Puli Alam, Gazni, and Qalat cities. The route provides the widest service area to these four cities and the nearby rural areas and villages.  The distances of the route to the centers of the Puli Alam, Gazni, and Qalat cities are 4.7 km, 2.4 km, and 3.6 km, respectively, while the distances to the vicinity of these cities are 2.5 km, 1.5 km, and 3 km, respectively. The short distance of the route to the cities guarantees the passengers flow, population growth, urban redevelopment, and economic productivity.

The HSR route has 50 intersections with roads along the route; four intersections are with trunk roads, three with primary roads, and seven others with secondary roads, while there are 36 intersections with local streets. Most of the streets are located in rural areas, and the majority of them are unpaved; therefore, they could be directed to use one underpass/overpass to cross the HSR route by rerouting these streets. Consequently, the number of intersections could decrease, which can significantly reduce project costs.

Furthermore, the route has crisscrossed with rivers and streams in 21 locations; 5 intersections are with main rivers, while 16 others are with small or medium-sized streams. The rivers' width at intersections with Paghman, Kabul, Logar, Ghazni, and Trank main rivers are 20 m, 22 m, 65 m, 70 m, and 55 m, respectively. In addition, 12 streams are the tributaries of the Trank river, and 3 others are of the Ghazni rivers.

The HSR route has four intersection points with faultlines. The route has one intersection point with Mokur faultline at (67.2366316°E 32.3448936°N) location by a 45° angle, and three intersections with Chaman faultline at the following locations: (67.6824993°E 32.6335181°N) by 20° angle, (68.4484009°E 33.5517463°N) by 45° angle, and (68.5412988°E 33.7436470°N) by 20° angle. Most importantly, the route avoided intersection with the Paghman fault, which is an active fault with the potential of creating destructive earthquakes.

The HSR route has minimum risk of natural disaster in most of the areas across the route alignment. More than 99.3% of the route alignment has a very low and low landslide risk; only 700 m of the route is in high landslide risk areas. Approximately 277.13 km, 221.69 km, and 2.8 km of the route are in very low, low, and moderate risky areas, respectively. The route has the lowest possible avalanche risk, about 98.3% (493.78 km) and 1.7% (8.33 km) of the study area is located in very low and low-risk areas, while only 210 m of the route is in the moderate risk area. The route is prone to flood risk in different locations, and a significant length of the route is located in very high and high-risk areas. Approximately 3.7% (18.48 km) of the route is highly and very highly prone to floods, while 93.63 km, 195.06 km, and 195.16 km of the route are located in moderate, low, and very low-risk areas, respectively. The highly and very highly risky segments of the route are generally at intersection points with rivers which can be resolved after constructing bridges over the rivers. Most of the risky segments of the route are located near Puli Alam city.

The results imply that about 93.6% (470.05 km) of the generated HSR route is located in areas with a slope less than 4%, while 6% (30.35 km) is located in areas with slopes between 4 to 10% and only 0.4% (1.93 km) in areas with slopes steeper than 10%. The HSR route has slopes greater than 10% in two locations; based on the observations and location assessment, it is very suitable to construct tunnels in these locations. The start and endpoints of the potential tunnels are specified as follow: (68.7480167°E 33.8923795°N) and (68.7764055°E 33.9068297°N) for the first tunnel with 3 km length; (68.1193230°E 34.1061980°N) and (69.1263871°E 34.1137005°N) for the second tunnel with 1 km length.

The result of the study suggests that the study area has a very high potential for implementing an HSR project with lower construction costs and higher operational efficiency. The study area is very suitable in terms of horizontal slope and LULC types. In addition, the natural disaster risk is very low in most parts of the area, which allows applying some modification in the implementation phase of the HSR route. Furthermore, the fuzzy-AHP method adopted in this study also has satisfactory results in eliminating the vagueness and inconsistency present in the judgment matrix.

The main limitation of this study was the inability of the ArcGIS Pro and other software to maintain the horizontal slope of the route in hillsides. The slope function in ArcGIS Pro and other software' produce the slope values only parallel to the slope direction; based on the slope values, it is not possible to place a route in high slope values, while the route can pass through higher slope values perpendicular or at a specific angle to the slope direction by maintaining the design slope. Therefore, the slope values could mislead the route in some areas with complex topography. Furthermore, this study had some limitations in terms of data aquation and processing. The unavailability of accurate datasets such as rivers and the misclassification of roads were the study's two major limitations, which have taken a very long time to check and clean. Moreover, the size of the study area has also led to longer processing times and necessitated a powerful workstation computer to process the data as the ordinary laptops and desktops were unable to do, especially for maintaining the required raster resolution for the data. Lake of comprehensive technical specifications to demonstrate all details and requirements for an HSR route was another very evident limitation most of the time. In addition, performing the survey and filling the questionary forms by experts was another limitation of the study; the questionary forms were sent to several companies, experts, and professors requesting to perform the survey, but only two requests were answered, and the forms were sent back.

# 7. CONCLUSIONS AND RECOMMENDATIONS

HSR networks are improving economic productivity by connecting the adjacent cities, creating an economic corridor that ensures a smooth and frequent economic exchange and sustaining the agglomeration of funds and talents. Furthermore, HSR has considered the most effective and environmentally friendly mode of transportation, which has both the lowest energy consumption and $CO_2$ emissions. The HSR lines have a substantial impact on the ravel patterns, landuse redevelopment, improving regional economy, and environmental characteristics of the potential service areas. Hence, comprehensive route planning and locational assessment are vital for selecting the most optimal route. The determination of the HSR route is a highly complex process and involves various factors at different levels. The HSR route can be determined using conventional or modern survey methods. Modern survey methods are more effective as they consider several factors, while conventional survey methods are generally based on only topographical maps. Modern survey methods rely on RS and GIS technologies integrated with MCDA methods that are robust, effective, and time and costs saving.

The primary aim of this thesis was to develop a practical method to select the best optimal HSR route considering the most prominent engineering, natural disaster risk, economic, and environmental factors using GIS, RS, and MCDA techniques. To reach this goal, the research objectives were formulated as follow:

1. To introduce a more effective, accurate, cost-effective, and modern survey method for solving the route selection problem.
2. To find economically and geometrically the most optimal route.
3. To apply different MCDA methods for weighing the criteria and ranking the alternatives; accordingly, evaluating their effectiveness, accuracy, and assessing their results in the study area.
4. To generate the shortest possible route by implementing LCPA.
5. To optimize an HSR route with a wide-range service area to serve the greatest number of populations.
6. To identify the safest route in terms of natural disaster risks by carefully assessing the study area.

The scientific research presented in this thesis has led to meeting all the objectives listed above. The first objective is met by employing the fuzzy-AHP method combined with GIS and RS techniques, which can resolve the routing problem by eliminating the expert's inconsistency in the judgment matrix and generating a route using GIS and RS resources.

The second objective is met by considering the maximum gradient for the HSR route alignment to reduce the number of bridges and cut/fill operation. In addition, the LULC types were carefully scored to avoid costly agricultural lands, buildup areas, and forests. The intersections with existing roads and rivers are decreased to a minimum by setting restrictive buffer zones around them, which can tremendously decrease the project costs.

The third objective of the study is met by comparing the AHP and fuzzy-AHP methods capabilities in handling a greater number of criteria and calculating the criteria weights, which showed sharp feasibility of the fuzzy-AHP in handling several criteria and management of the inconsistencies associated with the expert judgments. In addition, the simplicity of the fuzzy-AHP survey is also considered a significant advantage over the AHP method, as in fuzzy-AHP, the expert does not need to redo a very long questionary form to maintain the consistency of the judgment matrix.

The fourth objective of the study is met by generating the shortest route considering multiple criteria by utilizing the LCPA and the LCP tool of ArcGIS pro software, which considers every possible route from origin to destination and generates the shortest path as a result of the tool.

The fifth objective is met by creating suitability buffer zones around 10 different cities along the potential HSR route. These buffer zones made it possible to connect the maximum number of cities and towns.

The sixth objective of the study, which is not considered in most of the studies, is met by a comprehensive assessment of the natural disaster risk along the potential HSR route in the study area. The landslide, snow avalanche, flood, and earthquakes are identified as the most probable and destructive natural disasters in the study area.

For future works, we strongly recommend developing a method that allows a potential route to choose a horizontal slope along the route perpendicular to the slope direction used by GIS software. In addition, it is recommended first to conduct a separate analysis for selecting the most appropriate HSR station's locations in the origin and destination cities, as well as for the adjacent cities, and the routing process can then be carried between these stations in separate segments. Furthermore, it is recommended to carefully study the master plan of each city for areas dedicated to transportation expansion that can be masked to locate the HSR route in those areas.

# REFERENCES


Abatzoglou, J. T., Dobrowski, S. Z., Parks, S. A., & Hegewisch, K. C. (2018). TerraClimate, a high-resolution global dataset of monthly climate and climatic water balance from 1958-2015. *Scientific Data*, *5*, 1–12. https://doi.org/10.1038/sdata.2017.191

Abdı, A., Bouamrane, A., Karech, T., Dahri, N., & Kaouachi, A. (2021). Landslide Susceptibility Mapping Using GIS-based Fuzzy Logic and the Analytical Hierarchical Processes Approach: A Case Study in Constantine (North-East Algeria). *Geotechnical and Geological Engineering*, *39*(8), 5675–5691. https://doi.org/10.1007/S10706-021-01855-3/FIGURES/12

Abdullah, S. H., Chmyriov, V. M., & Dronov, V. I. (2008). Geology and mineral resources of Afghanistan. In *ESCAP United Nations*. ESCAP United Nations.

Acharya, T. D., Yang, I. T., & Lee, D. H. (2017). GIS-based preliminary feasibility study for the optimal route selection for China-India railway through Nepal. *Journal of the Korean Society of Surveying, Geodesy, Photogrammetry and Cartography*, *35*(4), 281–289. https://doi.org/10.7848/ksgpc.2017.35.4.281

Afghan Red Crescent Society. (2021). *Afghanistan: Flash Floods*. https://reliefweb.int/sites/reliefweb.int/files/resources/MDRAF006dfr.pdf

Ahmad, M., & Shahzad Siddiqui, A. (2017). A Study on Fuzzy AHP method and its applications in a "tie-breaking procedure." *Global Journal of Pure and Applied Mathematics*, *13*(6), 1619–1630. http://www.ripublication.com

Akay, H. (2021). Spatial modeling of snow avalanche susceptibility using hybrid and ensemble machine learning techniques. *Catena*, *206*(May), 105524. https://doi.org/10.1016/j.catena.2021.105524

Akinci, H., & Yavuz Ozalp, A. (2021). Landslide susceptibility mapping and hazard assessment in Artvin (Turkey) using frequency ratio and modified information value model. *Acta Geophysica*, *69*(3), 725–745. https://doi.org/10.1007/s11600-021-00577-7

Al-Hameedawi, A., Salih, M., Mohammed, H., & Hassan, M. (2018). Selecting optimum railway track using GIS techniques. *MATEC Web of Conferences*, *162*, 1–4. https://doi.org/10.1051/matecconf/201816203018

Ali, S. A., Parvin, F., Vojteková, J., Costache, R., Linh, N. T. T., Pham, Q. B., Vojtek, M., Gigović, L., Ahmad, A., & Ghorbani, M. A. (2021). GIS-based landslide susceptibility modeling: A comparison between fuzzy multi-criteria and machine learning algorithms. *Geoscience Frontiers*, *12*(2), 857–876. https://doi.org/10.1016/J.GSF.2020.09.004

Asian Development Bank Institute. (2021). *Frontiers in High-Speed Rail Development* (Y. Hayashi, W. Rothengatter, & K. Seetha Ram (eds.)). Asian Development Bank Institute. www.adbi.org

Beale, M. (2006). Route Selection Criteria for a New Railway. *Conference On Railway Engineering*, *May*, 1–8.

Belal, E. M., Khalil, A. A., & El-Dash, K. M. (2020). Economic investigation for building a high-speed rail in developing countries: The case of Egypt. *Ain Shams Engineering Journal*, *11*(4), 1001–1011. https://doi.org/10.1016/J.ASEJ.2020.02.003

Brožová, N., Baggio, T., D'agostino, V., Bühler, Y., & Bebi, P. (2021). Multiscale analysis of surface roughness for the improvement of natural hazard modelling. *Natural Hazards and Earth System Sciences*, *21*(11), 3539–3562. https://doi.org/10.5194/nhess-21-3539-2021

Byers, W. G. (2004). Rilroad Lifeline Damage in Earthquakes. *13th World Conference on Earthquake Engineering Vancouver, B.C., Canada*. https://www.iitk.ac.in/nicee/wcee/article/13_324.pdf

Cao, L., Yang, C., & Zhang, J. (2020). Derailment Behaviors of the Train-Ballasted Track-Subgrade System Subjected to Earthquake Using Shaking Table. *KSCE Journal of Civil Engineering 2020 24:10*, *24*(10), 2949–2960. https://doi.org/10.1007/S12205-020-0005-6

Chang, D. Y. (1996). Applications of the extent analysis method on fuzzy AHP. *European Journal of Operational Research*, *95*(3), 649–655. https://doi.org/10.1016/0377-2217(95)00300-2

Chang, Y., Lei, S., Teng, J., Zhang, J., Zhang, L., & Xu, X. (2019). The energy use and environmental emissions of high-speed rail transportation in China: A bottom-up modeling. *Energy*, *182*, 1193–1201. https://doi.org/10.1016/J.ENERGY.2019.06.120

Chen, P., Lu, Y., Wan, Y., & Zhang, A. (2021). Assessing carbon dioxide emissions of high-speed rail: The case of Beijing-Shanghai corridor. *Transportation Research Part D: Transport and Environment*, *97*, 102949. https://doi.org/10.1016/J.TRD.2021.102949

Chen, W., Hong, H., Panahi, M., Shahabi, H., Wang, Y., Shirzadi, A., Pirasteh, S., Alesheikh, A. A., Khosravi, K., Panahi, S., Rezaie, F., Li, S., Jaafari, A., Bui, D. T., & Bin Ahmad, B. (2019). Spatial Prediction of Landslide Susceptibility Using GIS-Based Data Mining Techniques of ANFIS with Whale Optimization Algorithm (WOA) and Grey Wolf Optimizer (GWO). *Applied Sciences 2019, Vol. 9, Page 3755*, *9*(18), 3755. https://doi.org/10.3390/APP9183755

Choubin, B., Borji, M., Hosseini, F. S., Mosavi, A., & Dineva, A. A. (2020). Mass wasting susceptibility assessment of snow avalanches using machine learning models. *Scientific Reports 2020 10:1*, *10*(1), 1–13. https://doi.org/10.1038/s41598-020-75476-w

Choubin, B., Borji, M., Mosavi, A., Sajedi-Hosseini, F., Singh, V. P., & Shamshirband, S. (2019). Snow avalanche hazard prediction using machine learning methods. *Journal of Hydrology*, *577*, 123929. https://doi.org/10.1016/J.JHYDROL.2019.123929

Chun-hao, W., Peng, C., Yu-sheng, L., Alcá ntara AYALA, I., Chao, H., & Shu-jian, Y. (2018). Seismogenic fault and topography control on the spatial patterns of landslides triggered by the 2017 Jiuzhaigou earthquake. *J. Mt. Sci*, *15*(4), 793–807. https://doi.org/10.1007/s11629-017-4761-9

Costache, R., Pham, Q. B., Sharifi, E., Linh, N. T. T., Abba, S. I., Vojtek, M., Vojteková, J., Nhi, P. T. T., & Khoi, D. N. (2020). Flash-flood susceptibility assessment using multi-criteria decision making and machine learning supported by remote sensing and GIS techniques. *Remote Sensing*, *12*(1). https://doi.org/10.3390/RS12010106

Dalkic, G., Balaban, O., Tuydes-Yaman, H., & Celikkol-Kocak, T. (2017). An assessment of the CO2 emissions reduction in high speed rail lines: Two case studies from Turkey. *Journal of Cleaner Production*, *165*, 746–761. https://doi.org/10.1016/J.JCLEPRO.2017.07.045

Darabi, H., Torabi Haghighi, A., Rahmati, O., Jalali Shahrood, A., Rouzbeh, S., Pradhan, B., & Tien Bui, D. (2021). A hybridized model based on neural network and swarm intelligence-grey wolf algorithm for spatial prediction of urban flood-inundation. *Journal of Hydrology*, *603*, 126854. https://doi.org/10.1016/J.JHYDROL.2021.126854

Das, B. M., Emeritus, D., & Sobhan, K. (2012). *Principles of Geotechnical Engineering* (H. Gowans & C. Rizzo (eds.); 8th ed.). Cengage Learning. http://faculty.tafreshu.ac.ir/file/download/course/1583609876-principles-of-geotechnical-engineering-8th-das.pdf

Das, S., & Gupta, A. (2021). Multi-criteria decision based geospatial mapping of flood susceptibility and temporal hydro-geomorphic changes in the Subarnarekha basin, India. *Geoscience Frontiers*, *12*(5), 101206. https://doi.org/10.1016/J.GSF.2021.101206

De Luca, M., Dell'Acqua, G., & Lamberti, R. (2012). High-Speed Rail Track Design Using GIS And Multi-Criteria Analysis. *Procedia - Social and Behavioral Sciences*, *54*, 608–617. https://doi.org/10.1016/j.sbspro.2012.09.778

Ding, Y., Wang, P., Liu, X., Zhang, X., Hong, L., & Cao, Z. (2020). Risk assessment of highway structures in natural disaster for the property insurance. *Natural Hazards*, *104*(3), 2663–2685. https://doi.org/10.1007/S11069-020-04291-3/TABLES/15

Doorga, J. R. S., Magerl, L., Bunwaree, P., Zhao, J., Watkins, S., Staub, C. G., Rughooputh, S. D. D. V., Cunden, T. S. M., Lollchund, R., & Boojhawon, R. (2022). GIS-based multi-criteria modelling of flood risk susceptibility in Port Louis, Mauritius: Towards resilient flood management. *International Journal of Disaster Risk Reduction*, *67*, 102683. https://doi.org/10.1016/J.IJDRR.2021.102683

Durmaz, A. İ., Ünal, E. Ö., & Aydın, C. C. (2019). Automatic pipeline route design with multi-criteria evaluation based on least-cost path analysis and line-based cartographic simplification: A case study of the MUS project in Turkey. *ISPRS International Journal of Geo-Information*, *8*(4), 1–18. https://doi.org/10.3390/ijgi8040173

Eroğlu, H., & Aydin, M. (2018). Solving power transmission line routing problem using improved genetic and artificial bee colony algorithms. *Electrical Engineering*, *100*, 2103–2116. https://doi.org/10.1007/s00202-018-0688-6

Farooq, A., Xie, M., Stoilova, S., & Ahmad, F. (2019). Multicriteria Evaluation of Transport Plan for High-Speed Rail: An Application to Beijing-Xiongan. *Mathematical Problems in Engineering*, *2019*. https://doi.org/10.1155/2019/8319432

Gärds, J., & Oscarsson, M. (2019). Exploring the use of GIS-based Least-cost Corridors for Designing Alternative Highway Alignments. In *KTH Royal Institute of Technology*. https://www.diva-portal.org/smash/get/diva2:1333968/FULLTEXT02.pdf

Getachew, N., & Meten, M. (2021). Weights of evidence modeling for landslide susceptibility mapping of Kabi-Gebro locality, Gundomeskel area, Central Ethiopia. *Geoenvironmental Disasters*, *8*(1), 1–22. https://doi.org/10.1186/S40677-021-00177-Z/FIGURES/11

Gitau, I. K., & Mundia, C. N. (2017). *GIS Modeling for an Optimal Road Route Location : Case Study of Moiben-Kapcherop-Kitale Road*. *6*(1), 26–39. https://doi.org/10.5923/j.ajgis.20170601.03

Godwin Muriki, Lewi Kari, C. Y. K. (2019). *Determination of Optimal Road Alignment Using GIS Least Cost Path Determination of Optimal Road Alignment Using GIS Least Cost Path Analysis : A Case Study of Situm - Gagidu Station , Morobe*. *February*, 0–13.

Gökceoglu, C., & Aksoy, H. (1996). Landslide susceptibility mapping of the slopes in the residual soils of the Mengen region (Turkey) by deterministic stability analyses and image processing techniques. *Engineering Geology*, *44*(1–4), 147–161. https://doi.org/10.1016/S0013-7952(97)81260-4

Goumrasa, A., Guendouz, M., & Guettouche, M. S. (2021). GIS-Based Multi-Criteria

Decision Analysis Approach (GIS-MCDA) for investigating mass movements' hazard susceptibility along the first section of the Algerian North-South Highway. *Arabian Journal of Geosciences*, *14*(10), 1–17. https://doi.org/10.1007/S12517-021-07124-0/FIGURES/7

Goumrasa, A., Guendouz, M., Guettouche, M. S., & Belaroui, A. (2021). Flood hazard susceptibility assessment in Chiffa wadi watershed and along the first section of Algeria North–South highway using GIS and AHP method. *Applied Geomatics*, *13*(4), 565–585. https://doi.org/10.1007/S12518-021-00381-4/FIGURES/8

Greene, R., Devillers, R., Luther, J. E., & Eddy, B. G. (2011). GIS-Based Multiple-Criteria Decision Analysis. *Geography Compass*, *5*(6), 412–432. https://doi.org/10.1111/J.1749-8198.2011.00431.X

Hamid-Mosaku, I. A., Oguntade, O. F., Ifeanyi, V. I., Balogun, A. L., & Jimoh, O. A. (2020). Evolving a comprehensive geomatics multi-criteria evaluation index model for optimal pipeline route selection. *Structure and Infrastructure Engineering*, *16*(10), 1382–1396. https://doi.org/10.1080/15732479.2020.1712435/FORMAT/EPUB

Hamlat, A., Kadri, C. B., Guidoum, A., & Bekkaye, H. (2021). Flood hazard areas assessment at a regional scale in M'zi wadi basin, Algeria. *Journal of African Earth Sciences*, *182*, 104281. https://doi.org/10.1016/J.JAFREARSCI.2021.104281

Hammad, M. (2020). *Landslide hazard assessment using advanced remote sensing techniques and GIS*. University of Szeged.

Haqmal, R., Kaur, M., & Nasir, H. (2019). *Review on Road Conditions in Afghanistan*. *34*, 142–148.

Haque, M. N., Siddika, S., Sresto, M. A., Saroar, M. M., & Shabab, K. R. (2021). Geo-spatial Analysis for Flash Flood Susceptibility Mapping in the North-East Haor (Wetland) Region in Bangladesh. *Earth Systems and Environment*, *5*(2), 365–384. https://doi.org/10.1007/S41748-021-00221-W/TABLES/11

Hasanabadi, A., Almodaresi, S. A., & Boloor, A. (2018). *Optimal Railway Routing using Spatial-Temporal Analysis in Gis ( A Case Study of Bafgh – Yazd , Iran )*. *4*(3), 11–22.

Henn, L., Sloan, K., & Douglas, N. (2013). European case study on the Financing of High Speed Rail. *Australasian Transport Research Forum*.

Hu, Q., Bian, L., & Tan, M. (2020). A data perception model for the safe operation of high-speed rail in rainstorms. *Transportation Research Part D: Transport and Environment*, *83*, 102326. https://doi.org/10.1016/J.TRD.2020.102326

Indian Ministry of Railways. (2020). *Report of Committee on Various Modern Survey Technologies*.

Ivanic, K.-Z., Stolton, S., Figueroa Arango, C., & Dudley, N. (2020). Protected Areas Benefits Assessment Tool + (PA-BAT+): A tool to assess local stakeholder perceptions of the flow of benefits from protected areas. In *Protected Areas Benefits Assessment Tool + (PA-BAT+): A tool to assess local stakeholder perceptions of the flow of benefits from protected areas* (Issue 4). https://doi.org/10.2305/iucn.ch.2020.patrs.4.en

Janic, M. (2015). A Methodology for Assessing Resilience of the Hsr ( High Speed Rail ) Network Affected By Disruptive Event ( S ). *NECTAR 2015 International Conference on "Smart Transport Planning."* http://resolver.tudelft.nl/uuid:f0fbb6ba-c5a4-42cd-b9af-1b306cdeb996

Januadi Putra, M. I., & Novia Utami, N. D. (2020). Routing the highway development by using SuperMap Least Cost Path Analysis (LCPA) and Multi-Criteria Decision Analysis (MCDA) and its assessment toward spatial planning. *IOP Conf. Ser.: Earth Environ. Sci*, *561*. https://doi.org/10.1088/1755-1315/561/1/012019

Japan International Cooperation Agency, & Ministry of Railways Republic of India. (2015). *Joint Feasibility Study for Mumbai-Ahmedabad High Speed Railway Corridor Final Report Volume 1*. https://www.jica.go.jp/english/our_work/social_environmental/id/asia/south/india/c8h0vm00009v1ylc-att/c8h0vm0000bzv4e5.pdf

Jiao, J., Wang, J., Zhang, F., Jin, F., & Liu, W. (2020). Roles of accessibility, connectivity and spatial interdependence in realizing the economic impact of high-speed rail: Evidence from China. *Transport Policy*, *91*, 1–15. https://doi.org/10.1016/J.TRANPOL.2020.03.001

Jiao, Y., Zhao, D., Ding, Y., Liu, Y., Xu, Q., Qiu, Y., Liu, C., Liu, Z., Zha, Z., & Li, R. (2019). Performance evaluation for four GIS-based models purposed to predict and map landslide susceptibility: A case study at a World Heritage site in Southwest China. *CATENA*, *183*, 104221. https://doi.org/10.1016/J.CATENA.2019.104221

Jin, Z., Liu, W., Pei, S., & He, J. (2020). Probabilistic assessment of vehicle derailment based on optimal ground motion intensity measure. *Https://Doi.Org/10.1080/00423114.2020.1792940*, 1–22. https://doi.org/10.1080/00423114.2020.1792940

Jin, Z., Pei, S., Li, X., Liu, H., & Qiang, S. (2016). Effect of vertical ground motion on earthquake-induced derailment of railway vehicles over simply-supported bridges. *Journal of Sound and Vibration*, *383*, 277–294. https://doi.org/10.1016/J.JSV.2016.06.048

Johnston, I., Murphy, W., & Holden, J. (2021). A review of floodwater impacts on the stability of transportation embankments. *Earth-Science Reviews*, *215*, 103553. https://doi.org/10.1016/J.EARSCIREV.2021.103553

Kahraman, C. (2008). *Fuzzy Multi-criteria Decision Making* (P. M. Pardalos & D.-Z. Du (eds.); Vol. 16). Springer Nature. https://doi.org/10.1007/978-0-387-76813-7

Keisler, J. M., & Linkov, I. (2021). Use and Misuse of MCDA to Support Decision Making Informed by Risk. *Risk Analysis*, *41*(9), 1513–1521. https://doi.org/10.1111/RISA.13631

Kiema, D.-I. J. B. K., Dang'ana, M. A., & Karanja, D.-I. F. N. (2007). GIS-Based Railway Route Selection for the Proposed Kenya-Sudan Railway: Case Study of Kitale-Kapenguria Section. *Journal of Civil Engineering Research and Practice*, *4*(1). https://doi.org/10.4314/jcerp.v4i1.29169

Kim, H., Sultana, S., & Weber, J. (2018). A geographic assessment of the economic development impact of Korean high-speed rail stations. *Transport Policy*, *66*, 127–137. https://doi.org/10.1016/J.TRANPOL.2018.02.008

Kırlangıçoğlu, C. (2014). *Optimal Urban Rail Transit Corridor Identification Based on Geographic Information Systems: A Case Study on Istanbul* [Istanbul University]. https://tez.yok.gov.tr/UlusalTezMerkezi/tezDetay.jsp?id=14QrRd2BB4OcnmdkJkz

QbA&no=RyvZ731AZa1ZisOnzmevug

Komikado, H., Morikawa, S., Bhatt, A., & Kato, H. (2021). High-speed rail, inter-regional accessibility, and regional innovation: Evidence from Japan. *Technological Forecasting and Social Change*, *167*, 120697. https://doi.org/10.1016/J.TECHFORE.2021.120697

Kosijer, M., Marković, M., & Belošević, I. (2012). Multicriteria decision-making in railway route planning and design. *GRAĐEVINAR*, *64*(3), 195–205. https://doi.org/10.14256/jce.645.2011

Ku, C. Y., Hsu, S. M., Chiou, L. Bin, & Lin, G. F. (2009). An empirical model for estimating hydraulic conductivity of highly disturbed clastic sedimentary rocks in Taiwan. *Engineering Geology*, *109*(3–4), 213–223. https://doi.org/10.1016/j.enggeo.2009.08.008

Kumar, S., Srivastava, P. K., & Snehmani. (2016). GIS-based MCDA–AHP modelling for avalanche susceptibility mapping of Nubra valley region, Indian Himalaya. *Https://Doi.Org/10.1080/10106049.2016.1206626*, *32*(11), 1254–1267. https://doi.org/10.1080/10106049.2016.1206626

Kumar, S., Srivastava, P. K., & Snehmani. (2018). Geospatial Modelling and Mapping of Snow Avalanche Susceptibility. *Journal of the Indian Society of Remote Sensing*, *46*(1), 109–119. https://doi.org/10.1007/s12524-017-0672-z

Kumar, S., Srivastava, P. K., Snehmani, & Bhatiya, S. (2019). Geospatial probabilistic modelling for release area mapping of snow avalanches. *Cold Regions Science and Technology*, *165*(June), 102813. https://doi.org/10.1016/j.coldregions.2019.102813

Kumar, Y., Panchal, S., Ashish, A., & Singh, B. P. (2017). Feasibility study of railway line in Hilly region using GIS. *International Journal of Online Engineering*, *13*(8), 183–191. https://doi.org/10.3991/ijoe.v13i08.7186

Kursah, M. B. (2017). Least-cost pipeline using geographic information system: The limit to technicalities. *International Journal of Applied Geospatial Research*, *8*(3), 1–15. https://doi.org/10.4018/ijagr.2017070101

Lakušić, S., Haladin, I., Vranešić, K., & Ivo Haladin, A. (2020). Railway infrastructure in earthquake affected areas. *Građevinar*. https://doi.org/10.14256/JCE.2967.2020

Li, F., Su, Y., Xie, J., Zhu, W., & Wang, Y. (2020). The Impact of High-Speed Rail Opening on City Economics along the Silk Road Economic Belt. *Sustainability 2020, Vol. 12, Page 3176*, *12*(8), 3176. https://doi.org/10.3390/SU12083176

Li, Y., Chen, Z., & Wang, P. (2020). Impact of high-speed rail on urban economic efficiency in China. *Transport Policy*, *97*, 220–231. https://doi.org/10.1016/J.TRANPOL.2020.08.001

Lila, R. B. (2018). *Landslide Hazard Modeling in Ventura and Santa Barbara Counties, California Using Multi-Tiered Geospatial Data Analysis* (Issue May). Texas State University.

Liu, J., Wu, Z., & Zhang, H. (2021). Analysis of changes in landslide susceptibility according to land use over 38 years in lixian county, china. *Sustainability (Switzerland)*, *13*(19), 1–23. https://doi.org/10.3390/su131910858

Liu, Y., Deng, Z., & Wang, X. (2021). *The Effects of Rainfall , Soil Type and Slope on the Processes and Mechanisms of Rainfall-Induced Shallow Landslides*.

Liu, Y., Eckert, C. M., & Earl, C. (2020). A review of fuzzy AHP methods for decision-making with subjective judgements. *Expert Systems with Applications*, *161*, 113738. https://doi.org/10.1016/J.ESWA.2020.113738

Long, F., Zheng, L., & Song, Z. (2018). High-speed rail and urban expansion: An empirical study using a time series of nighttime light satellite data in China. *Journal of Transport Geography*, *72*, 106–118. https://doi.org/10.1016/J.JTRANGEO.2018.08.011

Luu, C., Pham, B. T., Phong, T. Van, Costache, R., Nguyen, H. D., Amiri, M., Bui, Q. D., Nguyen, L. T., Le, H. Van, Prakash, I., & Trinh, P. T. (2021). GIS-based ensemble computational models for flood susceptibility prediction in the Quang Binh Province, Vietnam. *Journal of Hydrology*, *599*, 126500. https://doi.org/10.1016/J.JHYDROL.2021.126500

Malczewski, J., & Rinner, C. (2015). Multicriteria Decision Analysis in Geographic Information Science. In *Analysis methods* (Issue Massam 1993).

http://www.amazon.com/Multicriteria-Decision-Analysis-Geographic-Information/dp/3540747567/ref=sr_1_1?ie=UTF8&qid=1430864854&sr=8-1&keywords=Multicriteria+decision+analysis+in+geographic+information+science

Malik, S., Pal, S. C., Arabameri, A., Chowdhuri, I., Saha, A., Chakrabortty, R., Roy, P., & Das, B. (2021). GIS-based statistical model for the prediction of flood hazard susceptibility. *Environment, Development and Sustainability 2021 23:11*, *23*(11), 16713–16743. https://doi.org/10.1007/S10668-021-01377-1

Margreth, S. (2013). When should a hazard map show the risk of small avalanches or snow gliding? *International Snow Science Workshop Grenoble*.

Medrano, F. A. (2016). *Corridor Location: Generating Competitive and Efficient Route Alternatives*. https://escholarship.org/uc/item/4g92536t

Meena, S. R., Ghorbanzadeh, O., & Blaschke, T. (2019). A comparative study of statistics-based landslide susceptibility models: A case study of the region affected by the Gorkha earthquake in Nepal. *ISPRS International Journal of Geo-Information*, *8*(2). https://doi.org/10.3390/ijgi8020094

Meena, S. R., Mishra, B. K., & Piralilou, S. T. (2019). A hybrid spatial multi-criteria evaluation method for mapping landslide susceptible areas in Kullu valley, Himalayas. *Geosciences (Switzerland)*, *9*(4). https://doi.org/10.3390/geosciences9040156

Ministry of Industry and Commerce. (2020). *Afghanistan Trade Report During 2020*. https://moci.gov.af/en/reports

Mohammed Sameer, Y., Abed, A. N., & Naba Sayl, K. (2021). *Highway route selection using GIS and analytical hierarchy process case study Ramadi Heet rural highway*. https://doi.org/10.1088/1742-6596/1973/1/012060

Mosavi, A., Shirzadi, A., Choubin, B., Taromideh, F., Hosseini, F. S., Borji, M., Shahabi, H., Salvati, A., & Dineva, A. A. (2020). Towards an Ensemble Machine Learning Model of Random Subspace Based Functional Tree Classifier for Snow Avalanche Susceptibility Mapping. *IEEE Access*, *8*, 145968–145983. https://doi.org/10.1109/ACCESS.2020.3014816

Nakileza, B. R., & Nedala, S. (2020). Topographic influence on landslides characteristics and implication for risk management in upper Manafwa catchment, Mt Elgon Uganda. *Geoenvironmental Disasters*, *7*(1), 1–13. https://doi.org/10.1186/S40677-020-00160-0/FIGURES/7

Nasery, S., & Kalkan, K. (2021). Snow avalanche risk mapping using GIS-based multi-criteria decision analysis: the case of Van, Turkey. *Arabian Journal of Geosciences*, *14*(9). https://doi.org/10.1007/s12517-021-07112-4

National Environmental Protection Agency. (2019). *Initial Biennial Update Report Under The United Nation Framework Convention On Climate Change (UNFCCC)*. https://unfccc.int/sites/default/files/resource/BUR Report_Final.pdf

National Statistics and Information Authority. (2020). *Estimated Population of Afghanistan 2020-2021*. https:/nsia.gov.af

Nepal, N., Chen, J., Chen, H., Wang, X., & Pangali Sharma, T. P. (2019). Assessment of landslide susceptibility along the Araniko Highway in Poiqu/Bhote Koshi/Sun Koshi Watershed, Nepal Himalaya. *Progress in Disaster Science*, *3*, 100037. https://doi.org/10.1016/J.PDISAS.2019.100037

Ngunyi, J., Mundia, C., & Gachari, M. (2017). Analysis of Standard Gauge Railway Using GIS and Remote Sensing. *American Journal of Geographic Information System*, *6*(2), 54–63. https://doi.org/10.5923/j.ajgis.20170602.02

Nseka, D., Kakembo, V., Bamutaze, Y., & Mugagga, F. (2019). Analysis of topographic parameters underpinning landslide occurrence in Kigezi highlands of southwestern Uganda. *Natural Hazards*, *99*(2), 973–989. https://doi.org/10.1007/S11069-019-03787-X/FIGURES/6

Padaya, J., Juremalani, J., & Prakash, I. (2017). Design of railway alignment: conventional and modern method. *International Research Journal of Engineering and Technology*. www.irjet.net

Panchal, S. (2017). *Rail-Route Planning Using a Geographical Information System ( GIS )*. *7*(5), 2010–2013.

Parshad, R., Srivastva, P. K., Snehmani, Ganguly, S., Snehmani, & Snehmani. (2017).

Snow Avalanche Susceptibility Mapping using Remote Sensing and GIS in Nubra-Shyok Basin, Himalaya, India. *Indian Journal of Science and Technology*, *10*(31), 1–12. https://doi.org/10.17485/ijst/2017/v10i31/105647

Paryani, S., Neshat, A., Javadi, S., & Pradhan, B. (2020). Comparative performance of new hybrid ANFIS models in landslide susceptibility mapping. *Natural Hazards*, *103*(2), 1961–1988. https://doi.org/10.1007/s11069-020-04067-9

Patil, A. N. (2018). *Fuzzy ahp methodology and its sole applications*. *December*, 23–32.

Perla, R. I., & Martinelli, J. M. (2004). Agriculture handbook 489 u.s. department of agriculture forest service. In *Us Depratment of Agriculture*. https://www.n-sda.org/files/education/handbooks/Avalanche.pdf

Qizhou, H., Xin, F., & Lishuang, B. (2021). Natural disaster warning system for safe operation of a high-speed railway. *Transportation Safety and Environment*, *3*(4), 19. https://doi.org/10.1093/TSE/TDAB019

Rahmati, O., Ghorbanzadeh, O., Teimurian, T., Mohammadi, F., Tiefenbacher, J. P., Falah, F., Pirasteh, S., Ngo, P. T. T., & Bui, D. T. (2019). Spatial Modeling of Snow Avalanche Using Machine Learning Models and Geo-Environmental Factors: Comparison of Effectiveness in Two Mountain Regions. *Remote Sensing 2019, Vol. 11, Page 2995*, *11*(24), 2995. https://doi.org/10.3390/RS11242995

Rao, K. R., Sreekeshava, K. S., Dharek, M. S., & Sunagar, P. (2018). Raster least cost approach for automated corridor alignment in undulated terrain. *International Journal of Recent Technology and Engineering*, *8*(1), 1–4. https://doi.org/10.2139/ssrn.3517652

Richard, E. M. (2020). *Landslides in Northeastern Minnesota: Inventory Mapping and Susceptibility Assessment*. UNIVERSITY OF MINNESOTA.

Riley, S. J., DeGloria, S. D., & Elliot, R. (1999). A Terrain Ruggedness Index That Quantifies Topographic Heterogeneity. In *Intermountain Journal of Science* (Vol. 5, pp. 23–27).

Saat, M. R., & Aguilar Serrano, J. (2015). Multicriteria high-speed rail route selection: application to Malaysia's high-speed rail corridor prioritization. *Transportation*

*Planning and Technology*, *38*(2), 200–213. https://doi.org/10.1080/03081060.2014.997446

Saat, M. R., & Serrano, J. A. (2015). Multicriteria high-speed rail route selection: application to Malaysia's high-speed rail corridor prioritization. *Http://Dx.Doi.Org/10.1080/03081060.2014.997446*, *38*(2), 200–213. https://doi.org/10.1080/03081060.2014.997446

Saaty, T. L. (1977). A scaling method for priorities in hierarchical structures. *Journal of Mathematical Psychology*, *15*(3), 234–281. https://doi.org/10.1016/0022-2496(77)90033-5

Saaty, T. L. (1988). What is The Analytic Hierarchy Process? *Mathematical Models for Decision Support*, *F48*.

Saaty, T. L., & Vargas, L. G. (1980). Hierarchical analysis of behavior in competition: Prediction in chess. *Behavioral Science*, *25*(3), 180–191. https://doi.org/10.1002/bs.3830250303

Sahu, A., Bose, T., & Samal, D. R. (2021). *Urban Flood Risk Assessment and Development of Urban Flood Resilient Spatial Plan for Bhubaneswar*. https://doi.org/10.1177/09754253211042489

Sarı, F., & Sen, M. (2017). Least Cost Path Algorithm Design For Highway Route Selection. *International Journal of Engineering and Geosciences*, *2*(1), 1–8. https://doi.org/10.26833/IJEG.285770

Schito, J. (2017). Modeling and optimizing transmission lines with GIS and multi-criteria decision analysis. *IT - Information Technology*, *59*(1), 31–39. https://doi.org/10.1515/ITIT-2016-0057/MACHINEREADABLECITATION/RIS

Schubert, F. N. (1991). U.S. Army Corps of Engineers and Afghanistan's Highways 1960-1967. *Journal of Construction Engineering and Management*, *117*(3). https://apps.dtic.mil/sti/pdfs/ADA524269.pdf

Schweizer, J., Jamieson, J. B., & Schneebeli, M. (2003). Snow avalanche formation. *Reviews of Geophysics*, *41*(4). https://doi.org/10.1029/2002RG000123

Sethia, K. K., Pandey, P., Chattoraj, S., Manickam, S., & Champati ray, P. K. (2018).

Mapping, modeling and simulation of snow avalanche in Alaknanda Valley, central Himalaya: Hazard assessment. *International Geoscience and Remote Sensing Symposium (IGARSS)*, *2018-July*, 5150–5153. https://doi.org/10.1109/IGARSS.2018.8518516

Shahiri Tabarestani, E., & Afzalimehr, H. (2021). Artificial neural network and multi-criteria decision-making models for flood simulation in GIS: Mazandaran Province, Iran. *Stochastic Environmental Research and Risk Assessment*, *35*(12), 2439–2457. https://doi.org/10.1007/S00477-021-01997-Z/FIGURES/14

Shano, L., Raghuvanshi, T. K., & Meten, M. (2021). Landslide susceptibility mapping using frequency ratio model: the case of Gamo highland, South Ethiopia. *Arabian Journal of Geosciences*, *14*(7), 1–18. https://doi.org/10.1007/S12517-021-06995-7/TABLES/2

Sinarta, I. N., Rifa'I, A., Fathani, T. F., & Wilopo, W. (2017). Slope Stability Assessment Using Trigger Parameters and SINMAP Methods on Tamblingan-Buyan Ancient Mountain Area in Buleleng Regency, Bali. *Geosciences 2017, Vol. 7, Page 110*, *7*(4), 110. https://doi.org/10.3390/GEOSCIENCES7040110

Singh, A., Juyal, V., Kumar, B., Gusain, H. S., Shekhar, M. S., Singh, P., Kumar, S., & Negi, H. S. (2021). Avalanche hazard mitigation in east Karakoram mountains. *Natural Hazards*, *105*(1), 643–665. https://doi.org/10.1007/s11069-020-04329-6

Singh, M. P., Singh, P., & Singh, P. (2019). Fuzzy AHP-based multi-criteria decision-making analysis for route alignment planning using geographic information system (GIS). In *Journal of Geographical Systems* (Vol. 21, Issue 3). Springer Berlin Heidelberg. https://doi.org/10.1007/s10109-019-00296-0

Singh, P., Sharma, A., Sur, U., & Rai, P. K. (2021). Comparative landslide susceptibility assessment using statistical information value and index of entropy model in Bhanupali-Beri region, Himachal Pradesh, India. *Environment, Development and Sustainability*, *23*(4), 5233–5250. https://doi.org/10.1007/S10668-020-00811-0/FIGURES/5

Singh, V., Thakur, K., Garg, V., & Aggarwal, S. P. (2018). Assessment of Snow Avalanche Susceptibility of Road Network: A Case Study of Alaknanda Basin. *The*

*International Archives of the Photogrammetry, Remote Sensing and Spatial Information Sciences*, *XLII–5*. https://doi.org/10.5194/isprs-archives-XLII-5-461-2018

Smith, S. A. (2017). *GIS-based evaluation of landslide susceptibility for Eastern Tennessee*. Mississippi State University.

Sobandi Dwi Putra, M., Andryana, S., Gunaryati, A., Editor, G., & Zeng, Q. (2018). *Fuzzy Analytical Hierarchy Process Method to Determine the Quality of Gemstones*. https://doi.org/10.1155/2018/9094380

Soteres, R. L., Pedraza, J., & Carrasco, R. M. (2020). Snow avalanche susceptibility of the Circo de Gredos (Iberian Central System, Spain). *Journal of Maps*, *16*(2), 155–165. https://doi.org/10.1080/17445647.2020.1717655/FORMAT/EPUB

Stamellou, E., Kalogeropoulos, K., Stathopoulos, N., Tsesmelis, D. E., Louka, P., Apostolidis, V., & Tsatsaris, A. (2021). A GIS-Cellular Automata-Based Model for Coupling Urban Sprawl and Flood Susceptibility Assessment. *Hydrology 2021, Vol. 8, Page 159*, *8*(4), 159. https://doi.org/10.3390/HYDROLOGY8040159

Stavropoulos, S., Zaimes, G. N., Filippidis, E., Diaconu, D. C., & Emmanouloudis, D. (2020). Mitigating flash floods with the use of new technologies: A Multi-criteria decision analysis to map flood susceptibility for Zakynthos Island, Greece. *Journal of Urban and Regional Analysis*, *12*(2), 233–248. https://doi.org/10.37043/JURA.2020.12.2.7

Stinson, P. T., Naglak, M. C., Mandel, R. D., & Hoopes, J. W. (2016). The remote-sensing assessment of a threatened ancient water technology in Afghanistan. *Journal of Archaeological Science: Reports*, *10*, 441–453. https://doi.org/10.1016/J.JASREP.2016.10.004

Sujatha, E. R., & Sridhar, V. (2021). Landslide Susceptibility Analysis: A Logistic Regression Model Case Study in Coonoor, India. *Hydrology 2021, Vol. 8, Page 41*, *8*(1), 41. https://doi.org/10.3390/HYDROLOGY8010041

Sur, U., Singh, P., Rai, P. K., & Thakur, J. K. (2021). Landslide probability mapping by considering fuzzy numerical risk factor (FNRF) and landscape change for road corridor of Uttarakhand, India. *Environment, Development and Sustainability*, *23*(9), 13526–13554. https://doi.org/10.1007/s10668-021-01226-1

Tarife, R. P., Nakanishi, Y., Bondaug, J. V. S., Irosido, R. V., Tahud, A. P., & Estoperez, N. R. (2020). Optimization of Electric Transmission Line Routing for a Renewable Energy Based Micro-Grid System using Geographic Information System (GIS) Spatial Analysis. *9th International Conference on Renewable Energy Research and Applications, ICRERA 2020*, 215–220. https://doi.org/10.1109/ICRERA49962.2020.9242762

Teich, M., Bartelt, P., Grêt-Regamey, A., & Bebi, P. (2012). *Arctic, Antarctic, and Alpine Research Snow Avalanches in Forested Terrain: Influence of Forest Parameters, Topography, and Avalanche Characteristics on Runout Distance*. *44*(4), 509–519. https://doi.org/10.1657/1938-4246-44.4.509

Tekin, S. (2021). Completeness of landslide inventory and landslide susceptibility mapping using logistic regression method in Ceyhan Watershed (southern Turkey). *Arabian Journal of Geosciences*, *14*(17), 1–14. https://doi.org/10.1007/S12517-021-07583-5/FIGURES/13

The World Bank. (2017). *Disaster Risk Profile: Afghanistan*. https://www.gfdrr.org/sites/default/files/afghanistan_low_FINAL.pdf

Tiryaki, M., & Karaca, O. (2018). Flood susceptibility mapping using GIS and multicriteria decision analysis: Saricay-Çanakkale (Turkey). *Arabian Journal of Geosciences*, *11*(14), 1–17. https://doi.org/10.1007/S12517-018-3675-3/TABLES/3

Tiwari, A., G., A., & Vishwakarma, B. D. (2021). Parameter importance assessment improves efficacy of machine learning methods for predicting snow avalanche sites in Leh-Manali Highway, India. *Science of The Total Environment*, *794*, 148738. https://doi.org/10.1016/J.SCITOTENV.2021.148738

UIC-International union of railways. (2018). *High-speed rail, Fast track to sustainable mobility* . https://uic.org/IMG/pdf/uic_high_speed_2018_ph08_web.pdf

United Nations Economic Commission for Europe. (2017). *Trans-European Railway High-Speed Master Plan Study*. https://unece.org/DAM/trans/main/ter/terdocs/TER_High-Speed_Master_Plan_Study.pdf

Vakhshoori, V., Pourghasemi, H. R., Zare, M., & Blaschke, T. (2019). Landslide Susceptibility Mapping Using GIS-Based Data Mining Algorithms. *Water 2019, Vol. 11, Page 2292*, *11*(11), 2292. https://doi.org/10.3390/W11112292

van Laarhoven, P. J. M., & Pedrycz, W. (1983). A fuzzy extension of Saaty's priority theory. *Fuzzy Sets and Systems*, *11*(1–3), 229–241. https://doi.org/10.1016/S0165-0114(83)80082-7

Varol, N. (2022). Avalanche susceptibility mapping with the use of frequency ratio, fuzzy and classical analytical hierarchy process for Uzungol area, Turkey. *Cold Regions Science and Technology*, *194*, 103439. https://doi.org/10.1016/J.COLDREGIONS.2021.103439

Veitinger, J. (2015). *Release Areas of Snow Avalanches: New Methods and Parameters*.

Vojtek, M., Vojteková, J., Costache, R., Pham, Q. B., Lee, S., Arshad, A., Sahoo, S., Linh, N. T. T., & Anh, D. T. (2021). Comparison of multi-criteria-analytical hierarchy process and machine learning-boosted tree models for regional flood susceptibility mapping: a case study from Slovakia. *Http://Www.Tandfonline.Com/Action/JournalInformation?Show=aimsScope&journalCode=tgnh20#.VsXodSCLRhE*, *12*(1), 1153–1180. https://doi.org/10.1080/19475705.2021.1912835

Voumard, J., Derron, M. H., & Jaboyedoff, M. (2018). Natural hazard events affecting transportation networks in Switzerland from 2012 to 2016. *Natural Hazards and Earth System Sciences*, *18*(8), 2093–2109. https://doi.org/10.5194/NHESS-18-2093-2018

Wahdan, A., Effat, H., Abdallah, N., & Elwan, K. (2019). Design an Optimum Highway Route using Remote Sensing Data and GIS-Based Least Cost Path Model, Case of Minya-Ras Ghareb and Minya-Wahat-Bawiti Highway Routes, Egypt. *Technology, and Sciences (ASRJETS) American Scientific Research Journal for Engineering*, *56*(1), 157–181. http://asrjetsjournal.org/

Wahdana, A., Effat, H., Abdallah, N., & Elwan, K. (2019). Design an Optimum Highway Route using Remote Sensing Data and GIS-Based Least Cost Path Model, Case of Minya-Ras Ghareb and Minya-Wahat-Bawiti Highway Routes, Egypt. *American*

*Scientific Research Journal for Engineering, Technology, and Sciences (ASRJETS)*, *56*(1), 157–181. https://asrjetsjournal.org/index.php/American_Scientific_Journal/article/view/4863/1723

Wan, Z., Hook, S., & Hulley, G. (2015). Terra Land Surface Temperature/Emissivity 8-Day L3 Global 1km SIN Grid V006 [Data set]. In *NASA EOSDIS Land Processes DAAC*. NASA EOSDIS Land Processes DAAC. https://doi.org/10.5067/MODIS/MOD11A2.006

Wang, F., Wei, X., Liu, J., He, L., & Gao, M. (2019). Impact of high-speed rail on population mobility and urbanisation: A case study on Yangtze River Delta urban agglomeration, China. *Transportation Research Part A: Policy and Practice*, *127*, 99–114. https://doi.org/10.1016/J.TRA.2019.06.018

Wang, L., Acheampong, R. A., & He, S. (2020). High-speed rail network development effects on the growth and spatial dynamics of knowledge-intensive economy in major cities of China. *Cities*, *105*, 102772. https://doi.org/10.1016/J.CITIES.2020.102772

Wang, Q., Guo, Y., Li, W., He, J., & Wu, Z. (2019). Predictive modeling of landslide hazards in Wen County, northwestern China based on information value, weights-of-evidence, and certainty factor. *Http://Www.Tandfonline.Com/Action/JournalInformation?Show=aimsScope&journalCode=tgnh20#.VsXodSCLRhE*, *10*(1), 820–835. https://doi.org/10.1080/19475705.2018.1549111

Wang, Q., Liu, K., Wang, M., & Koks, E. E. (2021). A River Flood and Earthquake Risk Assessment of Railway Assets along the Belt and Road. *International Journal of Disaster Risk Science*, *12*(4), 553–567. https://doi.org/10.1007/S13753-021-00358-2/FIGURES/9

Weir, P. (2002). *Snow Avalanche Management in Forested Terrain* (Vol. 55). Government Publication Services. www.publications.gov.bc.ca

Wetwitoo, J., & Kato, H. (2017). High-speed rail and regional economic productivity through agglomeration and network externality: A case study of inter-regional transportation in Japan. *Case Studies on Transport Policy*, *5*(4), 549–559. https://doi.org/10.1016/J.CSTP.2017.10.008

Wheeler, R. L., Bufe, C. G., Johnson, M. L., Dart, R. L., & Norton, G. A. (2005). Seismotectonic map of Afghanistan, with annotated bibliography. In *Reston, VA, USA: US Department of the Interior, US Geological Survey*. Reston, VA, USA: US Department of the Interior, US Geological Survey.

Xiao, X., Ling, L., & Jin, X. (2012). A study of the derailment mechanism of a high speed train due to an earthquake. *Http://Dx.Doi.Org/10.1080/00423114.2011.597508*, *50*(3), 449–470. https://doi.org/10.1080/00423114.2011.597508

Yan, F., Zhang, Q., Ye, S., & Ren, B. (2019). A novel hybrid approach for landslide susceptibility mapping integrating analytical hierarchy process and normalized frequency ratio methods with the cloud model. *Geomorphology*, *327*, 170–187. https://doi.org/10.1016/j.geomorph.2018.10.024

Yang, X., Lin, S., Li, Y., & He, M. (2019). Can high-speed rail reduce environmental pollution? Evidence from China. *Journal of Cleaner Production*, *239*, 118135. https://doi.org/10.1016/J.JCLEPRO.2019.118135

Yariyan, P., Avand, M., Abbaspour, R. A., Karami, M., & Tiefenbacher, J. P. (2020). GIS-based spatial modeling of snow avalanches using four novel ensemble models. *Science of The Total Environment*, *745*, 141008. https://doi.org/10.1016/J.SCITOTENV.2020.141008

Yariyan, P., Omidvar, E., Minaei, F., Ali Abbaspour, R., & Tiefenbacher, J. P. (2021). An optimization on machine learning algorithms for mapping snow avalanche susceptibility. *Natural Hazards*, 1–36. https://doi.org/10.1007/S11069-021-05045-5/FIGURES/11

Yi, S. (2018a). Dynamic Analysis of High-Speed Railway Alignment. In *Dynamic Analysis of High-Speed Railway Alignment*. Elsevier. https://doi.org/10.1016/C2016-0-01248-2

Yi, S. (2018b). Railway Location. In *Principles of Railway Location and Design* (pp. 273–367). Academic Press. https://doi.org/10.1016/B978-0-12-813487-0.00004-4

Yildirim, V., & Bediroglu, S. (2019a). A geographic information system-based model for economical and eco-friendly high-speed railway route determination using analytic hierarchy process and least-cost-path analysis. *Expert Systems*, *36*(3). https://doi.org/10.1111/exsy.12376

Yildirim, V., & Bediroglu, S. (2019b). A geographic information system-based model for economical and eco-friendly high-speed railway route determination using analytic hierarchy process and least-cost-path analysis. *Expert Systems*, *36*(3), 1–14. https://doi.org/10.1111/exsy.12376

Yildirim, V., & Bediroglu, S. (2019c). A geographic information system-based model for economical and eco-friendly high-speed railway route determination using analytic hierarchy process and least-cost-path analysis. *Expert Systems*, *36*(3), e12376. https://doi.org/10.1111/EXSY.12376

Yildirim, V., Yomralioglu, T., Nisanci, R., Çolak, H. E., Bediroğlu, Ş., & Saralioglu, E. (2016). *Structure and Infrastructure Engineering Maintenance, Management, Life-Cycle Design and Performance A spatial multicriteria decision-making method for natural gas transmission pipeline routing A spatial multicriteria decision-making method for natural gas transmission pipeline routing*. https://doi.org/10.1080/15732479.2016.1173071

Yulianto, T., Suripin, S., & Purnaweni, H. (2019). *Zoning landslide vulnerable area according to geological structure, slopes, and landuse parameters In Trangkil Sukorejo Gunungpati Semarang City's Residental Area*. 12029. https://doi.org/10.1088/1742-6596/1217/1/012029

Zadeh, L. A. (1965). Fuzzy sets. *Information and Control*, *8*(3), 338–353. https://doi.org/10.1016/S0019-9958(65)90241-X

Zadeh, L. A. (1988). Fuzzy Logic. *Computer*, *21*(4), 83–93. https://doi.org/10.1109/2.53

Zeng, Q., & Dimitrakopoulos, E. G. (2018). Vehicle–bridge interaction analysis modeling derailment during earthquakes. *Nonlinear Dynamics*, *93*(4), 2315–2337. https://doi.org/10.1007/S11071-018-4327-6/TABLES/4

Zhao, J., Liu, K., & Wang, M. (2020). Exposure analysis of Chinese railways to multihazards based on datasets from 2000 to 2016.

*Http://Www.Tandfonline.Com/Action/JournalInformation?Show=aimsScope&journalCode=tgnh20#.VsXodSCLRhE*, *11*(1), 272–287. https://doi.org/10.1080/19475705.2020.1714753

Zhao, L., Zhang, X., & Zhao, F. (2021). The impact of high-speed rail on air quality in counties: Econometric study with data from southern Beijing-Tianjin-Hebei, China. *Journal of Cleaner Production*, *278*, 123604. https://doi.org/10.1016/J.JCLEPRO.2020.123604

Zhu, W., Liu, K., Wang, M., & Koks, E. E. (n.d.). Seismic Risk Assessment of the Railway Network of China's Mainland. *International Journal of Disaster Risk Science*, *11*. https://doi.org/10.1007/s13753-020-00292-9

## APPENDIX A

**Table 5.11.** The fuzzified pairwise comparison matrix for landslide susceptibility

**Table 5.11.** *The* fuzzified pairwise comparison matrix for snow avalanche susceptibility

| Criteria/Criteria | Slope | Aspect | Lithology | Rainfall | LULC | Distance from fault lines | Distance from roads | Distance from streams | NDVI | TWI |
|---|---|---|---|---|---|---|---|---|---|---|
| Slope | 1 1 1 | 6 7 8 | 1 1 2 | 1 2 3 | 4 5 6 | 2 3 4 | 7 8 9 | 7 8 9 | 5 6 7 | 3 4 5 |
| Aspect | 0 1/7 1/6 | 1 1 1 | 1/7 1/6 1/5 | 1/6 1/5 1/4 | 1 2 3 | 2 3 4 | 1 2 3 | 1 2 3 | 1/4 1/3 1/2 | 1/5 1/4 1/3 |
| Lithology | 1 1 1 | 5 6 7 | 1 1 1 | 1 2 3 | 2 3 4 | 3 4 5 | 6 7 8 | 6 7 8 | 5 6 7 | 1 2 3 |
| Rainfall | 0 1/2 1 | 4 5 6 | 1/3 1/2 1 | 1 1 1 | 2 3 4 | 1 2 3 | 4 5 6 | 4 5 6 | 3 4 5 | 2 3 4 |
| LULC | 0 1/5 1/4 | 1/3 1/2 1 | 1/4 1/3 1/2 | 1/4 1/3 1/2 | 1 1 1 | 1/3 1/2 1 | 2 3 4 | 2 3 4 | 1 2 3 | 1/4 1/3 1/2 |
| Distance from fault lines | 0 1/3 1/2 | 1/4 1/3 1/2 | 1/5 1/4 1/3 | 1/3 1/2 1 | 1 2 3 | 1 1 1 | 2 3 4 | 2 3 4 | 1 2 3 | 1 2 3 |
| Distance from roads | 0 1/8 1/7 | 1/3 1/2 1 | 1/8 1/7 1/6 | 1/6 1/5 1/4 | 1/4 1/3 1/2 | 1/4 1/3 1/2 | 1 1 1 | 1 1 2 | 1/4 1/3 1/2 | 1/5 1/4 1/3 |
| Distance from streams | 0 1/8 1/7 | 1/3 1/2 1 | 1/8 1/7 1/6 | 1/6 1/5 1/4 | 1/4 1/3 1/2 | 1/4 1/3 1/2 | 1/2 1 1 | 1 1 1 | 1/4 1/3 1/2 | 1/5 1/4 1/3 |
| NDVI | 0 1/6 1/5 | 2 3 4 | 1/7 1/6 1/5 | 1/5 1/4 1/3 | 1/3 1/2 1 | 1/3 1/2 1 | 2 3 4 | 2 3 4 | 1 1 1 | 1/4 1/3 1/2 |
| TWI | 0 1/4 1/3 | 3 4 5 | 1/3 1/2 1 | 1/4 1/3 1/2 | 2 3 4 | 1/3 1/2 1 | 3 4 5 | 3 4 5 | 2 3 4 | 1 1 1 |

**Table 5.12** *The process of obtaining normalized weights by calculating the fuzzy geometric mean and fuzzy weights for landslide susceptibility*

| Fuzzy Geometric mean value ri | | | Fuzzy Weights | | | Weights | Normalized Weights |
|---|---|---|---|---|---|---|---|
| 2.85 | 3.56 | 4.48 | 0.28 | 0.26 | 0.25 | 0.26 | 0.262 |
| 0.44 | 0.63 | 0.83 | 0.04 | 0.05 | 0.05 | 0.04 | 0.045 |
| 2.20 | 3.11 | 3.76 | 0.22 | 0.23 | 0.21 | 0.22 | 0.216 |
| 1.56 | 2.16 | 2.96 | 0.15 | 0.16 | 0.16 | 0.16 | 0.158 |
| 0.51 | 0.71 | 1.04 | 0.05 | 0.05 | 0.06 | 0.05 | 0.053 |
| 0.66 | 1.00 | 1.43 | 0.07 | 0.07 | 0.08 | 0.07 | 0.072 |
| 0.27 | 0.33 | 0.47 | 0.03 | 0.02 | 0.03 | 0.03 | 0.026 |
| 0.26 | 0.33 | 0.44 | 0.03 | 0.02 | 0.02 | 0.02 | 0.024 |
| 0.50 | 0.66 | 0.92 | 0.05 | 0.05 | 0.05 | 0.05 | 0.049 |
| 0.95 | 1.28 | 1.79 | 0.09 | 0.09 | 0.10 | 0.09 | 0.095 |

**Table 13** *The calculated principal eigenvalue, consistency index, and consistency ratio of the fuzzy-AHP method for landslide susceptibility*

| **ʎmax** | RI | CI | CR |
|---|---|---|---|
| 11.0 | 1.49 | 0.114 | 0.077 |

**Table *5.14*** *The fuzzified pairwise comparison matrix for snow avalanche susceptibility*

**Table 5.14.** *The* fuzzified pairwise comparison matrix for snow avalanche susceptibility

| Criteria/Criteria | Slope | | | Precipitation | | | Temperature | | | LULC | | | Length of Slope | | | Curvature | | | TRI | | | Aspect | | | WEI | | | Elevation | | |
|---|---|---|---|---|---|---|---|---|---|---|---|---|---|---|---|---|---|---|---|---|---|---|---|---|---|---|---|---|---|---|
| Slope | 1 | 1 | 1 | 1 | 1 | 2 | 1 | 2 | 3 | 2 | 3 | 4 | 3 | 4 | 5 | 3 | 4 | 5 | 4 | 5 | 6 | 5 | 6 | 7 | 6 | 7 | 8 | 7 | 8 | 9 |
| Precipitation | 1/2 | 1 | 1 | 1 | 1 | 1 | 1 | 2 | 3 | 2 | 3 | 4 | 3 | 4 | 5 | 3 | 4 | 5 | 4 | 5 | 6 | 5 | 6 | 7 | 6 | 7 | 8 | 7 | 8 | 9 |
| Temperature | 1/3 | 1/2 | 1 | 1/3 | 1/2 | 1 | 1 | 1 | 1 | 1 | 2 | 3 | 2 | 3 | 4 | 2 | 3 | 4 | 3 | 4 | 5 | 4 | 5 | 6 | 4 | 5 | 6 | 5 | 6 | 7 |
| LULC | 1/4 | 1/3 | 1/2 | 1/4 | 1/3 | 1/2 | 1/3 | 1/2 | 1 | 1 | 1 | 1 | 2 | 3 | 4 | 1 | 2 | 3 | 2 | 3 | 4 | 4 | 5 | 6 | 5 | 6 | 7 | 6 | 7 | 8 |
| Length of Slope | 1/5 | 1/4 | 1/3 | 1/5 | 1/4 | 1/3 | 1/4 | 1/3 | 1/2 | 1/4 | 1/3 | 1/2 | 1 | 1 | 1 | 1 | 2 | 3 | 2 | 3 | 4 | 3 | 4 | 5 | 5 | 6 | 7 | 6 | 7 | 8 |
| Curvature | 1/5 | 1/4 | 1/3 | 1/5 | 1/4 | 1/3 | 1/4 | 1/3 | 1/2 | 1/3 | 1/2 | 1 | 1/3 | 1/2 | 1 | 1 | 1 | 1 | 1 | 2 | 3 | 4 | 5 | 6 | 4 | 5 | 6 | 5 | 6 | 7 |
| TRI | 1/6 | 1/5 | 1/4 | 1/6 | 1/5 | 1/4 | 1/5 | 1/4 | 1/3 | 1/4 | 1/3 | 1/2 | 1/4 | 1/3 | 1/2 | 1/3 | 1/2 | 1 | 1 | 1 | 1 | 1 | 2 | 3 | 2 | 3 | 4 | 4 | 5 | 6 |
| Aspect | 1/7 | 1/6 | 1/5 | 1/7 | 1/6 | 1/5 | 1/6 | 1/5 | 1/4 | 1/6 | 1/5 | 1/4 | 1/5 | 1/4 | 1/3 | 1/6 | 1/5 | 1/4 | 1/3 | 1/2 | 1 | 1 | 1 | 1 | 2 | 3 | 4 | 4 | 5 | 6 |
| WEI | 1/8 | 1/7 | 1/6 | 1/8 | 1/7 | 1/6 | 1/6 | 1/5 | 1/4 | 1/7 | 1/6 | 1/5 | 1/7 | 1/6 | 1/5 | 1/6 | 1/5 | 1/4 | 1/4 | 1/3 | 1/2 | 1/4 | 1/3 | 1/2 | 1 | 1 | 1 | 2 | 3 | 4 |
| Elevation | 1/9 | 1/8 | 1/7 | 1/9 | 1/8 | 1/7 | 1/7 | 1/6 | 1/5 | 1/8 | 1/7 | 1/6 | 1/8 | 1/7 | 1/6 | 1/7 | 1/6 | 1/5 | 1/6 | 1/5 | 1/4 | 1/6 | 1/5 | 1/4 | 1/4 | 1/3 | 1/2 | 1 | 1 | 1 |

**Table 5.15.** *The process of obtaining normalized weights by calculating the fuzzy geometric mean and fuzzy weights for snow avalanche susceptibility*

| Fuzzy Geometric mean value ri | | | Fuzzy Weights | | | Weights | Normalized Weights |
|---|---|---|---|---|---|---|---|
| 2.62 | 3.32 | 4.23 | 0.24 | 0.23 | 0.23 | 0.23 | 0.232 |
| 2.44 | 3.32 | 3.94 | 0.22 | 0.23 | 0.21 | 0.22 | 0.222 |
| 1.60 | 2.20 | 3.01 | 0.15 | 0.15 | 0.16 | 0.15 | 0.153 |
| 1.26 | 1.71 | 2.29 | 0.12 | 0.12 | 0.12 | 0.12 | 0.119 |
| 0.92 | 1.21 | 1.57 | 0.08 | 0.08 | 0.08 | 0.08 | 0.084 |
| 0.79 | 1.05 | 1.45 | 0.07 | 0.07 | 0.08 | 0.07 | 0.074 |
| 0.50 | 0.66 | 0.91 | 0.05 | 0.05 | 0.05 | 0.05 | 0.047 |
| 0.37 | 0.46 | 0.59 | 0.03 | 0.03 | 0.03 | 0.03 | 0.032 |
| 0.25 | 0.31 | 0.38 | 0.02 | 0.02 | 0.02 | 0.02 | 0.022 |
| 0.18 | 0.20 | 0.24 | 0.02 | 0.01 | 0.01 | 0.01 | 0.014 |

**Table 5.16.** *The calculated principal eigenvalue, consistency index, and consistency ratio of the fuzzy-AHP method for snow avalanche susceptibility*

| $\lambda$max | RI | CI | CR |
|---|---|---|---|
| 10.9 | 1.49 | 0.096 | 0.0644 |

**Table 5.17.** *The* fuzzified pairwise comparison matrix for flood susceptibility

| Criteria/Criteria | Rainfall | Lithology | Soil Types | slope | LULC | Distance from Streams | Flow Accumulation | TWI | Curvature |
|---|---|---|---|---|---|---|---|---|---|
| **Rainfall** | 1 1 1 | 1 1 2 | 1 2 3 | 2 3 4 | 3 4 5 | 4 5 6 | 4 5 6 | 5 6 7 | 5 6 7 |
| **Lithology** | 1 1 1 | 1 1 1 | 1 2 3 | 2 3 4 | 3 4 5 | 4 5 6 | 4 5 6 | 5 6 7 | 5 6 7 |
| **Soil Types** | 0 1/2 1 | 1/3 1/2 1 | 1 1 1 | 1 2 3 | 2 3 4 | 3 4 5 | 3 4 5 | 4 5 6 | 4 5 6 |
| **slope** | 0 1/3 1/2 | 1/4 1/3 1/2 | 1/3 1/2 1 | 1 1 1 | 1 2 3 | 2 3 4 | 2 3 4 | 4 5 6 | 4 5 6 |
| **LULC** | 0 1/4 1/3 | 1/5 1/4 1/3 | 1/4 1/3 1/2 | 1/3 1/2 1 | 1 1 1 | 1 2 3 | 2 3 4 | 3 4 5 | 4 5 6 |
| **Distance from Streams** | 0 1/5 1/4 | 1/6 1/5 1/4 | 1/5 1/4 1/3 | 1/4 1/3 1/2 | 1/3 1/2 1 | 1 1 1 | 1 2 3 | 2 3 4 | 2 3 4 |
| **Flow Accumulation** | 0 1/5 1/4 | 1/6 1/5 1/4 | 1/5 1/4 1/3 | 1/4 1/3 1/2 | 1/4 1/3 1/2 | 1/3 1/2 1 | 1 1 1 | 1 2 3 | 2 3 4 |
| **TWI** | 0 1/6 1/5 | 1/7 1/6 1/5 | 1/6 1/5 1/4 | 1/6 1/5 1/4 | 1/5 1/4 1/3 | 1/4 1/3 1/2 | 1/3 1/2 1 | 1 1 1 | 1 2 3 |
| **Curvature** | 0 1/6 1/5 | 1/7 1/6 1/5 | 1/6 1/5 1/4 | 1/6 1/5 1/4 | 1/6 1/5 1/4 | 1/4 1/3 1/2 | 1/4 1/3 1/2 | 1/3 1/2 1 | 1 1 1 |

**Table 5.17.** *The fuzzified pairwise comparison matrix for flood susceptibility*

**Table 1.8.** *The process of obtaining normalized weights by calculating the fuzzy geometric mean and fuzzy weights for flood susceptibility*

| Fuzzy Geometric mean value ri | | | Fuzzy Weights | | | Weights | Normalized Weights |
|---|---|---|---|---|---|---|---|
| 2.37 | 3.03 | 3.91 | 0.26 | 0.24 | 0.24 | 0.25 | 0.248 |
| 2.20 | 3.03 | 3.62 | 0.24 | 0.24 | 0.22 | 0.24 | 0.235 |
| 1.47 | 2.04 | 2.81 | 0.16 | 0.16 | 0.17 | 0.17 | 0.166 |
| 1.03 | 1.43 | 1.96 | 0.11 | 0.12 | 0.12 | 0.12 | 0.116 |
| 0.76 | 1.03 | 1.39 | 0.08 | 0.08 | 0.09 | 0.08 | 0.084 |
| 0.50 | 0.68 | 0.93 | 0.05 | 0.05 | 0.06 | 0.06 | 0.055 |
| 0.39 | 0.53 | 0.73 | 0.04 | 0.04 | 0.05 | 0.04 | 0.044 |
| 0.28 | 0.36 | 0.48 | 0.03 | 0.03 | 0.03 | 0.03 | 0.029 |
| 0.23 | 0.28 | 0.38 | 0.03 | 0.02 | 0.02 | 0.02 | 0.024 |

**Table 5.19.** *The calculated principal eigenvalue, consistency index, and consistency ratio of the fuzzy-AHP method for flood susceptibility*

| $\lambda_{max}$ | RI | CI | CR |
|---|---|---|---|
| 9.4 | 1.45 | 0.056 | 0.0386 |

**APPENDIX B**

1- The JavaScript code used for calculating the LST using MODIS satellite MOD11A2 V6 product in Google Earth Engine API.

```
Imports (1 entry)
 var table: Table users/suhrabuddinnasery93/HSR_Provinces
var table;

var Dataset2015 = ee.ImageCollection("MODIS/006/MOD11A2")
.filterBounds(table)
.filterDate('2015-01-20','2015-03-01')
.mean()
.clip(table)
.multiply(0.02)
.subtract(273.15);
print(Dataset2015);
Map.addLayer(Dataset2015);

var Dataset2016 = ee.ImageCollection("MODIS/006/MOD11A2")
.filterBounds(table)
.filterDate('2016-01-20','2016-03-01')
.mean()
.clip(table)
.multiply(0.02)
.subtract(273.15);
print(Dataset2016);
Map.addLayer(Dataset2016);

var Dataset2017 = ee.ImageCollection("MODIS/006/MOD11A2")
.filterBounds(table)
.filterDate('2017-01-20','2017-03-01')
.mean()
.clip(table)
.multiply(0.02)
.subtract(273.15);
print(Dataset2017);
Map.addLayer(Dataset2017);

var Dataset2018 = ee.ImageCollection("MODIS/006/MOD11A2")
.filterBounds(table)
.filterDate('2018-01-20','2018-03-01')
.mean()
.clip(table)
.multiply(0.02)
.subtract(273.15);
print(Dataset2018);
Map.addLayer(Dataset2018);

var Dataset2019 = ee.ImageCollection("MODIS/006/MOD11A2")
.filterBounds(table)
.filterDate('2019-01-20','2019-03-01')
.mean()
.clip(table)
.multiply(0.02)
.subtract(273.15);
print(Dataset2019);
Map.addLayer(Dataset2019);
```

```
var Dataset2020 = ee.ImageCollection("MODIS/006/MOD11A2")
.filterBounds(table)
.filterDate('2020-01-20','2020-03-01')
.mean()
.clip(table)
.multiply(0.02)
.subtract(273.15);
print(Dataset2020);
Map.addLayer(Dataset2020);

var D2015 = Dataset2015.select('LST_Day_1km');
var D2016 = Dataset2016.select('LST_Day_1km');
var D2017 = Dataset2017.select('LST_Day_1km');
var D2018 = Dataset2018.select('LST_Day_1km');
var D2019 = Dataset2019.select('LST_Day_1km');
var D2020 = Dataset2020.select('LST_Day_1km');

Export.image.toDrive({
  image: D2020,
  description: 'ModisLST2020',
  region: table,
  scale: 1000,
  maxPixels: 1e9
});

Export.image.toDrive({
  image: D2019,
  description: 'ModisLST2019',
  region: table,
  scale: 1000,
  maxPixels: 1e9
});
Export.image.toDrive({
  image: D2018,
  description: 'ModisLST2018',
  region: table,
  scale: 1000,
  maxPixels: 1e9
});
Export.image.toDrive({
  image: D2017,
  description: 'ModisLST2017',
  region: table,
  scale: 1000,
  maxPixels: 1e9
});
Export.image.toDrive({
  image: D2016,
  description: 'ModisLST2016',
  region: table,
  scale: 1000,
  maxPixels: 1e9
});
Export.image.toDrive({
  image: D2015,
  description: 'ModisLST2015',
  region: table,
  scale: 1000,
  maxPixels: 1e9
});
```

2- The JavaScript code used for calculating the annual average rainfall using TerraClimate dataset of IDAHO University in Google Earth Engine API.

```
Imports (1 entry)
var table: Table users/suhrabuddinnasery93/HSR_Provinces

var table;
var dataset = ee.ImageCollection("IDAHO_EPSCOR/TERRACLIMATE")
.filterBounds(table)
.filterDate('2000-12-01','2001-05-28')
.mean()
.clip(table);
print(dataset);
Map.addLayer(dataset);

var dataset1 = ee.ImageCollection("IDAHO_EPSCOR/TERRACLIMATE")
.filterBounds(table)
.filterDate('2001-12-01','2002-05-28')
.mean()
.clip(table);
print(dataset1);
Map.addLayer(dataset1);

var dataset2 = ee.ImageCollection("IDAHO_EPSCOR/TERRACLIMATE")
.filterBounds(table)
.filterDate('2002-12-01','2003-05-28')
.mean()
.clip(table);
print(dataset2);
Map.addLayer(dataset2);

var dataset3 = ee.ImageCollection("IDAHO_EPSCOR/TERRACLIMATE")
.filterBounds(table)
.filterDate('2003-12-01','2004-05-28')
.mean()
.clip(table);
print(dataset3);
Map.addLayer(dataset3);

var dataset4 = ee.ImageCollection("IDAHO_EPSCOR/TERRACLIMATE")
.filterBounds(table)
.filterDate('2004-12-01','2005-05-28')
.mean()
.clip(table);
print(dataset4);
Map.addLayer(dataset4);

var dataset5 = ee.ImageCollection("IDAHO_EPSCOR/TERRACLIMATE")
.filterBounds(table)
.filterDate('2015-12-01','2016-05-28')
.mean()
.clip(table);
print(dataset5);
Map.addLayer(dataset5);
```

```
var dataset6 = ee.ImageCollection("IDAHO_EPSCOR/TERRACLIMATE")
.filterBounds(table)
.filterDate('2016-12-01','2017-05-28')
.mean()
.clip(table);
print(dataset6);
Map.addLayer(dataset6);

var dataset7 = ee.ImageCollection("IDAHO_EPSCOR/TERRACLIMATE")
.filterBounds(table)
.filterDate('2017-12-01','2018-05-28')
.mean()
.clip(table);
print(dataset7);
Map.addLayer(dataset7);

var dataset8 = ee.ImageCollection("IDAHO_EPSCOR/TERRACLIMATE")
.filterBounds(table)
.filterDate('2018-12-01','2019-05-28')
.mean()
.clip(table);
print(dataset8);
Map.addLayer(dataset8);

var dataset9 = ee.ImageCollection("IDAHO_EPSCOR/TERRACLIMATE")
.filterBounds(table)
.filterDate('2019-12-01','2020-05-28')
.mean()
.clip(table);
print(dataset9);
Map.addLayer(dataset9);

var dataset10 = ee.ImageCollection("IDAHO_EPSCOR/TERRACLIMATE")
.filterBounds(table)
.filterDate('2020-12-01','2021-05-28')
.mean()
.clip(table);
print(dataset10);
Map.addLayer(dataset10);

var D2000 = dataset.select('pr');
var D2001 = dataset1.select('pr');
var D2002 = dataset2.select('pr');
var D2003 = dataset3.select('pr');
var D2004 = dataset4.select('pr');
var D2015 = dataset5.select('pr');
var D2016 = dataset6.select('pr');
var D2017 = dataset7.select('pr');
var D2018 = dataset8.select('pr');
var D2019 = dataset9.select('pr');
var D2020 = dataset10.select('pr');


var Combined_Dataset = ee.ImageCollection([D2000,D2001,
D2002,D2003,D2004,D2015, D2016, D2017,D2018,D2019,D2020])
.mosaic();
print(Combined_Dataset);
Map.addLayer(Combined_Dataset);

Export.image.toDrive({
  image: Combined_Dataset,
  description: 'IDAHO_Combined_Dataset',
  region: table,
  scale: 1000,
  maxPixels: 1e9
});
```

3- The JavaScript code used for calculating the NDVI index using Sentinel 2 satellite MSI dataset in Google Earth Engine API.

```
Imports (1 entry)
var table: Table users/suhrabuddinnasery93/HSR_Provinces

var HSR = table;
Map.centerObject(HSR);
Map.addLayer(HSR);

function maskS2clouds(image) {
  var qa = image.select('QA60');
  var cloudBitMask = 1 << 10;
  var cirrusBitMask = 1 << 11;
  var mask = qa.bitwiseAnd(cloudBitMask).eq(0)
      .and(qa.bitwiseAnd(cirrusBitMask).eq(0));
  return image.updateMask(mask).divide(10000);
}

var Sentinel = ee.ImageCollection('COPERNICUS/S2_SR')
.filterBounds(HSR)
.filterDate('2021-08-10','2021-08-30')
.filter(ee.Filter.lt('CLOUDY_PIXEL_PERCENTAGE',20))
.map(maskS2clouds)
.median()
.clip(HSR);

var nir = Sentinel.select('B8');
var red = Sentinel.select('B4');
var ndvi = nir.subtract(red).divide(nir.add(red)).rename('NDVI');
Map.addLayer(ndvi);
Map.addLayer(Sentinel);

Export.image.toDrive({
  image: ndvi,
  description: 'Sentinelndvimap',
  region: HSR,
  scale: 30,
  maxPixels: 1e9
});
```

# CURRICULUM VITAE

## PERSONAL INFORMATION

Name/Surname: Suhrabuddin Nasery

Languages: Pashto, Persian, English, Turkish, Hindi

## PROFESSIONAL SUMMARY

GIS and Remote Sensing professional with 5+ years experience in MIS, thematic/topographic mapping, spatial analysis, data manipulation, and data visualization. Expertise includes advanced satellite image processing, land cover mapping, time-series analysis, land-use optimization, allocation model design, spatial decision support model design, web-based mapping, program reporting, monitoring, and evaluation. Highly skilled in ArcGIS Pro/Desktop/Online, QGIS, PostgreSQL, PostGIS, and Google Earth Engine.

## EMPLOYMENT HISTORY

- **GIS and Surveying Manager**, Kabul Municipality. Kabul, Afghanistan
  September 2017 – November 2018
- **GIS Engineer**, Kabul Municipality. Kabul, Afghanistan
  February 2017 – August 2017
- **GIS Intern**, Afghan Geodesy and Cartography Head Office (AGCHO). Kabul, Afghanistan
  January 2016 – April 2016
- **Customer Service Representative (CSR)**, Etisalat Afghanistan. Kabul, Afghanistan
  February 2015 – January 2017

## EDUCATION

- **Eskişehir Technical University**, Eskisehir, Turkey GPA 3.96
  Master of Science, Remote Sensing and Geographical Information Systems, January 2022
- **Kabul Polytechnic University**, Kabul, Afghanistan GPA 3.69
  Bachelor of Science, Geodesy Engineering, August 2016

## PUBLICATIONS

1. Snow avalanche risk mapping using GIS-based multi-criteria decision analysis: the case of Van, Turkey
   (DOI: https://doi.org/10.1007/s12517-021-07112-4)
2. GIS-based wind farm suitability assessment using fuzzy AHP multi-criteria approach: the case of Herat, Afghanistan
   (DOI: https://doi.org/10.1007/s12517-021-07478-5)
3. Burn area detection and burn severity assessment using Sentinel 2 MSI data: The case of Karabağlar district, İzmir/Turkey
   (https://dergipark.org.tr/en/pub/turkgeo/issue/56822/770803)